



Norwegian University of
Science and Technology

Addressing the barriers for delivery of liposomal nanoparticles to tumors

Kristine Andreassen

Nanotechnology

Submission date: June 2018

Supervisor: Catharina de Lange Davies, IFY

Co-supervisor: Marieke Olsman, IFY

Norwegian University of Science and Technology
Department of Physics

Preface

This master thesis was carried out during the spring of 2018 at the department of physics at NTNU. The thesis builds on a specialization project completed in the fall of 2017, and it follows that some theory and methods will be similar between the two reports. Further, some results from the specialization project have been expanded and included in this work. This work presented here was part of a larger collaboration with two PhD-candidates, Marieke Olsman, who performed the animal experiments, and Viktoria Sereti, who provided the NPs.

Many people have contributed to making this semester a rewarding and fulfilling end to my time as a student in Trondheim. First of all, I would like to thank Professor Catharina de Lange Davies for always showing interest in the progression of this project and for taking the time to provide useful advice and feedback. Ph.D. candidate, and best assistant, Marieke Olsman deserves a huge thanks for many good discussions, MATLAB scripts and expertise, and for all the feedback and advice. Thank you, Astrid Bjørkøy for excellent training on the SP8 microscope during the specialization project and for always being very helpful with advice and technical problems. I would like to thank the biophysics group for excellent feedback, cake, and useful discussions. To Snorre, thanks for motivational songs and support, and for helping with proofreading.

Summary

This study concerns the enhanced delivery of three types of fluorescently labelled liposomal nanoparticles to prostate cancer xenographs. Passive delivery of the liposomes was achieved by utilizing the enhanced permeability and retention effect within tumors, while active delivery was achieved by introducing microbubbles along with the liposomal nanoparticles and applying ultrasound locally to the tumor tissue. Cavitation of the microbubbles will induce stress on the blood vessel walls, which increases their permeability. Ultrasound can also cause local streaming of interstitial liquid and thereby increase penetration of nanoparticles into tumor tissue. In this study, four barriers to drug delivery was addressed by studying the aggregation behaviour of the NPs, their extravasation and distribution in tumor tissue with and without exposure to ultrasound and microbubbles, and their cellular uptake in vitro. Poly(ethylene glycol) is attached to all three types of liposomal nanoparticles to increase their stealth.

For all three formulations the fluorescence emission spectra were captured and assessed. Aggregation behaviour of the NPs when mixed with whole blood and serum was investigated by confocal microscopy. The research was concerned with animal experiments on mice (all animal experiments were performed by Ph.D. candidate Marieke Olsman). Tumor tissue samples from the animal experiments were imaged by confocal and multiphoton microscopy by the author, and image analysis was performed to evaluate the effect of ultrasound on the extravasation of nanoparticles and distance travelled from the blood vessel wall. In addition, in vitro cellular uptake of the three nanoparticles was investigated using flow cytometry, supported by confocal microscopy. The behaviour of the three liposomal nanoparticles when mixed with whole blood and serum was investigated by confocal microscopy.

Applying ultrasound was found to minimally increase extravasation of all three nanoparticles for both mechanical indices, with the exception of one low ultrasound intensity group. A large mean distance travelled from blood vessels was obtained when the extravasation was relatively high. A large degree of heterogeneity was seen between and within animals, making it challenging to evaluate whether the observed effects were truly due to ultrasound exposure. There was no clear aggregation behaviour of the nanoparticles observed when added to blood and serum, but more aggregates were observed in the stock solution of the standard nanoparticles, compared to the other two nanoparticles. The standard formulation of nanoparticles were taken up in cells much more frequently than the cleavable and non-cleavable formulations of nanoparticles. Removing of the poly(ethylene glycol) did not affect the cellular uptake in vitro.

Sammendrag

Denne studien onhandler økt leveranse av tre forskjellige nanopartikler, merket med fluorescerende molekyler, til prostatakreftsvulster implantert i mus. Passivt opptak av liposomene ble oppnådd ved å utnytte effekten av økt bloduttredelse og opphoping i svulster. Aktivt opptak ble oppnådd ved å introdusere mikrometer-store gasbobler sammen med nanopartiklene samt ved å rette ultralyd mot svulsten. Ultralyd får gasboblene til å oscillere, og dette kan påføre stress mot blodåreveggene, som kan øke bloduttredelsen. Ultralyd kan også øke fordelingen av nanopartiklene i svulsten ved å skape væskestrømninger lokalt. I denne studien ble fire barrierer for levering av nanopartikler til krefceller taklet ved å studere aggregering av nanopartiklene, bloduttredelse i fordeling i kreftvev med og uten ultralyd og gasbobler, og opptak av partiklene i celler in vitro. Spektra av utslippet av fluorescens fra de to fluoroforene i de tre nanopartiklene ble målt. Aggregering av nanopartiklene blandet med blod eller serum ble undersøkt med konfokalmikroskopi. Nanopartiklene ble brukt i dyreforsøk utført av PhD-kandidat Marieke Olsman, og vevsprøver fra dyreforsøkene ble undersøkt ved konfokal- og multifotonmikroskopi av forfatteren. Bildeanalyse ble utført for å evaluere bloduttredelse av partiklene og avstanden deres fra blodåreveggen. I tillegg ble opptak i celler evaluert in vitro ved væskestrømscytometri, og funnene ble underbygget med konfokalmikroskopi. Ved undersøkelser i konfokalmikroskopi ble oppførselen til nanopartiklene etter blanding med blod og serum undersøkt.

Det ble observert at ultralyd i kombinasjon med mikrobobler økte bloduttredelsen av nanopartiklene minimalt. Avstanden fra blodåreveggen som nanopartiklene befant seg ved virket å øke minimalt når bloduttredelsen var høy. Det var imidlertid store variasjoner både mellom ulike dyr og innad i individuelle dyr. Derfor kan det ikke sies med sikkerhet at økningen i bloduttredelse og fordeling i vev skyldes ultralydbehandlingen. Siden relativt få dyr ble undersøkt ble det ikke utført en statistisk analyse av resultatene. De kjemiske sammensetningene av nanopartiklene virket å påvirke både aggregering og opptak i celler in vitro. Flere aggregater ble observert i standard formuleringen an nanopartikler. Standard formuleringen ble tatt opp til en større grad enn den kløyvbare og den ikke-kløyvbare formuleringen. Å fjerne polyetylen glycol endret ikke opptak i celler in vitro.

Abbreviations

BBB	blood brain barrier.
CLSM	confocal laser scanning microscopy.
ECM	extracellular matrix.
EPR	enhanced permeability and retention.
GM	growth medium.
MBs	microbubbles.
MI	mechanical index.
MMPs	matrix metalloproteinases.
MP	multiphoton.
NPs	nanoparticles.
PEG	poly(ethylene glycol).
ROI	region of interest.
SHG	second harmonic generation.
TPLSM	two photon laser scanning microscopy.
US	ultrasound.
VEGF	vascular endothelial growth factor.
WLL	white light laser.

Glossary

Basement membrane	ECM proteins arranged in sheet-like structures that lines and connects the ECM to other structures such as skin, blood vessels, and lymph vessels. It consists of heparan sulfate (a glycosaminoglycan), and proteins such as collagen type IV, fibronectin, laminin and enactin.
Cavitate	To form cavities or bubbles. "Cavitation" is used here to describe the oscillation of bubble diameter with acoustic pressure.
Cytostatic	Cytostatic drugs stop cell growth. (Cyto: cell, stasis: stop).
Cytotoxic	Cytotoxic drugs kill cells (Cyto: cell, toxic: poison (here: killing)).
Depth of field	Area between upper and lower planes of the in-focus region.
Endothelial fenestrae	Transcellular holes in endothelial cells. Allow for diffusion of small molecules such as O ₂ and glucose across the blood vessel wall.
Extravasation	The leakage of fluids out of it's container, e.g. blood out of blood vessels.
Interstitium	The space of a tissue (e.g. tumor) bounded by blood vessel walls and cellular membranes.
Metastasize	To spread by metastasis; a change in location.
Necrosis	Uncontrolled cell death. Usually leaves a lot of debris, and can induce necrosis in neighboring cells.
Neoplasia	Rapid, abnormal cell growth.
Photon	A quantum (or unit) of electromagnetic radiation. Also known as a "wave package" or a "light particle". The energy of a photon depends on it's frequency.
Proliferation	To increase in number, e.g. by cell division, or growth by the production of new parts.
Quantum yield	The quantum yield of a fluorescent molecule is the ratio between the number of emitted photons and the number of absorbed photons. The quantum number is often represented with the letter Q and has a value between 0 and 1.

- Stealth** The act of proceeding secretly or imperceptibly. Here, increasing stealth increases the circulation time in blood by hiding the particles from serum components and immune cells..
- Tumorigenesis** The development of tumors.
- Volume of distribution** The distribution of a drug between blood plasma and the rest of the body.

Contents

Preface	i
Summary	iii
Sammendrag	v
Abbreviations	vii
Glossary	ix
1 Introduction	1
1.1 Motivation	1
1.2 Aims of study	2
2 Theory	3
2.1 Cancer histology	3
2.1.1 The hallmarks of cancer	3
2.1.2 Cancer development and cell types	4
2.1.3 Enhanced permeability and retention effect	6
2.2 Tumor associated ECM	6
2.3 Matrix metalloproteinases	8
2.4 Barriers for drug delivery	8
2.4.1 Circulation in vasculature	8
2.4.2 Extravasation	9
2.4.3 Transport through tumor ECM	10
2.4.4 Cellular uptake	10
2.4.5 Additional challenges	11
2.5 Nanoparticles for drug delivery	11
2.6 Ultrasound	11
2.6.1 Mechanical index and cavitation	13
2.6.2 Radiation force	14
2.6.3 Thermal effects	15
2.7 Fluorescence	15
2.7.1 Two photon excitation and second harmonic generation	16
2.8 Confocal laser scanning microscopy	18
2.8.1 Multiphoton microscopy and second harmonic generation	19
2.9 Flow cytometry	19

3	Materials and experimental methods	21
3.1	Materials	21
3.1.1	Liposomal nanoparticles	21
3.1.2	Atto 488 and Atto 700	21
3.1.3	Preparation of solutions	22
3.2	Animal experiment protocol	23
3.2.1	Ultrasound setup	23
3.3	Cultivating cells	24
3.4	Fluorescence emission spectroscopy of nanoparticles	24
3.5	Nanoparticle behaviour in blood and serum	24
3.6	Confocal microscopy of tumor sections	25
3.6.1	Tile scans	26
3.7	Nanoparticle uptake experiments	28
3.7.1	Flow cytometry	28
3.7.2	Microscopy of nanoparticle uptake	28
3.8	Image processing and analysis	28
3.8.1	SP8 microscopy image post-processing	29
3.9	Data analysis	30
3.9.1	Statistics	30
4	Results	33
4.1	Characterization of nanoparticles	33
4.1.1	Fluorescence intensity measurements	33
4.1.2	Characterization of nanoparticle properties	36
4.1.3	Aggregation behaviour in blood and serum	36
4.2	Extravasation and distribution of nanoparticles	42
4.2.1	Extravasation of NPs from blood vessels	42
4.3	Penetration into tumor tissue	43
4.3.1	Distance travelled vs percent extravasated	45
4.3.2	Effect of blood vessel content on penetration	48
4.3.3	Effect of collagen content on penetration	51
4.4	Histology of tumors: distribution of collagen and blood vessels	55
4.5	In vitro nanoparticle uptake in cells	57
4.5.1	Flow cytometry to evaluate uptake in cells	57
4.5.2	Microscopy of live cells	59
5	Discussion	61
5.1	Stability and batch to batch variability	61
5.1.1	Temporal stability	61
5.1.2	Batch variability	62
5.2	Aggregation in blood and serum components	62
5.3	Extravasation of NPs without ultrasound	64
5.4	Distance travelled through ECM without ultrasound	65
5.5	Tumor heterogeneity and variability	66
5.6	Effect of US and MBs on extravasation	67
5.7	Effect of US and MBs on tumor penetration	69
5.8	Cellular uptake	70

<i>CONTENTS</i>	xiii
5.9 Clinical relevance, suggestions for improvement and future outlook	72
6 Conclusion	73
Appendix A Fluorescence emission overview	I
Appendix B Extravasation	III
Appendix C Microscopy images of tumor tissue	V
Appendix D Nuclei density	IX
Appendix E Biodistribution in animals	XI
Appendix F Microscopy images of lymph nodes	XIII

Chapter 1

Introduction

1.1 Motivation

Cancer are diseases which can arise in any tissue of the body, often triggered by external factors such as exposure to radiation, chemicals, or certain viral agents [1]. The incidence of cancer is rising globally, and so is the research aiming at improving treatment, seen by a steady increase in publications containing the phrases "drug delivery", "cancer" over the last years.

Treatment procedures and their success rates depend on the location and aggressiveness of the tumors. Treatment in the form of radiation, chemotherapeutic agents, and surgery are common, and often a combination is applied. Surgery is beneficial in tumors with defined edges, and in tumors with easy access, e.g. melanomas in the skin. When operating it is essential to remove every cancer cell, as just a single remaining cell can form the focus of a recurrent tumor. Radiation and chemotherapeutic agents usually target dividing cells. Dividing cells are killed by destruction of their DNA. However, dormant cells will not be affected by these drugs or radiation, and can facilitate the regrowth of tumors after the treatment has ended [2].

When chemotherapeutic agents are used in cancer therapy, only up to 0.01 % of the injected **cytostatic** and **cytotoxic** drugs reach the tumor where their detrimental effects are essential [3]. The rest of the dose will either be cleared by the body, or end up harming cells in other tissues, leading to the many side effects associated with chemotherapy. These side effects limit the dose that can safely be given to a patient.

One of many attempts to enhance tumor uptake and reduce side effects is to target tumor tissue specifically. Encapsulating the drug in a carrier can reduce the **volume of distribution** in healthy tissues [4, 5].

Many carrier systems can be utilized as drug delivery vehicles, including (but not limited to) polymers (as simple conjugates or as polymersomes), micelles, dendrimers, and liposomes [4, 6, 7, 8]. The term **nanoparticles (NPs)** will be used as a general term for these carriers in this thesis.

The NPs can target tumors passively or actively. Passive targeting utilizes the **enhanced permeability and retention (EPR)** effect, the tendency of tumor vasculature to be poorly developed and disorganized, leading to leaky blood vessels where larger entities can escape compared to the well organized blood vessels in healthy tissue [9]. To reach all potential tumors passively, the NPs have to avoid being opsonized and cleared by the immune system and organs such as the liver and spleen. A common way to increase the **stealth** of NPs in blood is to coat them with **poly(ethylene glycol) (PEG)**. PEG provides sterical hindrance for adsorbing proteins and thereby address the first barrier to successful drug delivery: clearance from blood. However, if

a particle is heavily PEGylated, the sterical hindrance can reduce cellular uptake.

Although increased stealth gives the NPs longer time to reach the tumor, and the EPR effect facilitates passive **extravasation**, this is rarely enough to obtain a sufficient amount of drug in the tumor **interstitium**. In fact, a multivariate analysis by Wilhelm et al. showed that the median amount that reach the tumor was just 0.7 %, i.e. only 10 times more than for free drug. For that, measures are taken to actively increase extravasation into the tumor, distribution through the interstitial space, and uptake in cells. Active targeting can be achieved by the addition of ligands binding to receptors overexpressed on cancer cells, it can be done by external triggers such as radiation to e.g. release drug locally, or it can be achieved by smart NP systems which are functionalized to release their load when entering the typically acidic pH of tumors.

One method designed to increase extravasation and penetration through interstitium is the application of **ultrasound (US)** and **microbubbles (MBs)**. The MBs are co-injected with NPs in blood, and when focused US is applied to the tumor, it causes the gas bubbles to **cavitate**. Cavitating MBs cause strain to nearby endothelial cells, and can increase extravasation by opening or increasing the dilation of pores in the endothelial cell membrane or between cells. Some systems use NPs that are attached to the MBs to ensure that the NPs are located in close proximity to the cavitating MBs. When the intensity of the US becomes sufficiently large, the MBs can implode, and assert a higher mechanical force on the blood vessel wall.

A recent clinical trial successfully used ultrasound and microbubbles to enhance delivery of the drug gemcitabine to inoperable pancreatic cancer [10]. They showed that combining US and MBs with chemotherapy did not increase toxicity and in some cases reduced the maximum tumor diameter. The median survival was increased by approximately 9 months. Although the patient number was low (n=10), these promising results are a step in the right direction.

1.2 Aims of study

The aim of this master thesis was to investigate whether ultrasound improved uptake and distribution of liposomal nanoparticles in human tumor xenografts in mice. Further, we wanted to examine the behaviour of the 3 liposomes in blood, and study their uptake by cells in vitro.

Following is a list of hypotheses that was tested:

1. The three NPs have different lipid compositions and it is expected that the formulation representing the clinically approved liposome (Doxil/Caelyx) will show less aggregation when exposed to whole blood and serum proteins, compared to the other two formulations.
2. Ultrasound will increase the extravasation of all three NPs.
3. The mechanical index will affect the degree of extravasation.
4. Ultrasound will increase the penetration of NPs into tumors.
5. The amount of blood vessels will affect the degree of extravasation of NPs.
6. Collagen will hinder the penetration of NPs.
7. All three NPs are expected to be taken up to a similar extent by cells in vitro.
8. Removing the PEG coating will result in increased uptake in cells in vitro.

Chapter 2

Theory

2.1 Cancer histology

2.1.1 The hallmarks of cancer

In 2000, Hanahan and Weinberg presented a list of 6 hallmarks of cancer, and in 2011 the list was expanded to include two additional "emerging" hallmarks and two characteristics enabling [tumorigenesis](#) and cancer growth [11]. The following list includes the original hallmarks (1-6), the new hallmarks (7-8), and the enabling characteristics (9-10):

1. Sustaining proliferative signaling
2. Evading growth suppressors
3. Resisting cell death
4. Enabling replicative immortality
5. Inducing angiogenesis
6. Activating invasion and metastasis
7. Reprogramming energy metabolism
8. Avoiding immune destruction
9. Genome instability and mutation
10. Tumor-promoting inflammation

As can be inferred from the list, the common property of all tumors, malignant or not, is increased [neoplasia](#) (rapid, abnormal cell growth), and [proliferation](#) (growth by cell division). This is evident from points 1-4 which all increase growth and suppress cell death, but also implied in points 5 and 7, which help enable growth by increasing nutrient supply via new blood vessels and changing the energy metabolism. The altered metabolism supports the increased nutrient demand [11]. In Hanahan and Weinberg's article, the metabolism alteration was termed an emerging hallmark, to emphasize its significance in cancer development and sustained growth while at the same time noting its functional dependence on some of the six original hallmarks. Later, Ward and Thompson argued that the change in metabolism definitively should be a part of the "core" hallmarks. They argue that change in metabolism could be the reason proto-oncogenes and tumor suppressor genes exist in the first place. They support the importance of altered metabolism in tumorigenesis by the notion that proliferating cells (cancer or healthy) change their metabolism to aerobic glycolysis (typical anaerobic metabolism in aerobic conditions), which, although not the most effective way to produce ATP, produces necessary components for the production of e.g. amino acids [12].

Although questions on definitions and whether some phenotypes are causes or effects of others still prevail, both articles agree that the hallmarks (and enabling characteristics) listed

above are all important features found before, during and/or after cancer development. As with most processes in cell biology, interactions are complex and often co-dependent on several factors. It is also worth mentioning that trying to establish a set of descriptive hallmarks found in such a highly variable group of diseases listed under the "cancer"-umbrella is difficult if not impossible. What is true for one cancer type, might be false for another, and within a tumor there are many different cells with different tasks and different properties. Therefore, different forms of treatment are necessary for different cancers.

Indeed, Floor et al. responded to Hanahan and Weinberg to emphasize the heterogeneity of cancers, both between different cancer types and between cell types found within single tumors. Floor et al. argued that Hanahan and Weinbergs paper is easily misunderstood as listing hallmarks which can be interpreted as being true for all cells in a tumor at all time points in the development and sustained growth of cancer cells [13]. However, Hanahan and Weinberg specifically state that the hallmarks should not be considered in this manner [11]. If anything, Floor et al. caused more confusion when they tried to clarify and elaborate the hallmarks. The only correct, important, clarifying thing they emphasize is that tumors are heterogeneous [13]. Indeed, this is why different medicines and treatments usually only work on some cancer types, and the complete removal of cancer cells tends to be very difficult. Therefore, it is important for scientists, researchers and surgeons who works with drug delivery, radiation, and surgical removal of tumors to remember that a universal solution to cure cancer is still to be developed, and that combining different treatments is likely necessary for the coming years.

2.1.2 Cancer development and cell types

In literature, benign tumors are the term used for abnormal tissues confined within the tissue in which it arise. Benign tumors are usually easy to remove, and their cells will not spread to other parts of the body. Malignant tumors are known as *cancer*. Malignant tumors are able to invade neighbouring tissue (making them more irregularly shaped than their benign counterparts), as well as [metastasize](#) (spread to other parts of the body). Metastasis is a complicated chain of events, where cells must to detach from their neighbouring cells and surrounding [extracellular matrix \(ECM\)](#), cut through the [basement membrane](#) that separates blood vessels from underlying tissue, enter the blood vessel, travel to a new location, perform [extravasation](#) (escaping circulation and entering tissue), where it can proliferate and create new cancerous tumors (see bottom part of Figure 2.1) [1, 11]. As this thesis doesn't consider differences between benign and malignant tumors, the terms "tumor" and "cancer" will be used interchangeably.

Tumors are initiated by cancer cells which have acquired a set of mutations (item 9 in the list above) including oncogenes and loss of tumor suppressors. As mentioned above, many have regarded a tumor as a rather homogeneous cell population, at least until late in tumor progression, when genetic instability and many rounds of cell replication lead to daughter cells with a large degree of clonal heterogeneity. However, the recognition of multiple cell types as well as the tumor microenvironment have received more and more attention [11]. As can be seen in the top part of Figure 2.1, cancer cells are accompanied by cancer stem cells, which is a relatively newly recognized sub-population believed to have increased ability to create new tumors when transfected to new animals, and expressing some transcriptional properties with some normal, healthy stem cell populations [11]. Immune inflammatory cells are believed to be recruited, in part, by cells which have died by [necrosis](#). Although the immune cells are supposed to hinder tumor growth, they also help the tumor cells by releasing growth factors

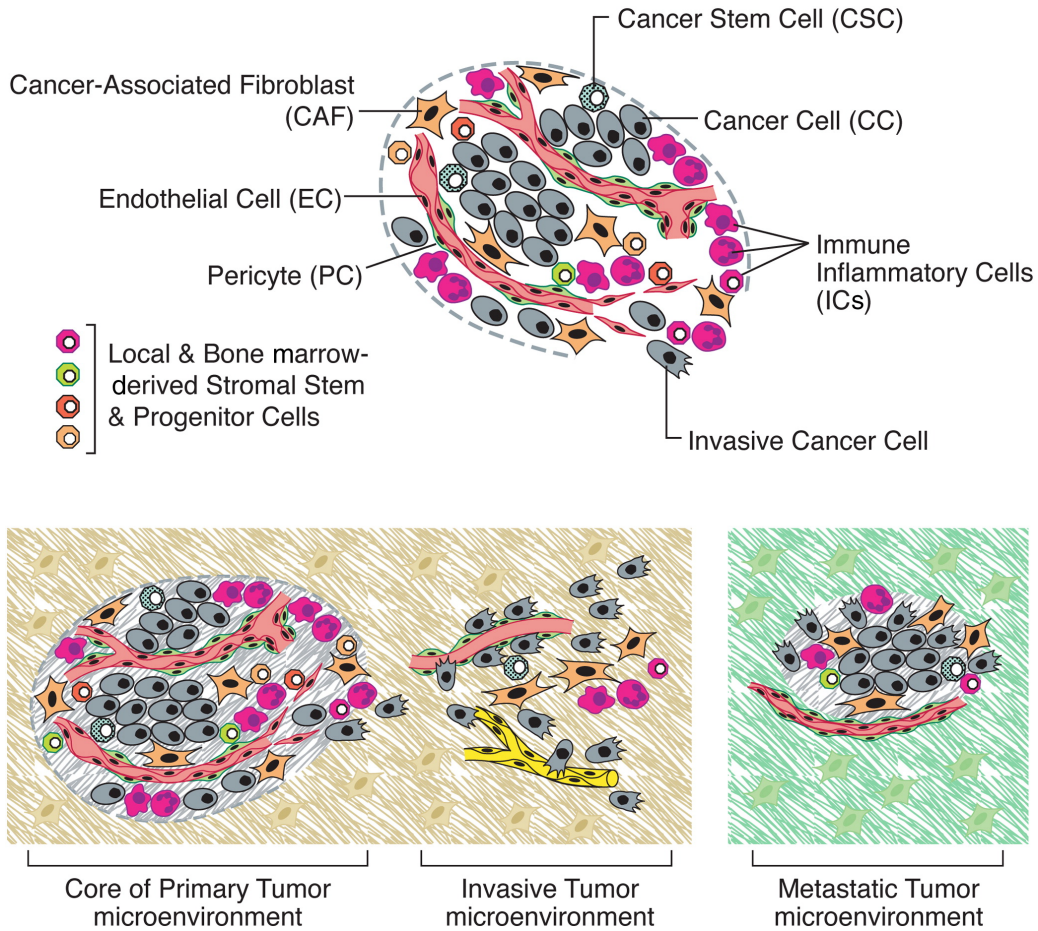


Figure 2.1: Illustration of different cells found in a tumor (top) and an illustration of microenvironments found in the different stages of metastasis. Adapted from [11] with permission from Elsevier.

and angiogenesis promoting factors during inflammation.

Invasive cancer cells have undergone differentiation from e.g. epithelial to mesenchymal cell types, to allow dislocation from the tumor to facilitate metastasis. Pericytes are cells which support blood vessels and help build the vascular basement membrane [11]. When the pericyte coverage is low, tumor vessels allegedly lose integrity and functionality, thereby possibly allowing more cells and molecules to travel across the vascular walls [11]. Poor vascular integrity is assumed to be a result of the fast growing tumor signaling for a higher rate of angiogenesis than the system can produce. The consequences of altered blood and lymph vessels will be further elaborated below, in section 2.1.3.

Endothelial cells form the vasculature of the tumor, and because the distance between cells and blood vessels greatly affects the availability of nutrients and waste disposal. Among other things, cells far from blood vessels will become hypoxic and perform anaerobic metabolism and release lactate, which lowers the tumor pH. In addition to blood vessels, endothelial cells also make up lymph vessels. Intratumoral lymph vessels are not as well understood as intratumoral blood vessels, but are believed to be a path of escape for metastasizing cells [11].

Cancer-associated fibroblasts are recruited or reprogrammed fibroblasts which are exploited by the cells of the tumor. The cancer-associated fibroblasts secrete many extra cellular components such as protein fibers and enzymes [11]. The fibroblasts are also believed to help sustain growth, angiogenesis, and invasion and metastasis [11].

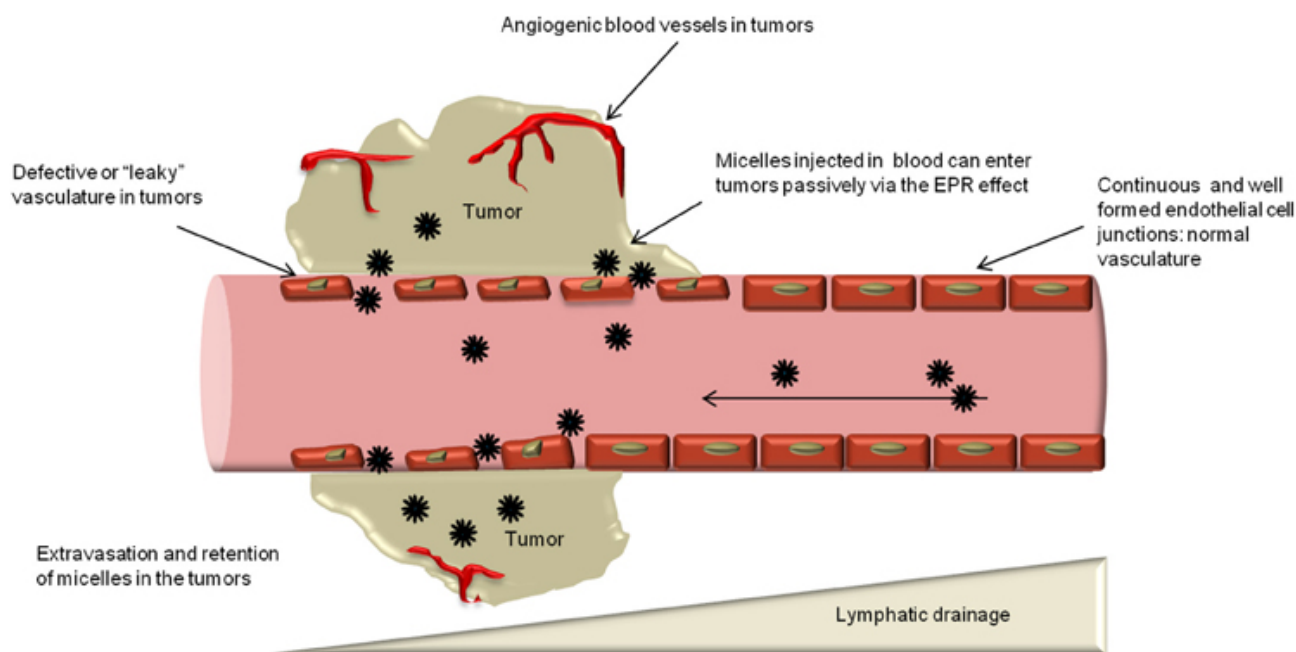


Figure 2.2: Illustration of the EPR effect in a tumor. Nanoparticles (* = micelles) cannot exit continuous normal vasculature. Within the tumor the vasculature becomes leaky and the NPs enter the tumor passively. Lymphatic drainage is low within the tumor [15].

2.1.3 Enhanced permeability and retention effect

The EPR effect (Figure 2.2) is caused by increased permeability of blood vessels, and under-developed lymphatic drainage [9]. Normally, angiogenesis is directed by fine tuned and highly controlled chemical gradients to create a well ordered, and functioning vasculature. Angiogenesis in tumors is induced by overexpression of [vascular endothelial growth factor \(VEGF\)](#) and other chemical cues. Loss of regulation can lead to vessels with an incomplete pericyte support, and as a result, tumor vasculature tends to have a highly heterogenous organization, inferior structure and function. Therefore, the blood flow within tumor blood vessels might be highly various in both speed, time and direction [14]. The poor structure often leads to leaky vessels where cells and molecules can extravasate and intravasate (i.e. moving from tissue to blood) easier than in healthy vessels [9, 11, 14]. The leakiness can be exploited for passive targeting, as particles which are small enough to escape leaky vessels, but too large to extravasate through healthy vessel walls, will passively end up extravasating into tumors. Exploiting the EPR effect requires that the particles stay in circulation long enough to reach the leaky vessels [9].

Passive targeting by the EPR effect is usually not sufficient to ensure that the necessary amount of drug delivery carriers end up in the tumor. To increase drug delivery, additional active targeting can be applied. Examples of targets are over-expressed receptors, or the release or activation of drugs and carriers triggered by local external or internal cues.

2.2 Tumor associated ECM

The extracellular matrix is the environment that surrounds cells, and consists of macromolecules made up of protein, proteoglycans, and glycosaminoglycans [16, 17, 18]. The proteins and polysaccharides form an elaborate hydrated mesh, through which nutrients and waste can

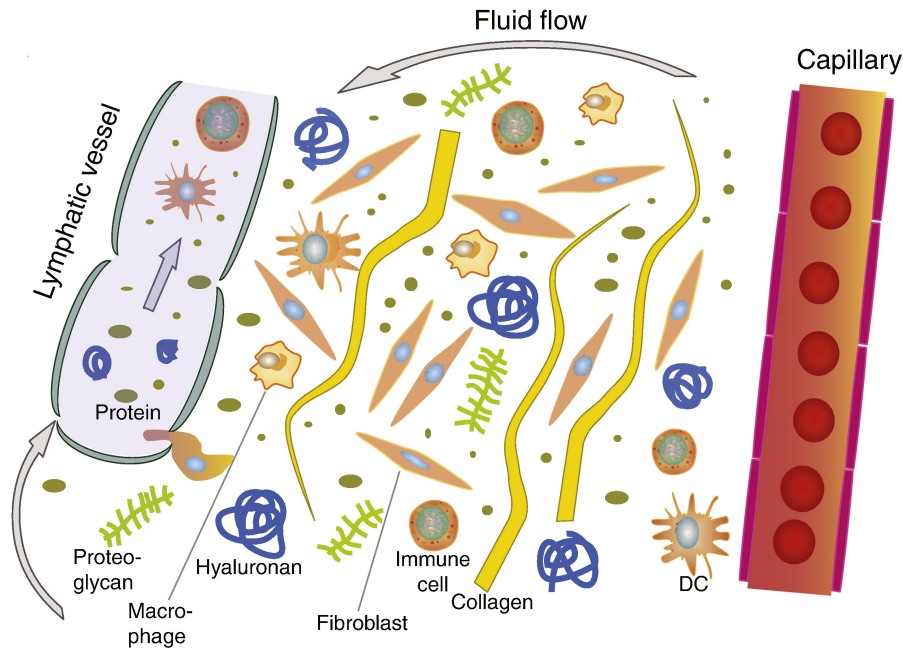


Figure 2.3: Illustration of several components of the (healthy) ECM. Fluid flow from blood vessel through the ECM and to a lymph vessel. Proteoglycans, fibroblasts and immune cells are included. Proteins are represented in the forms of collagen and soluble proteins (small grey circles), while glycosaminoglycans are represented by hyaluronan. Reproduced from [19] with permission from Elsevier (no changes made).

diffuse, and where cells reside, migrate and interact (Figure 2.3). It is the cells which create, secrete and remodel the ECM around them, yet the ECM often provides many of the signals triggering these actions [16, 17, 18].

Lu, Weaver and Werb describe the dynamic role of the ECM in creating the tumor microenvironment by comparing it to the concept of how the local microenvironment has a direct effect on embryonic development [16]. They put emphasis on how the ECM directs almost all cellular processes either directly or indirectly, through junctions, proteins, and receptors, hosting signalling molecules such as growth hormones, or by facilitating angiogenesis or migration. Loss of regulation of ECM structure in tumors can result in tumors that are more rigid due to increased fibrous protein content, remodelling, and cross-linking of those proteins [17]. An increased ECM stiffness can promote cell growth by up-regulating integrin signalling [16].

In addition to being a structural scaffold, the ECM stores many signaling proteins. Among these protein are factors for and against angiogenesis. When the ECM becomes stiffened, it tends to favor activation of pro-angiogenic factors to support endothelial cell growth, as well as invadopodia and cell migration. However a rigid ECM might also lead to up-regulation of enzymes which can break down ECM and the [basement membrane](#) and indirectly compromise angiogenic growth [17].

The basement membrane is a specialized form of ECM which attaches vasculature to the ECM below. The basement membrane is rich in collagen type IV and connective proteins [16].

Both Lu et al. and Pickup et al. suggests that the many ways ECM interacts with the cancer cells and the cancer-associated stromal cells should ensure the ECM a spot among the hallmarks of cancer [16, 17].

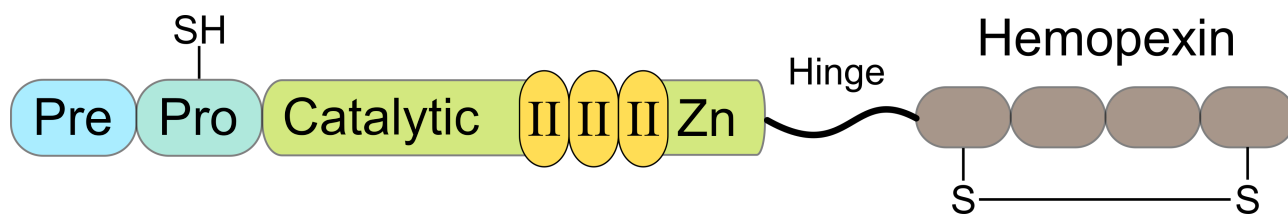


Figure 2.4: Illustration of the structure of MMP2 and MMP9. Pre = signal sequence, pro = propeptide with a free zinc-ligating thiol group (SH), II = collagen binding fibronectin II, Zn = zinc binding site, the first and last repeats in the hemopexin site are linked by a disulfide bond. Adapted with permission from [24]

with permission from Elsevier.

2.3 Matrix metalloproteinases

[Matrix metalloproteinases \(MMPs\)](#) are proteolytic enzymes upregulated in almost every tumor [20]. Some MMPs are secreted by cancer cells, others, e.g. MMP2 and MMP9 are secreted by stromal cells, usually as a proenzyme which must be activated [20, 21]. The MMPs can be recruited to, and activated by, cancer cells or other MMPs, and are therefore often located in close proximity to cancer or stromal cells. The main task of MMPs is to degrade proteins, and by doing so they play an important role in cancer development, contributing to processes ranging from angiogenesis to proliferation to metastasis [20]. The MMPs can affect the faith of cells because cells have receptors for structural ECM components such as integrins, and the cleavage and remodeling of ECM proteins will result in changing which binding ligands are presented to the cells, e.g. by revealing cryptic sites. With altered binding sites comes altering of cellular functions and signalling [22].

In general, MMPs are not up-regulated due to genetic alterations (i.e. mutations) of cancer cells. Instead the up-regulation is believed to be due to changes in transcription.

Between the more than 21 human MMPs, virtually all components of the ECM can be cleaved, but this thesis will focus on two of them, MMP2 and MMP9, the structure of which can be seen in Figure 2.4.

MMP2 and MMP9 are expected to be located close to cells as they are activated at the cell surface of the cell that secreted them [20]. Further, MMP2, -9, and -14 are directly involved in angiogenesis, and experiments with MMP2 deficient mice has led to less blood vessels (number and area) as well as slower growing tumors [20, 21]. Mice deficient in MMP9 developed fewer metastatic colonies compared to wild type mice [23]. A cancer with upregulated MMPs is typically more malignant than if MMPs is deactivated or suppressed [16, 17, 20, 22].

2.4 Barriers for drug delivery

2.4.1 Circulation in vasculature

It is essential that a drug delivery carrier stays in circulation for a sufficient amount of time when the targeting is passive (EPR effect) (Figure 2.5, top left). Protein adsorption on the carrier should be minimal for the carrier to remain hidden from the immune cells. Further, when they reach tumor vasculature they are faced with the irregular structure and flow (described in depth in Section 2.1.3) which can be a major obstacle for encompassing delivery to the whole tumor [25]. To facilitate prolonged circulation time, drug delivery carriers are usually coated

with poly(ethylene glycol) (PEG). PEG is a linear molecule which increases the stealth by masking the surface of whatever it is attached to. Without PEG, the surface will quickly be coated by adsorbing proteins which will form a protein corona. These proteins include opsonin factors which induces complement activation and removal of the carriers by immune cells [26, 27]. The sterical hindrance provided by PEG can also reduce aggregation of the carriers [28].

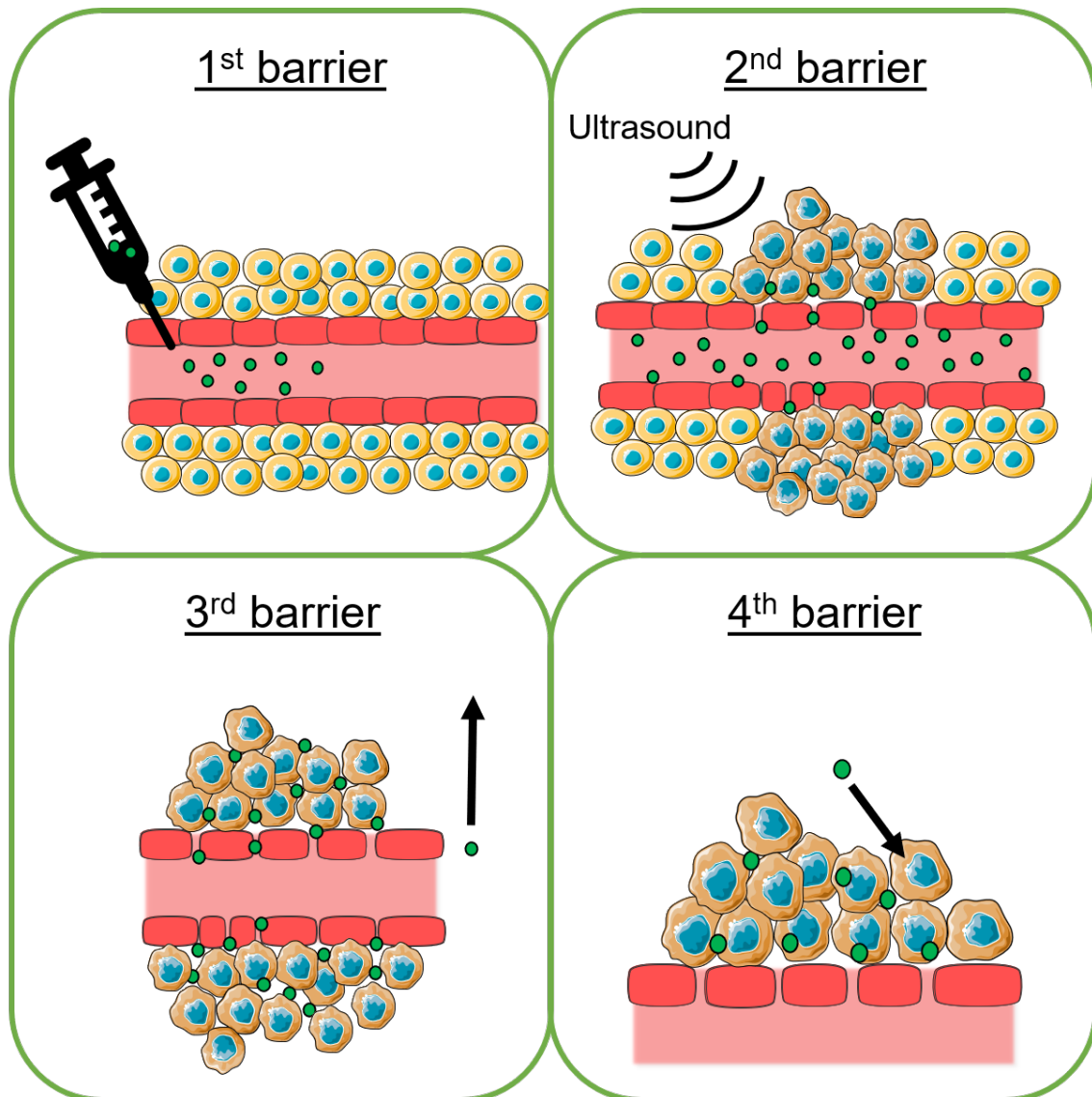


Figure 2.5: 4 barriers that the NPs have to overcome to ensure a successful drug delivery to cancer cells. The first barrier is staying in circulation, the second is extravasation, the third is travelling from the vessel into the tumor ECM, and the fourth is cellular uptake. Not shown is cavitating microbubbles to increase extravasation. Illustration by the author using Servier Medical Art ©.

2.4.2 Extravasation

The second barrier in Figure 2.5 illustrates extravasation, the escape of NPs from blood into tumor ECM. Hashizume et al. imaged openings between the vessel lining cells, holes through the lining cells, and *endothelial fenestrae*, by scanning electron microscopy [25]. The openings

had sizes varying from 0.2-0.9 μm for intracellular holes to 0.3-4.7 μm for intercellular openings. Endothelial fenestrae were observed to be only 50-80 nm. The intra- and intercellular holes observed by Hashizume et al. indicates that the particles used here should have ample space to extravasate, but it should be emphasized that the data is collected from a cancer line which is known to have highly leaky vessels [25]. Particles can extravasate due to diffusion (concentration gradients) or convection (pressure gradients). Since tumors usually display an elevated interstitial fluid pressure, the convection gradient in tumor and tumor vasculature is directed out of the tumor interstitium. The mechanism behind passive extravasation is therefore diffusion [29]. Since diffusion is slower for larger sized entities, it has become the focus of many to increase extravasation by actively targeting developing blood vessels or by applying external cues, e.g. thermal, electromagnetic or acoustic radiation [30]. The spatial and temporal heterogeneity of vasculature within a tumor also means that some areas of the tumors are poorly vascularized, and the NPs might have to penetrate far from the blood vessel they extravasated from. This is discussed next.

2.4.3 Transport through tumor ECM

Once extravasated the carriers must travel through the tumor ECM and interstitial fluid to reach all cells (Figure 2.5), as even just a couple of surviving cells could regrow a full tumor after treatment [2]. The diffusion gradient for NPs delivered intravenously is necessarily directed from the blood vessels and into tumor ECM, and is the driving force for transport through the tumor ECM. As mentioned, due to the enhanced permeability of tumor blood vessels and lack of functional lymph vessels to remove debris, the interstitial pressure is much higher compared to healthy tissue. The high interstitial pressure also hinders convection of NPs into the tumor ECM once extravasated. Further, dense structural components such as collagen contribute to low diffusion throughout the tumor by sterical hindrance [31]. Poor vascularization leads to large distances which the carriers have to traverse to get from blood vessels to cells [32]. Other hindrances to diffusion through the ECM are glycosaminoglycans and cells, and the distance which needs to be travelled for the carriers increases as they have to follow a tortuous path (i.e. zig-zag around cells and other molecules).

2.4.4 Cellular uptake

The final frontier to be crossed is the cellular membrane of the cancer cells (Figure 2.5). If drug delivery vesicles are to be taken up by cells, they need to either be in very close proximity to the cell membrane or to activate endocytosis by binding to membrane proteins such as clathrin or caveolin [33]. For many drugs their detrimental effects on the cell occurs when they reach the nucleus [2]. There are several ways that drugs loaded in vesicles can end up inside the cytoplasm. If the molecules are released from the carrier outside cells, they can either diffuse through the membrane if they're small and non-polar, or be engulfed by cells by phagocytosis or pinocytosis, or by the molecules binding to membrane transport proteins [1]. Controlled release of the drug outside the cell only in the tumor can be challenging. Releasing drugs outside cells also increase the risk of them being cleared by immune cells before killing any tumor cells. Therefore, the goal is often for the entire nanoparticle carrier to be taken up by the cell, before the drug is released intracellularly. Uptake of the drug delivery carrier is highly dependent on cell-carrier interactions, typically mediated by charge and surface structures and components (proteins etc). Indeed, the PEG coating which protects the vesicle from serum proteins and

immune cells can also hinder uptake in the target cells due to the negative surface charge shared by PEG and cell membranes. High degrees of PEGylation are shown in literature to reduce uptake by cells [34].

Typically, once inside an endosome, there are still problems to overcome, such as endosomal escape and avoiding efflux proteins, but this is beyond the scope of this thesis.

2.4.5 Additional challenges

In addition to the four barriers described above, the NPs have to avoid degradation due to adsorbing proteins and immune cell in all compartments they enter. Any adsorbing proteins could lead to increased elimination by the body, or a reduction of the effect of the treatment. Further, low tumor blood supply, heterogeneous vessel coverage and hypoxic tumor areas can limit drug distribution, and cells in nutrient deficient areas are known to develop drug resistance [35].

2.5 Nanoparticles for drug delivery

Nanotechnology is the area of science that observes and exploits the change of properties of materials when reducing size causes surface effects to dominate over bulk effects. The large surface to volume ratio allows for the creation of a highly reactive structure. In medicine, one of the major focus areas of nanotechnology is to improve on existing, or create novel, solutions to deliver drugs to their target site, and thereby avoid systemic distribution of the drug, which might harm healthy parts of the body.

Many platforms of nanomedicine have been explored, including (but not limited to) metal beads, lipid compartments (micelles, liposomes, etc.), protein particles, polymer structures, dendrimers, nanotubes, and viral carriers [4, 7]. The diversity in materials enables tailoring of shape, size, surface functionalization, and loading of e.g. drugs, fluorescent markers, contrast agents or targeting molecules for therapy, diagnostics or a combination.

Loading a drug in a compartment hides it from proteins in the blood and the body's immune system and, depending on the properties of the vesicle, can cause it to end up at a different location compared to the free drug, e.g. by utilizing the EPR effect. The primary reason for loading the clinically approved cancer drug doxorubicin in a sterically stabilized liposome was that free doxorubicin tended to accumulate in the heart. That meant that the dose and frequency of injection of the free drug was strictly limited by the harm inflicted on the heart. By encapsulating the drug into a liposome which did not accumulate in the heart, the dose could be increased, ultimately leading to better treatment of the cancer [36].

A multivariate analysis of tumor uptake of nanoparticles for drug delivery over the last couple of decades found that so far, encapsulating drugs had only lead to a median of 0.7 % of the injected dose ending up in the tumor. It follows that encapsulation is not enough to achieve sufficient delivery, and therefore active targeting should be added. One way of increasing tumor uptake is by the stimulation of microbubbles by ultrasound. This is described next.

2.6 Ultrasound

Sound is the propagation of energy, as pressure waves, through a medium. The pressure waves cause molecules to vibrate and thereby the medium to contract and expand. Soundwaves are

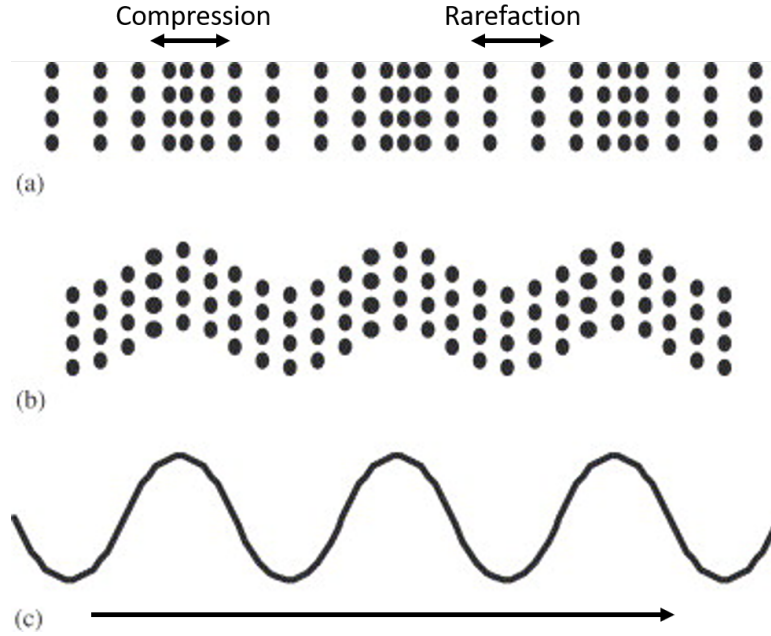


Figure 2.6: (a) Longitudinal, (b) shear, and (c) sinusoidal waves. (a) and (b) are polarizations, while (c) describes the shape of the wave. Adapted from [38] with permission from Elsevier. Added info: Arrows showing areas of compression and rarefaction by the longitudinal wave (top), and an arrow indicating direction of wave (left to right, bottom).

described by their frequency, velocity (c) and amplitude, and they can be continuous or pulsed [37].

The velocity, or rate of propagation, c is given by

$$c = \sqrt{\frac{K}{\rho}}, \quad (2.1)$$

where K is the elasticity of the medium and ρ is the density [37].

The frequency (f) of the wave is related to the wavelength (λ) and velocity, as:

$$f = \frac{c}{\lambda}. \quad (2.2)$$

The amplitude describes either the maximum distance a vibrating molecule travels from its resting position due to the pressure wave, or it can describe the local maximum (or minimum) pressure.

Waves can be longitudinal or shear, and describes how molecules vibrate in relation to the direction of the wave. This is seen in Figure 2.6, where a wave moves in the horizontal direction. Particles in a longitudinal wave oscillates in the horizontal direction (left-right), parallel to the sound wave, and in the perpendicular direction (up-down) relative to the sound wave in a shear wave.

Sound waves mainly cause longitudinal vibrations of soft tissue, as the perpendicular vibrations in shear waves are only possible in highly ordered materials such as bone or other solids [38].

The displacement of a molecule, $y(x,t)$, in the longitudinal sound wave, is given by

$$y(x,t) = A \cos\left(\omega\left(t - \frac{x}{c}\right)\right), \quad (2.3)$$

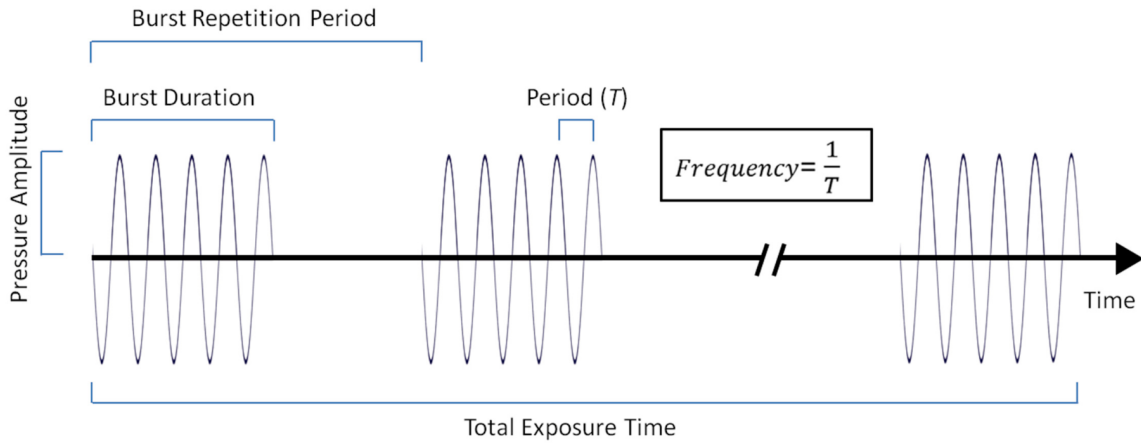


Figure 2.7: Sinusoidal, pulsed US wave. A pulse is called a burst in the figure. Areas of compression are above the x-axis (time axis) and areas of rarefaction are below. Reprinted from [39] with permission from Elsevier.

where A is the amplitude of the oscillations, ω is the angular frequency, t is time, x is the distance from source, and c is the speed of the wave.

When the frequency of the pressure waves exceeds 20 kHz, they are called ultrasound [40, 38, 41]. Although ultrasound is most common in diagnostics, it can be used for therapy as well. Specifically, it is possible to use focused US to increase the permeability of tumor blood vessels to enhance uptake of nanoparticles in tumors and to disrupt the [blood brain barrier \(BBB\)](#) [42]. Therapeutic ultrasound usually has a frequency of 1 MHz, while diagnostics often use higher frequencies, typically up to 5 MHz.

2.6.1 Mechanical index and cavitation

Acoustic power and intensity are measures of the strength of the US wave, with power being the total energy passing through a cross sectional area per unit time, and intensity defined as energy per unit area per unit time, and therefore the intensity depends on the ultrasound beam width [43]. If the US is pulsed (Figure 2.7), the intensity is zero between pulses. Acoustic power is constant throughout the sample only if there is no loss in the medium, but due to attenuation (deflection, divergence and absorption), when the US wave travels through soft tissue, some power is lost. Sometimes the term "acoustic pressure" is used as the force which an area treated experiences, and depends on acoustic power at the source as well as properties of the media the wave travels through, and the distance travelled [44].

[Mechanical index \(MI\)](#) is a measure of acoustic power, given by the peak negative pressure (PNP) divided by the square root of the frequency (f) (Equation 2.4) and describes non-thermal effects on the system, such as cavitation and streaming [44].

$$MI = \frac{PNP}{\sqrt{f}}. \quad (2.4)$$

Although the MI is a unit less number, the PNP is given in MPa and the frequency in MHz. When gas bubbles experience an acoustic field, e.g. US, the oscillating pressure can cause gas to [cavitate](#), i.e. form bubbles. The bubbles formed can be either from endogenous gas, or from

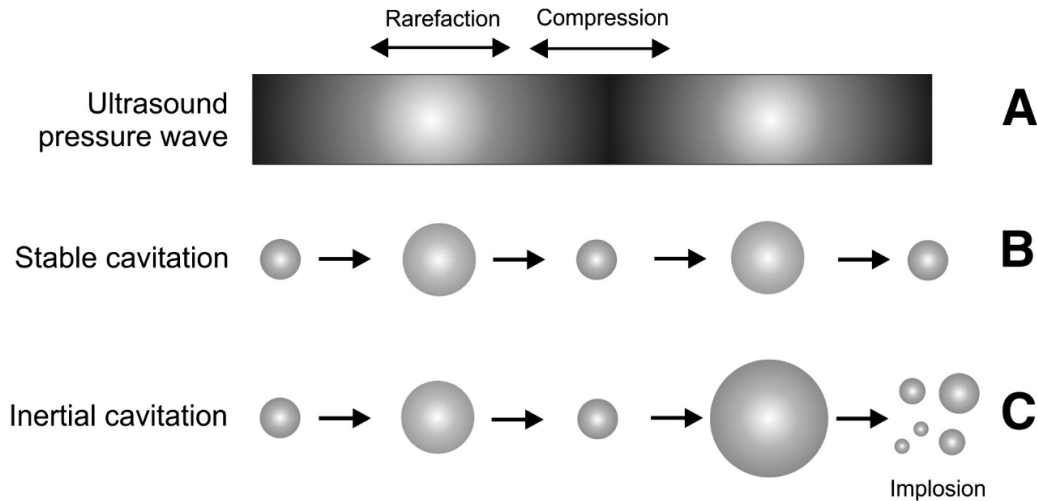


Figure 2.8: Illustration of stable (b) and inertial (c) cavitation of microbubbles when exposed to a longitudinal pressure wave (a). Whether MBs behave by stable or inertial cavitation depends on the amplitude of the US, and therefore on the degree of compression and rarefaction, as well as of the frequency of these. Reprinted from [46] with permission from Elsevier.

injected microbubbles. The size of the bubbles will vary with acoustic pressure, i.e. they will be compressed under high pressure and expand under low pressure (Figure 2.8).

Under a certain acoustic pressure (depending on the system), stable cavitation occurs, i.e. stable compression and expansion of the bubbles (Figure 2.8C). Stable cavitation can cause shear stress on the nearby blood vessels and thereby increase vasculature permeability. If the pressure increases above a certain pressure, the bubble can implode and emit microjets. Implosions and microjets have been found to breach cell membranes, increase local temperature and create reactive oxygen species which all can be harmful to nearby cells [45]. Whereas stable cavitation will continue for the duration of each pulse, the time of implosion depends on gas bubble size and the mechanical index of the ultrasound applied.

2.6.2 Radiation force

Radiation force is caused by momentum transfer from the US wave to the medium, in the direction of wave propagation, and the force increases with frequency and intensity of the US wave [42]. If the radiation force is strong enough, it is believed that the pressure waves can help particle convection in the tissue either by pushing directly on the particles, or by causing the extracellular fluids to stream and consequently transport particles [41]. Another possibility is that the ultrasound can physically alter the molecules of the ECM, or their orientations and distributions, and thereby affect how far NPs can travel into the tissue [42]. These alterations could be permanent, depending on the force of the US wave, or it could be primarily a temporal effect of the tissue expanding and compressing locally due to the pressure wave. Lammertink et al. found that the acoustic pressure force could push microbubbles towards blood vessel walls, which would increase the interactions between cavitating microbubbles and endothelial cells [47].

2.6.3 Thermal effects

When US interacts with tissue and fluids in the body, some of the energy will be absorbed and cause heating locally [42, 48]. The degree of heating will increase with US intensity and duration. The heating might enhance drug delivery, as drug release from carriers, blood flow, cell wall permeability and diffusion can all increase with temperature [42, 41].

2.7 Fluorescence

Fluorescence is the phenomenon where a molecule emits energy in the form of a [photon](#). A fluorescent molecule, or a fluorophore, must be in an excited energy state (e.g. S1 in [Figure 2.9](#)) before it can fluoresce. A fluorophore can be excited by the absorption of a photon. The photon must be of an energy which matches an energy gap between states in the molecule [49]. The emitted photon is usually of lower energy than the absorbed photon, as some of the absorbed energy is lost to e.g. heat radiation (purple arrows). The difference in energy between an emitted photon of lower energy than the absorbed photon is known as the Stokes shift [49]. A sufficiently large Stokes shift is necessary for the separation of incident light and the fluorescence signal.

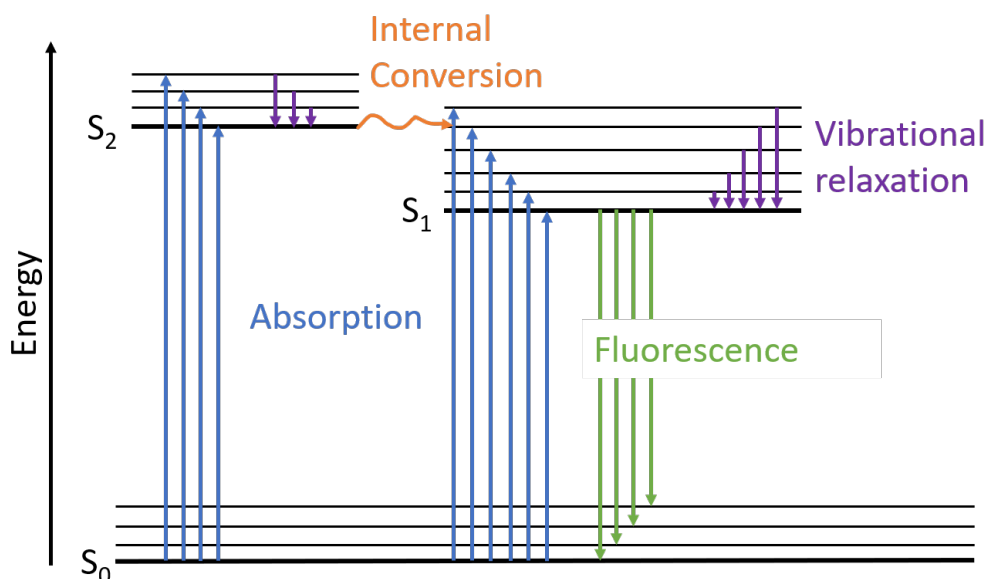


Figure 2.9: Diagram showing absorption (blue), fluorescence (green), internal conversion (orange), and vibrational relaxation (purple). For a fluorophore to emit a photon, it must first absorb a photon with an energy that matches the energy difference of two allowed states of the molecule. If two states have almost the same energy, internal conversion might occur, shown here from the lowest mode of S_2 to a high S_1 vibrational state (orange squiggly arrow). Vibrational relaxation happens when the molecule loses energy to the surrounding due to rotation or vibrations.

2.7.1 Two photon excitation and second harmonic generation

A molecule can absorb two or more photons if the sum of their energy matches the energy difference between two allowed energy states in the molecule [50]. This can result in the release of one photon with energy near to the sum of the two absorbed photons. This phenomenon is exploited in multiphoton microscopy and second harmonic generation.

Two photon laser scanning microscopy (TPLSM) utilizes the possibility that a molecule can be excited to a higher energy state by absorbing two photons. The closer the two photons arrive in time to the same location the higher the probability that they both excite the molecule via a virtual intermediate state [50]. TPLSM is therefore achieved using a pulsed laser light source. The two photons can be of the same energy, but does not have to be. The excited molecule can return to its ground state by emitting a photon with an energy equal to or less than the sum of the two absorbed photons (figure 2.10a). TPLSM allows for a molecule to be excited in the near infrared range, and to fluoresce in the visible range. This is useful in biological tissues where water has a high absorption in the visible range.

Second harmonic generation (SHG) is similar to TPLSM in the sense that it absorbs two photons of the same energy and emits a single photon of twice that energy (Figure 2.10). The main difference is that it is no excitation of fluorescent molecules, and therefore the emitted photon is exactly the sum of the two absorbed photons. SHG is a non-linear optical effect and occurs only in structures without inversion symmetry. Examples of such structures found in biological samples are all surfaces and interfaces, and non-centrosymmetric structures such as ordered fibrillar collagen. Setting the focal depth below the surface avoids interference from the tissue surface [50, 51].

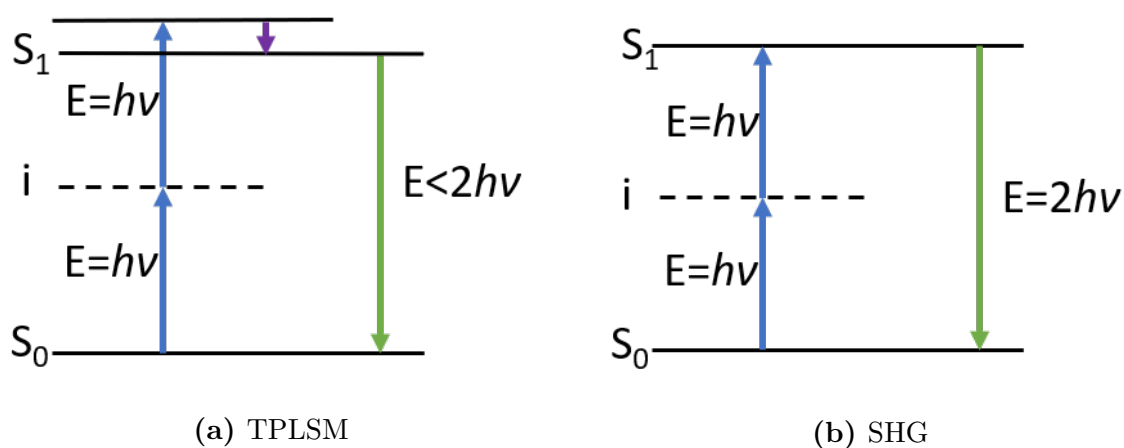


Figure 2.10: Absorption (blue arrows) of two photons with the same energy, and emission (green arrow) of a single photon with energy less than (a: TPLSM) or equal to (b: SHG) the sum of the two absorbed photons. The molecule is excited from the ground state (S_0) to a higher energy state (S_1) via a virtual intermediate state (i). It is important to note that the photons are absorbed simultaneously, and that the intermediate state is not a real, allowed energy state, but a short lived scattering state. Adapted from [50].

2.8 Confocal laser scanning microscopy

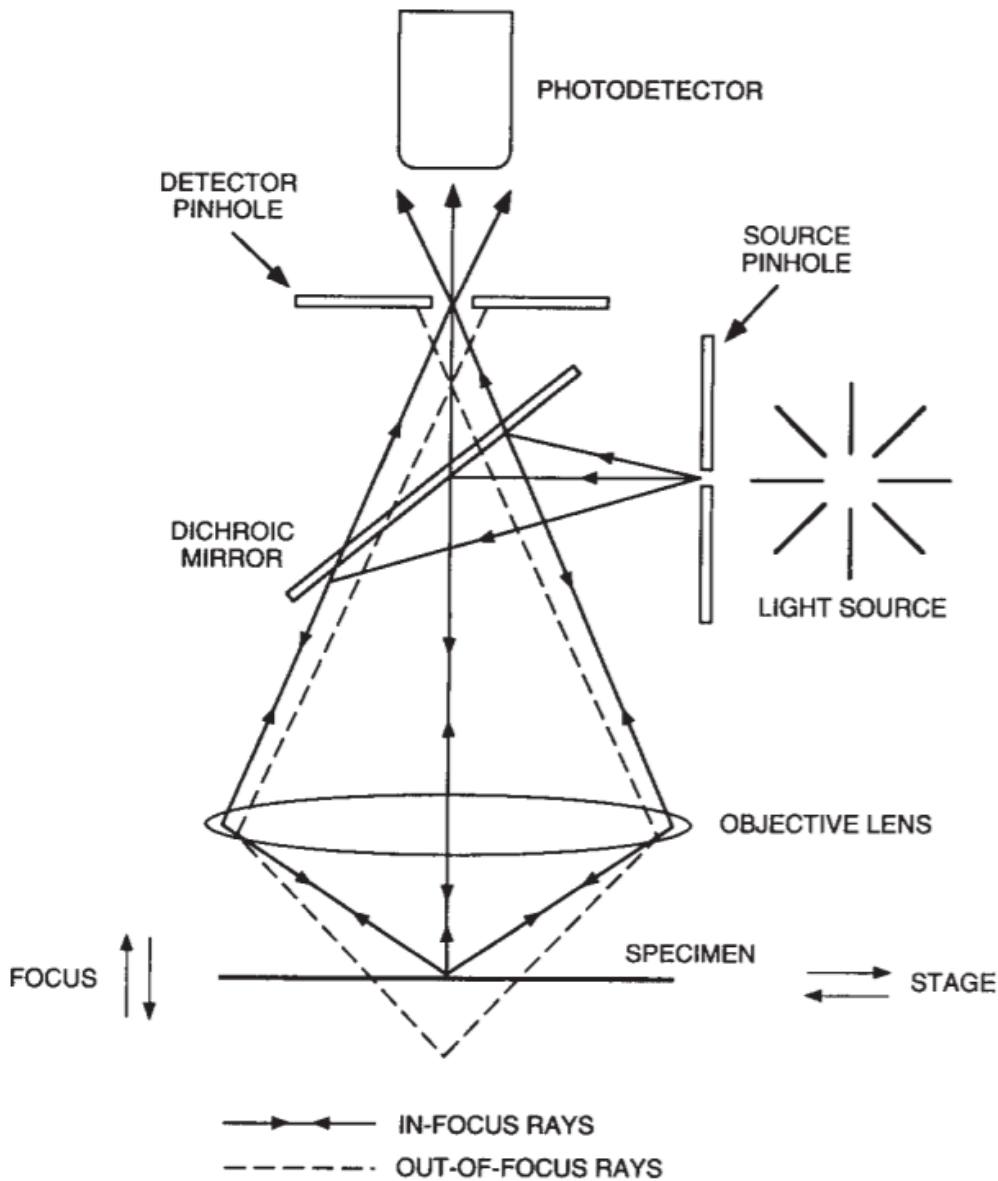


Figure 2.11: CLSM principle. Reprinted from [52] with permission from Springer Nature.

Confocal laser scanning microscopy (CLSM) is a popular microscopy technique for measuring fluorescence in tissue. Unlike conventional epifluorescent microscopes, which illuminates and collects signal from the entire sample simultaneously, confocal microscopes use lasers, mirrors, apertures, and lenses to achieve a very narrow **depth of field**. Placing the aperture in front of the detector in the conjugate plane of the in-focus plane leads to increased resolution by a factor of $\sqrt{2}$ compared to a conventional epifluorescent microscope [53]. Mirrors and filters are applied to choose the appropriate wavelength(s) for excitation and detection. The focal plane can then be moved in the x, y, and z directions, and the signal collected can be used to build 2D and 3D images using a computer software [53]. Movement of the focal plane is done either by scanning the focused laser beam across the sample using mirrors, or by moving the sample

using a piezo-electric stage. CLSM provides better resolution than a wide-field microscope, especially in the direction of illumination, as the sample is only excited locally and signals from out-of-focus areas are reduced [53, 52]. The out-of-focus fluorescence distributions are removed by inserting an aperture, namely a confocal pinhole (figure 2.11), which blocks the out-of-focus light [51]. A larger pinhole opening gives a thicker optical section, and therefore more information, but when the optical section becomes larger than the depth of field (focused region), resolution is lost due to interaction between out-of-focus light and in-focus light, causing the out-of-focus light to blur the image created by light from the in-focus region. In figure 2.11 light is reflected (back scattered) from the sample and directed to the detector. Some light will be forward scattered (not shown in the figure), and can be detected using mirror systems or other detectors.

While the pinhole size affects the amount of light that reaches the detectors, band pass filters are used to choose the wavelengths that are detected. Choosing the correct filter to match the fluorophore of interest is just as important as exciting with the proper wavelength. If multiple fluorophores are present, a sequential scan can be done with different excitation wavelengths and emission filters. This will give separate images, and by overlaying these images one can build a comprehensive image containing information from the different structures in the sample.

2.8.1 Multiphoton microscopy and second harmonic generation

Multiphoton microscopy uses two or more photons to excite a fluorescent molecule. In the case of two photon excitation, the term [two photon laser scanning microscopy \(TPLSM\)](#) is used. SHG works similarly to TPLSM, but emits photons with exactly double the energy of the two absorbed photons. Imaging by TPLSM and SHG require pulsed lasers for excitation, and both create images by only exciting fluorophores that are in the focal area, eliminating the need for confocal pinholes. This is possible because the probability of out of focus fluorophores being excited by two photons simultaneously is extremely low [52].

2.9 Flow cytometry

Flow cytometry allows for imaging of individual cells. Focusing a sample fluid containing cells to an approximately one cell wide stream, allows for illumination of single cells as they flow past a laser source. The focusing is accomplished by injecting the sample stream into a surrounding stream of sheath fluid. If both streams are flowing smoothly, it is known from fluid mechanics that the streams will not mix, and by adjusting the speed of the surrounding sheath fluid, the thickness of the core stream can be adjusted.

Modern flow cytometers usually contains one to four laser sources with focuses positioned along the sample stream, and a set up of multiple detectors to detect different wavelengths of scattered light. Different cells will scatter light at different angles, commonly divided into small and large angle scattering. Small angle scattering ($0.5-5^\circ$), also known as forward scattering, gives a rough measure of cell size. This can be used to exclude large clusters or small debris from subsequent analysis. Large angle (or side) scattering ($15-150^\circ$) signal amplitude increases with granularity and surface roughness of the cell, and can be used to separate between cell types in a heterogeneous cell population. Further, filters allow for detection of fluorescent molecules or components. Side scattered light and fluorescence are collected at 90° , on opposite sides of the laser excitation angle [54].

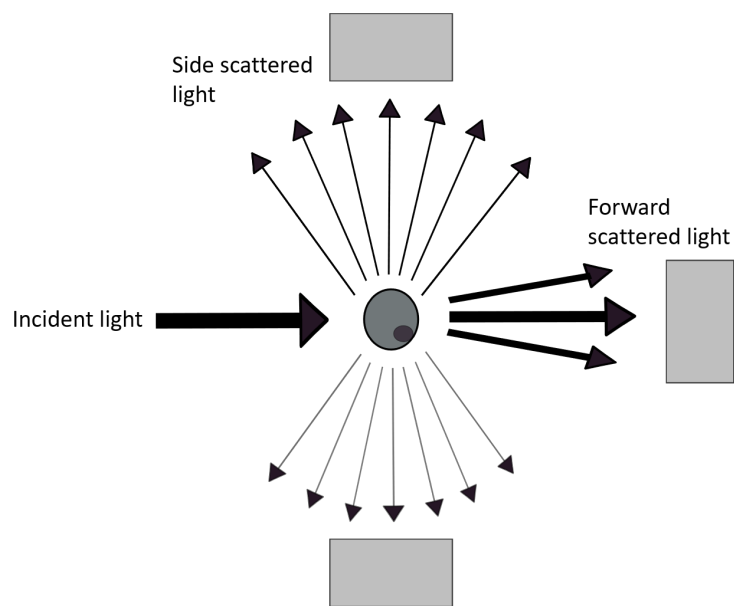


Figure 2.12: Forward and side scattering of light by a cell. Grey boxes represents detector systems. Note that the detector systems not imaged are comprised of multiple dichroic mirrors and detectors which allow for detection of multiple wavelength regions simultaneously. Cells are brought into the focus of the incident light in the direction perpendicular to the paper plane.

Chapter 3

Materials and experimental methods

3.1 Materials

Human prostatic adenocarcinoma (PC3) cells was purchased from American Type Culture Collection. Dubecco's Modified Eagle Medium (DMEM, Gibco) and CellMask (Deep Red plasma membrane staining) was obtained from Thermo Fisher Scientific. Fetal bovine serum (FBS), 4-(2-Hydroxyethyl)piperazine-1-ethanesulfonic acid sodium salt (HEPES), Phosphate Buffered Saline (PBS), penicillin/streptomycin (1:1), thermolysin, and trypsin- ethylenediaminetetraacetic acid (EDTA) solution were purchased from Sigma Aldrich. 75 cm² Tissue Culture Flasks and 12 well plates were obtained from VWR. 8 well microscope slides were purchased from Ibidi. VectaShield® mounting medium with DAPI (4',6-diamidino-2-phenylindole) was purchased from Vector Laboratories (CA, USA). Liposomes with cleavable and uncleavable PEG-chains were prepared at DTU in Denmark. Whole blood (used for teaching purposes) was obtained from St. Olavs hospital.

3.1.1 Liposomal nanoparticles

Three liposomal nanoparticles, "cleavable", "non-cleavable", and "standard" were provided by Viktoria Sereti at DTU, Denmark (Figure 3.1). The cleavable liposome consisted of POPC:Chol:Chol-PCL1:DOPE-Atto 488:DPPE-Atto 700 in molar ratios of 59.6:35:5:0.2: 0.2. The non-cleavable liposome consisted of POPC:Chol:Chol-PEG:DOPE-Atto 488: DPPE-Atto 700 in molar ratios of 59.6:35:5:0.2:0.2. The standard liposome consisted of HSPC:Chol: DSPE-PEG:DOPE-Atto 488:DPPE-Atto 700 in molar ratios of 56.4:38.2:5.3 :0.2:0.2 (see expansion of chemical abbreviations in Table 3.1). The standard liposome has the same lipid composition as Doxil, a PEGyated liposome clinically approved for delivery of the chemotherapeutic agent Doxorubicin [36]. The cleavable liposome has PEG-chains attached to cholesterol by an amino acid linker sequence. The sequence is cleaved by the enzymes MMP2, MMP9, and thermolysin. The non-cleavable NPs are similar to the cleavable, except that the PEG can not be cleaved off. In one control experiment a fourth NP was used to confirm the activity of thermolysin (described later).

3.1.2 Atto 488 and Atto 700

The two fluorophores Atto 488 (peak excitation wavelength = 501 nm, quantum yield = 0.8), and Atto 700 (peak excitation wavelength = 700 nm, fluorescence quantum yield = 0.25), are

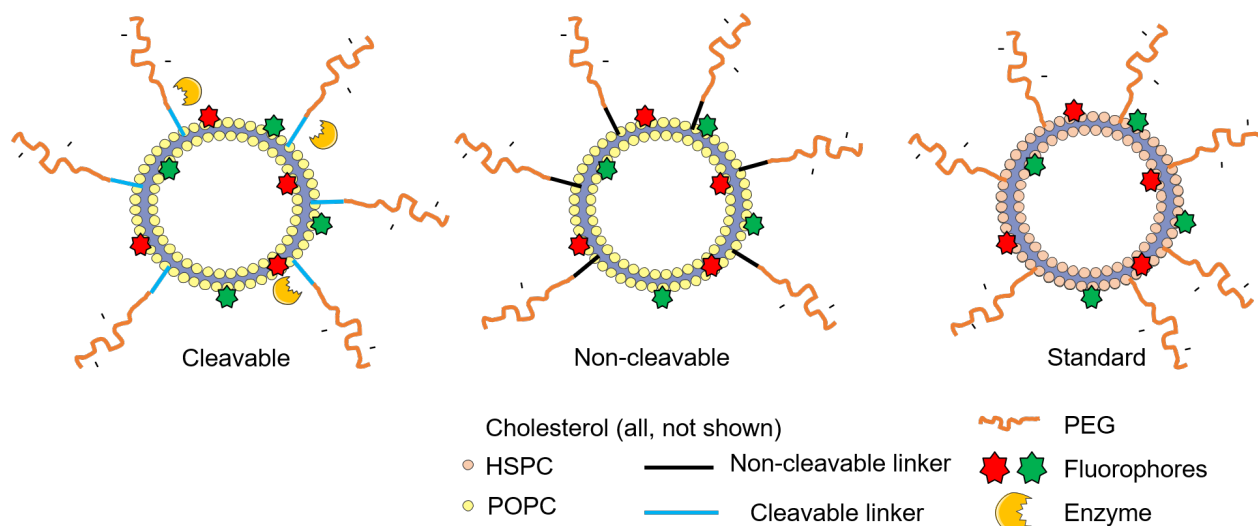


Figure 3.1: Illustration of the three liposomal nanoparticles used in this thesis. Made by the author using Servier Medical Art .

linked to lipids (DOPE and DPPE, respectively) by covalent bonds at the hydrophilic head group. The lipids are incorporated into the nanoparticles, leaving the fluorophores at the water-lipid interface. When imaging the dissected tumors they were full of blood and water, which have high absorbance of visible light. Atto 700 allows for imaging in the near infrared spectrum, where water and hemoglobin do not have a high absorption.

Table 3.1: Abbreviations of the compositions of the liposomal nanoparticles. Atto 488 and Atto 700 are covalently linked to the headgroups of DOPE and DPPE, respectively.

Abbreviation	
HSPC	Hydrogenated soybean phosphatidylcholine
POPC	1-palmitoyl-2-oleoyl-sn-glycero-3-phosphocholine
Chol	Cholesterol
Chol-PEG	Cholesterol with polyethylene glycol (PEG) chain
Chol-PCL1	PEG linked to Chol by MMP2/-9 specific amino acid sequence
DSPE-PEG	1,2-distearoyl-sn-glycero-3-phosphoethanolamine-N-[amino(polyethylene glycol)-2000]
DOPE Atto488	1,2-dioleoyl-sn-glycero-3-phosphoethanolamine with Atto 488
DPPE Atto700	1,2-dipalmitoyl-sn-glycero-3-phosphoethanolamine with Atto 700

3.1.3 Preparation of solutions

Cell culture growth medium

Growth medium (GM) was prepared by adding 10% v/v FBS and 1% v/v Penicillin Streptomycin, stored at 4°C. Unless otherwise stated, the growth medium was heated for 15 min at 37°C before being added to cell cultures or nanoparticles.

HEPES buffer saline

HEPES buffer saline was prepared by diluting HEPES buffer (50 mM) and NaCl (100 mM) in

distilled water. The pH was adjusted by adding 200 μL 1 mM NaOH to a final pH of 7.

HEPES buffer with salts

HEPES buffer with salts was prepared by adding CaCl_2 (1 mM) and ZnCl_2 (2 μM) to previously made HEPES buffer saline.

Cleaving liposomes by thermolysin

Cleavable liposomes (2.5 mM) were incubated overnight with thermolysin (10 $\mu\text{g mL}^{-1}$) in HEPES buffer with salts.

Liposome dilutions

Prior to experiments liposomes were diluted from stock solutions to the desired concentration in wanted solvent (GM, PBS, or HEPES buffer saline). The stock solutions were gently mixed to ensure a uniform liposome suspension.

3.2 Animal experiment protocol

All animal experiments was done by M. Olsman prior to this thesis. Tumors were induced in the hind leg of immunodeficient mice by injecting 50 μL (3×10^6) PC3 cells (human prostate cancer line) subcutaneously using a syringe. The PC3 tumor cells were allowed to proliferate for 3-4 weeks to let a suitable tumor size form.

Table 3.2: Ultrasound settings. One treatment group received a mechanical index of 0.4, the other received 0.8. The control group did not receive US treatment.

Setting	Low MI group	High MI group
Mechanical index	0.4	0.8
Pulse repetition frequency [Hz]	0.5	0.5
Number of cycles	10 000	10 000
Duration [min]	2	2

3.2.1 Ultrasound setup

To expose the tumor to ultrasound, the mice were put under anesthesia and the hind leg containing the tumor was lowered into a water bath in the far field of the ultrasound transducer, as described previously in [55]. The US settings are described in Table 3.2. Prior to ultrasound treatment, nanoparticles, i.e. liposomes with Atto 488 and Atto 700, (100 μL , 6 mM) and microbubbles (100 μL , SonoVueTM, Bracco) were injected intravenously. Control animals only received nanoparticles and no US.

The animals were sacrificed 3 hours after nanoparticle injection. 5 minutes prior to the euthanasia, 100 μL lectin (Ulex europaeus-Atto 594 conjugate, Sigma Aldrich) was injected intravenously to stain the luminal side of endothelial cells of the blood vessels. The mice were imaged using a whole animal optical imager both before and up to 3 hours after US treatment.

After sacrificing the animals, the tumor and major organs were dissected out, weighed and imaged in a whole animal optical imager. The tumor was cut in half, one part being preserved in formaldehyde, the other frozen in liquid nitrogen and stored at -80°C . From the frozen tumor, sections were cut at 5 levels (300 μm apart), and from each level 4 sections with a thickness of 25 μm were obtained and attached to microscope slides. The slides were subsequently stored

at -20°C . An additional section ($4\ \mu\text{m}$ thick) was cut from each level and stained with HES (Hematoxylin Eosin Saffron) to be able to view the tissue in an optical microscope.

3.3 Cultivating cells

PC3 cell cultures were maintained in GM at 37°C and 5 % CO_2 . Passaging was done every 3-4 days to maintain the cells in the exponential phase. To passage cells, 5 mL of PBS was added to remove trypsin inhibiting ions. PBS was then removed and 3 mL Trypsin was added and incubated with the cells until all cells had detached from the flask. 9 mL growth medium was added to stop the trypsin activity, the cells were resuspended and 10 mL transferred to a centrifuge tube. A drop of suspension was also added to a Bürker chamber for counting cell concentration. The cell suspension was centrifuged at 1500 rpm for 5 min, the supernatant was removed and the pellet was resuspended in growth medium to a concentration of 1×10^6 cells/mL. Cells were seeded in new T75 flasks, or further diluted to suitable concentrations for seeding in 12 well plates or 8 well microscopy slides. In addition to the passaging, growth medium was changed once per week, and on the day prior to experiments.

3.4 Fluorescence emission spectroscopy of nanoparticles

Stock solutions of standard, cleavable and non-cleavable liposomes in PBS (1 mL, 1 mM) were prepared. From each stock solution, dilutions were created (ranging from 0.005 mM to 1 mM) and the fluorescence intensity of the two encapsulated fluorophores (Atto 488 and Atto 700) was measured for each dilution. 3 replicates of each concentration were measured, and averaged. Control measurements of pure PBS were performed. Average PBS values were subtracted from the average fluorescent intensity for each concentration. The fluorophores were excited, and their emissions detected, in a SpectraMax i3x Multi-mode detection platform (Molecular devices). The wavelengths for excitation and emission are described in Table 3.3. The instrument required a 25 nm interval between excitation and emission wavelengths.

Table 3.3: Excitation and emission wavelengths used in plate reader to detect Atto 488 and Atto 700, respectively. Atto 488 was used to image the NPs by confocal microscopy, and Atto 700 was used to image the NPs in the tumor in the whole animal optical imager.

Fluorophore	Excitation wavelength	Emission range
Atto 488	480 nm	505-650 nm
Atto 700	680 nm	705-850 nm

3.5 Nanoparticle behaviour in blood and serum

Aggregation of NPs in buffer, serum and whole blood was imaged using confocal microscopy (Leica TCS SP8), with a 40X/1.10 water immersion objective, and excited by a white light laser using the same settings as for tumor tissue microscopy of Atto 488 (described below) Red blood cells were imaged in a bright field channel simultaneously. Standard, non-cleavable, and cleavable liposomes were diluted in separate eppendorf tubes in PBS and HEPES respectively

(0.5 mM, 200 μ L). In new tubes the nanoparticles in PBS or HEPES were mixed with whole blood or serum (2:1) (see Table 3.4. From each tube, a 20 μ L drop was transferred to a microscope slide and a cover slip was applied. A time series of images were taken and assembled into approximately 30 second long movies. The degree of aggregation was assessed qualitatively by a custom-made MATLAB script which connected neighboring pixels (4 nearest neighbors).

Table 3.4: Experimental ratios mixing NPs in buffers and/or blood and serum. NPs were mixed 2:1 with serum or whole blood. Pure NPs in either buffer were also imaged.

Mixing NPs with serum or whole blood	NP in PBS (0.5 mM)	NP in HEPES buffer saline (0.5 mM)	Serum	Whole blood
NP in PBS (0.5 mM)	1	-	2:1	2:1
NP in HEPES buffer saline (0.5 mM)	-	1	2:1	2:1

3.6 Confocal microscopy of tumor sections

Tumor sections from animal experiments were imaged by confocal microscopy, TPLSM and SHG (Leica TCS SP8).

Prior to imaging a section was thawed in room temperature, and a sufficient amount of VectaShield® mounting medium with DAPI to cover the tumor section was applied (typically 1-2 drops). The section was covered with a coverglass and sealed with nail polish. The nail polish was allowed to dry before the slide was inserted onto the microscope stage, and imaged.

All sections were imaged in a Leica TCS SP8 confocal microscopy with a [white light laser \(WLL\)](#) (Leica Microsystems, Germany) and a [multiphoton \(MP\)](#) (Chameleon Vision-S, Coherent, USA) laser, using a 40X/1.10 water objective.

Laser, detector, and imaging settings were tuned to optimize image quality (see Table 3.5) using the software Leica Application suite (1997, Leica Microsystems CMS). The excitation intensity was chosen so that only a few pixels were saturated. This was done to utilize the whole greyscale, and thereby get as much information as possible.

Each feature (collagen, nuclei, blood vessel, nanoparticles) was imaged in separate channels. A compound image, made by merging the channels can be seen in Appendix C, Figure C.3. For the standard and non-cleavable nanoparticles, excitation and detection wavelength settings were optimized to ensure that optimal signal was attained in case of altered properties. Both transmitted and reflected SHG signal of collagen was obtained by TPLSM, with settings described in Table 3.2. Transmitted SHG signal from collagen was detected by a condenser lens with a NA of 0.9. For the specialization project, only the backward scattered SHG signal was collected. Due to a human error, the 0.9 NA condenser lens which collected the transmitted signal was on an occasion switched with a 1.4 NA oil immersion condenser lens. It was not possible to see which images were taken with the wrong condenser lens. To assess the effect of using the wrong condenser lens, images with high and low SHG signals (i.e. different amounts of collagen) were taken with both condenser lenses. No difference could be seen between the images taken with different condenser lenses. Prior to each imaging session full Köhler illumination was achieved.

During imaging, the tissue section was viewed in the ocular to find stained blood vessels. The blood vessel channel was primarily searched, and blood vessels were imaged without knowing whether nanoparticles were present. This yielded an overview of the blood vessels in each section and the nanoparticles in and around the blood vessels, as well as nuclei and fibrillar collagen. However, nanoparticles that were not associated with blood vessels, e.g. whenever the blood vessels poorly perfused or were blocked by NPs at the time of lectin staining, would not be imaged when following the procedure mentioned above. Therefore the nanoparticle channel was also scanned to look for areas with a prominent amount of nanoparticles (Figure 3.2).

Table 3.5: Software settings for sequential imaging. All images captured using a bidirectional scan of speed 100, with a line average of 8, between frames. Transmitted and reflected SHG signal from collagen was detected.

Parameters	Collagen	Nuclei (DAPI)	Blood vessels (Atto 594)	Liposomes (Atto 488)
Laser	MP	MP	WLL	WLL
Excitation wavelength [nm]	890	730	601	501
Excitation intensity [%]	22	8	15	15
Emission filter range [nm]	435-455	400-450	616-656	516-556
Detector gain [%]	100	100	97.3	100
Optical section [μm]			4	4

3.6.1 Tile scans

Multiple images (tiles) were taken of a larger area of the tumor, to get an overview of the distribution of collagen, blood vessels, nuclei and nanoparticles. The tiles were imaged from edge to edge, in two directions as illustrated in Figure 3.3. The tiles were built to large field images by the microscope software (Leica SP8). The same imaging settings were used as for imaging individual vessels (Table 3.5). In stead of the 40x objective, a 20x objective was used.

3.7 Nanoparticle uptake experiments

3.7.1 Flow cytometry

Cell seeding for flow cytometry

120,000 PC3 cells were seeded into 12-well plates (VWR, Radnor, PA, USA) in growth medium to a total volume of 2 mL. Growth medium was changed after two days. Experiments were performed after three days, when a confluent cell layer was developed.

NP incubation

NPs were incubated with cells at 37°C for 3 hours at concentrations of 0.5 mM and 1.0 mM. An experiment at 4°C was done for the 0.5 mM concentration to evaluate whether uptake was due to endocytosis or leakage of dye.

Flow cytometry of nanoparticle uptake

After incubation with NPs, cells were washed 3 times with 1 mL PBS to remove free NPs. The cells were released from the wellplate by adding trypsin for 2-3 minutes, followed by growth medium which was added to deactivate the trypsin. The cell suspension was put on ice before being transferred to flow cytometry tubes. Nanoparticle uptake was evaluated by flow cytometry. Atto 488 was excited by a blue laser (488 nm) and detected at 525 nm (with a 40 nm band pass filter). Gating to exclude dead cells, debris, and clusters was applied based on 3 control sample populations. Control samples consisted of cells in growth medium, without any nanoparticles added. The same gating was applied to all flow cytometry histograms, which were analyzed in Kaluza software (version 1.5, Beckman Coulter, USA).

3.7.2 Microscopy of nanoparticle uptake

15,000 cells in 300 μ L GM were seeded in each well of an 8-well microscope slide. Growth medium was changed after 2 days. Incubation with lipid NPs was performed after 3 days. NPs not taken up by cells were washed away with PBS (3x). Cell membranes were stained with CellMask (2.5 μ g ml⁻¹) for up to 5 minutes. The CellMask was removed and the cells were washed with PBS once prior to imaging. CLSM (Leica TCS SP8, using a 40X/1.10 water objective) was used to obtain z-stack images of cell membranes (CellMask deep red) and NPs (Atto 488).

Table 3.6: Image settings for in vitro nanoparticle uptake.

Microscopy settings	NP (Atto 488)	CellMask (Deep Red)
Excitation wavelength [nm]	505	650
Detection range [nm]	520-580	ca 670
Optical section [μ m]	1	1
Time gating [ns]	0.3-6.9	0.3-6.8

3.8 Image processing and analysis

To enable comparison, the analysis of sections containing non-cleavable and standard NPs were analyzed in the same manner as the cleavable liposomes analyzed during previous project work.

The exception is that transmitted collagen SHG signal was included in addition to the reflected signal. Collagen comparisons might therefore be unfair.

3.8.1 SP8 microscopy image post-processing

Images were processed in Fiji (a distribution of ImageJ, version 2) [56, 57]. Raw NP, blood vessel, forward and reverse collagen images were thresholded using Fiji's automatic "Triangle" threshold, after evaluating the "Triangle" to be the most suitable of the automatic thresholds. A **region of interest (ROI)** of the thresholded NPs were created and stored (Figure 3.4c). A distance map was created of the binary blood vessel channel, and the ROI of the NPs was added to the distance map (Figure 3.5). As the distance map gives every pixel a value which represents their distance to the closest thresholded blood vessel pixels, the histogram then gives each discrete distance from the blood vessel and how many NPs travelled the respective distances (in pixels). The distance travelled by the NPs in μm was then calculated using the pixel size ($0.6 \mu\text{m}$). The total area in an image containing blood vessels, nuclei, and collagen, was determined by the number of pixels above threshold in the respective channels.

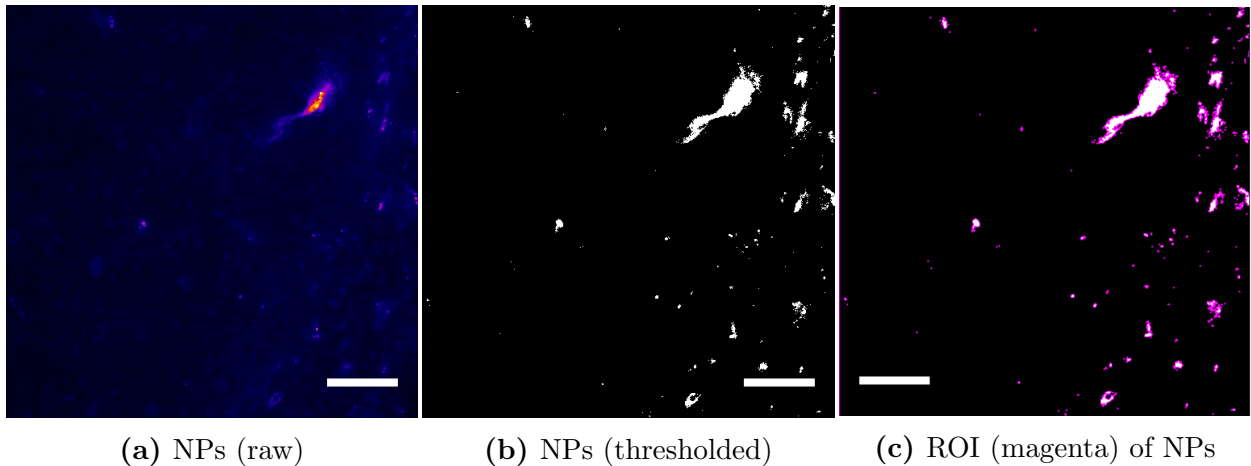
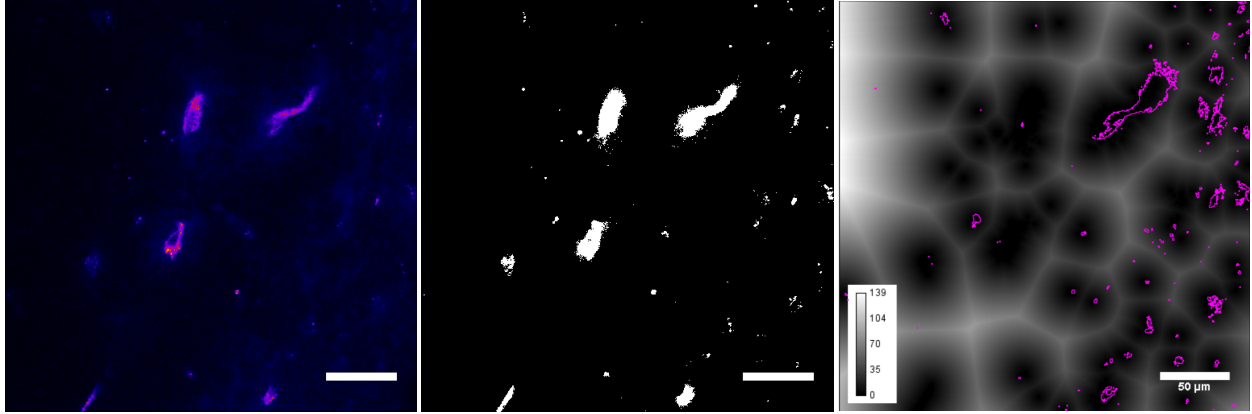


Figure 3.4: Image processing of nanoparticle channel in Fiji. Image a shows the raw image, colored with "Fire" where higher intensities are represented by red, and lower by blue. b shows the same image after being thresholded using Fiji's triangle threshold. In c, an outline (ROI) of the NPs from b is created and stored. Scale bars are $50 \mu\text{m}$.



(a) Raw image BV channel (raw image, fake color 'Fire'.), (b) Thresholded BV channel used to make distance map. (c) ROI of NPs on distance map

Figure 3.5: Image processing of blood vessel channel in Fiji. Image a shows the raw image, b shows the same image after being thresholded using Fiji's triangle threshold. In c, a distance map is created which gives every blood vessel pixel (the white pixels in b) the distance value 0, and every other particle a value corresponding to the distance from the nearest blood vessel pixel. The distances are assigned a greyscale, thus the brightest pixels are furthest from a blood vessel. In the color bar the darkest color represents 0 and the lightest 139 (139 pixels are approximately 83 μm). Scale bars are 50 μm .

3.9 Data analysis

% Extravasation was calculated from thresholded images by:

$$\% \text{ Extravasation} = \frac{\text{Count of pixels outside a blood vessel}}{\text{Total count of pixels in an image}}, \quad (3.1)$$

where the pixels represent thresholded nanoparticles. Mean distance travelled from blood vessels was calculated as:

$$\text{Mean distance} = \frac{\sum(x \times y)}{\sum y}, \quad (3.2)$$

where x is pixels at a distance from the nearest blood vessel and y is counts [#] at the respective distance.

Percent of collagen and blood vessel in an image was calculated from thresholded images as:

$$\text{Amount of X} = \frac{100 \times \text{Total pixel count of X}}{\text{Total pixels in an image}}, \quad (3.3)$$

where X could be either collagen or blood vessels.

The two collagen SHG channels (forward and backward) were added prior to thresholding to ensure that all the collagen was included. For the cleavable images only the backward direction was collected.

3.9.1 Statistics

Due to the low amount of animals (3 per US group for each of the NP types) statistical analysis has not been included in this thesis. While statistical analysis can provide valuable information

about e.g. the success of a treatment, it is far too often used irresponsibly in literature, along with manipulation of results to ensure publication. It is the view of the author that this is unethical research, and that statistical tools should be left to results with appropriate sample sizes and distributions as the tools were meant for. Instead, the data will be presented in a way that hopefully allows the reader to evaluate the effect of the different treatments themselves.

Chapter 4

Results

4.1 Characterization of nanoparticles

All experiments were done with the first batches of NPs. The second batches were used to evaluate reproducibility and to measure the circulation half life time. The animal experiments performed previous to this work were analyzed in this thesis, investigating extravasation and distance travelled into the tumor from frozen tumor sections. For easy visual comparison, the tumor section results from previous work (cleavable NPs) were replotted and added to the appropriate result sections.

4.1.1 Fluorescence intensity measurements

The three lipid NPs (cleavable, non-cleavable and standard) were designed to contain the same amount of fluorophores per NP, and to have a 1:1 ratio of Atto 488 and Atto 700 within each NP. This would ease comparison of complementary fluorescence intensity information by comparing images taken of NPs in the whole animal optical imager (Atto 700) and confocal images of tumor sections (Atto 488), assuming that the detectors were sensitive enough.

To assess whether comparison of fluorescence measurements between the different NPs would be fair, emission spectra were obtained. Two batches of each NP were analyzed to assess reproducibility of NP production with respect to NP content. The first batch was examined twice, over the span of four months to evaluate stability.

Spectra were made for a range of concentrations, from 0.005 mM to 1.0 mM (NPs in PBS). The spectra had similar shapes for all concentrations (seen for the first run of the first batch in Appendix A), and the fluorescence intensity increased linearly with concentration as expected (data not shown). Of these concentrations, 0.5 mM (Figure 4.1) was used for in vitro experiments of cellular uptake, and will be the focus of this section, while 0.3-0.4 mM was the approximate blood concentration during in vivo experiments.

As can be seen in Figure 4.1a the non-cleavable NPs had an approximately 1.5 times higher Atto 488 intensity emission signal compared to both the standard and cleavable NPs. The cleavable and standard NPs had a comparable emission intensity. For Atto 700, the non-cleavable NPs showed an emission signal approximately 1.6 times higher than the cleavable and a little over 5 times higher than the standard NPs (Figure 4.1b).

A new measurement of the first batches was done after 4 months to evaluate whether intensity had been reduced with time. The relationships between NPs showed the same trends

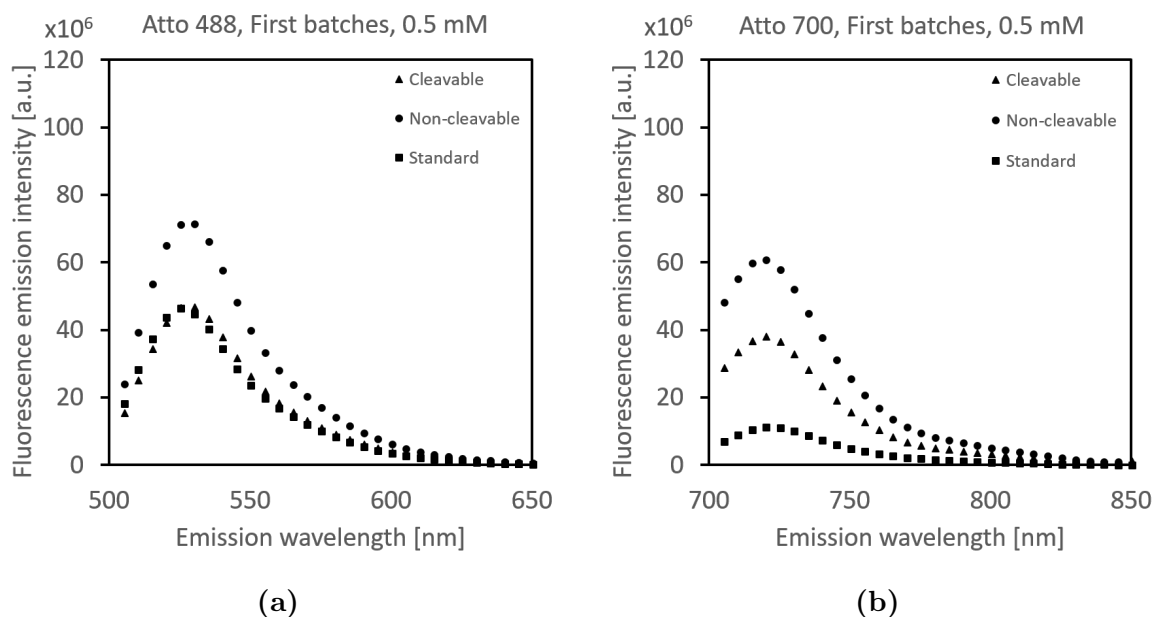


Figure 4.1: Fluorescence emission intensity of Atto 488 and Atto 700 in the three different NPs. The same symbols are used for the same NPs. a) Atto 488 was excited at 480 nm, and emission was detected from 505 nm to 655 nm. b) Atto 700 was excited at 680 nm and emission was detected between 705 nm and 850. Concentration of NPs was 0.5 mM in PBS. 3 replikates for each measurement.

(Figure 4.2), with the intensity of all samples slightly reduced, except Atto 488 in the standard NP, which showed a small increase.

New batches of all NPs were investigated to evaluate the reproducibility of the NP production. Interestingly, the NP with the highest Atto 488 emission intensity of the new batches was the cleavable, followed by the non-cleavable and the standard NPs. The Atto 488 spectra of the second batch of non-cleavable NPs was somewhere in-between the two time points of the first batch. The second batch of the standard NP showed a lower Atto 488 intensity, but a higher Atto 700 intensity compared to the first batch (Figure 4.3).

Regarding the Atto 700 spectra, the second batch of the non-cleavable NPs again showed the highest fluorescence intensity, followed by the cleavable and the standard NPs. Here, both non-cleavable and standard NPs had a higher Atto 700 than Atto 488 emission intensity (Figure 4.3).

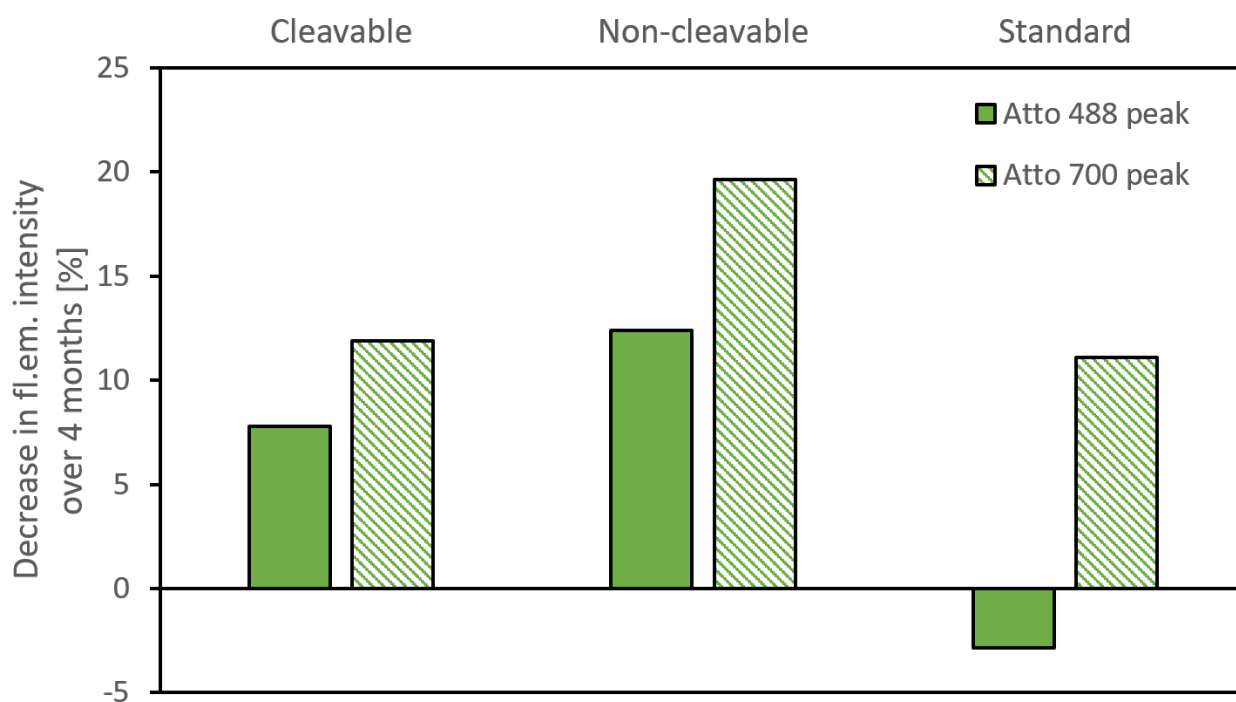


Figure 4.2: Decrease in fluorescence emission intensity over 4 months. 3 replicates for each measurement.

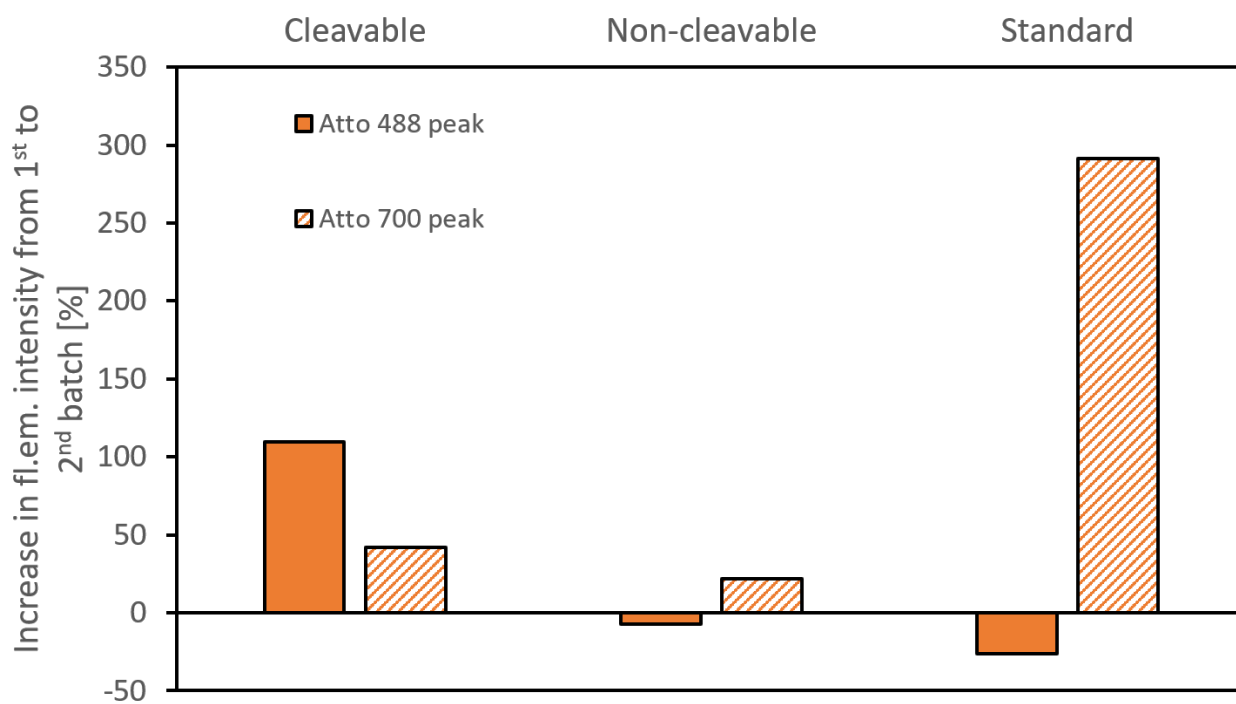


Figure 4.3: Increase in fluorescence emission intensity from first to second batch. 3 replicates for each measurement.

4.1.2 Characterization of nanoparticle properties

As mentioned above, the nanoparticles used here are provided by Ph.D.-candidate V. Sereti at DTU, in Denmark, as a part of a collaborative project. With each batch, V. Sereti has kindly included measured properties of the NPs, including average size, poly dispersity index (PDI), zeta-potential, and the concentration of each vial (see Table 4.1 and 4.2). It should be noted for the first batches, that the size of the standard NP is approximately 20-25 % smaller than the non-cleavable and cleavable NPs. The surface charge of the NPs varies from approximately -3 mV for the non-cleavable, to -8 mV for the cleavable and -13 mV for the standard NP (Table 4.1).

It can be seen that while the size of the cleavable and standard NPs are quite similar between batches, the second batch of non-cleavable NPs have an average size which is 25 % smaller than the first non-cleavable batch. For the cleavable NPs, the ζ -potential were more negative in the second batch, the standard NPs had a more neutral ζ -potential than the first batch, while the non-cleavable NPs had the same surface charge (Table 4.2) For all NPs the second batches had a smaller concentration than their respective first batches.

M. Olsman tested blood circulation half-life for the second batches of NPs and found that all three NPs had a comparable circulation time, from 3.4 hours (standard), to 3.8 h hours (cleavable) and 4 hours (non-cleavable) (Table 4.2).

Table 4.1: Characteristics of the first batches of the three lipid NPs as provided by V. Sereti at DTU.

	Cleavable	Non-cleavable	Standard
Size [nm]	168.0 ± 3.1	155.4 ± 1.234	126.0 ± 0.8
PDI	0.05 ± 0.032	0.102 ± 0.02	0.035 ± 0.007
ζ -potential [mV]	-8.14 ± 1.35	-2.73 ± 0.25	-13.4 ± 0.45
Concentration stock [mM]	19.9	21.8	19.7

Table 4.2: Characteristics of the second batches of the three lipid NPs as provided by V. Sereti at DTU, as well as half life circulation time data provided by M. Olsman (personal communication).

	Cleavable	Non-cleavable	Standard
Size [nm]	154.7 ± 3.8	115.9 ± 0.95	108.0 ± 0.9
PDI	0.065 ± 0.015	0.083 ± 0	0.028 ± 0.011
ζ -potential [mV]	-15.7 ± 0.2	-3.16 ± 0.45	-10.9 ± 0.7
Concentration stock [mM]	13.03	16.08	16.16
Half life time in blood [h]	~ 3.8	~ 4	~ 3.4

4.1.3 Aggregation behaviour in blood and serum

When nanoparticles are injected intravenously, the first barrier the nanoparticles encounter is the blood, where they can interact with everything from proteins to immune cells. To reach the tumor, the drug delivery carriers must not be opsonized and cleared from circulation. Further, when the NPs need to escape the blood, cross the epithelial wall of the blood vessels

(second barrier), and enter the tumor tissue, large sized aggregates will probably not be able to extravasate. Therefore, it was decided to evaluate the three NPs behaviour in whole blood and in serum. The stock solutions of NPs were kept in HEPES buffer saline, so NPs in HEPES (0.5 mM), HEPES and serum, and HEPES and blood were imaged (Figure 4.4). When the NPs were injected in mice during the in vivo experiments previous to this project, they were first diluted to desired concentration (6 mM for in vivo experiments) in PBS. Hence, the NPs were also diluted in PBS (0.5 mM, here) to evaluate whether the salts in PBS affected the aggregation of NPs (Figure 4.5). The NP in buffer (0.5 mM) were mixed in a 2:1 ratio with both whole blood and serum.

From the images in Figures 4.4 and 4.5 it would appear that the standard nanoparticle has the largest aggregates both in HEPES buffer and PBS. The difference between cleavable and non-cleavable NPs is less clear, but there seems to be a brighter background (more 1 and 2 pixel sized particles) in the cleavable and more middle sized non-cleavable particles in PBS and serum.

To quantify the differences of the three NPs, particle sizes were counted and distributions were plotted (Figures 4.7 and 4.8). The histograms show a distribution of particles imaged in each sample (N=1), where the size or area of a particle is given as a number of pixels clustered together and not e.g. a diameter, due to the different shapes seen in Figures 4.4 and 4.5. As the pixel size (200 nm) was smaller than the resolution of the microscope (excitation wavelength was 501 nm), μm^2 was not used to avoid confusion of how accurate the measurements were. Size was instead measured as number of connected pixels.

It was found that the cleavable NPs didn't form any aggregates with an area larger than 200 pixels. The non-cleavable NPs did not form aggregates larger than 100 pixels. The standard NPs formed larger aggregates compared to the other two NPs (Figures 4.7 and 4.8). The shapes of the larger aggregates of the standard NPs were more elongated, compared to round aggregates seen in the other two groups. The aggregates were found in both HEPES buffer saline and PBS, as well as when NPs in buffer were mixed with serum and whole blood (Figures 4.4 and 4.5). It is worth noting that the percentage of large aggregates is increased for images with a low "background", or few small aggregates in focus. Aggregates below 5 connected pixels were not included in the plots of size distribution.

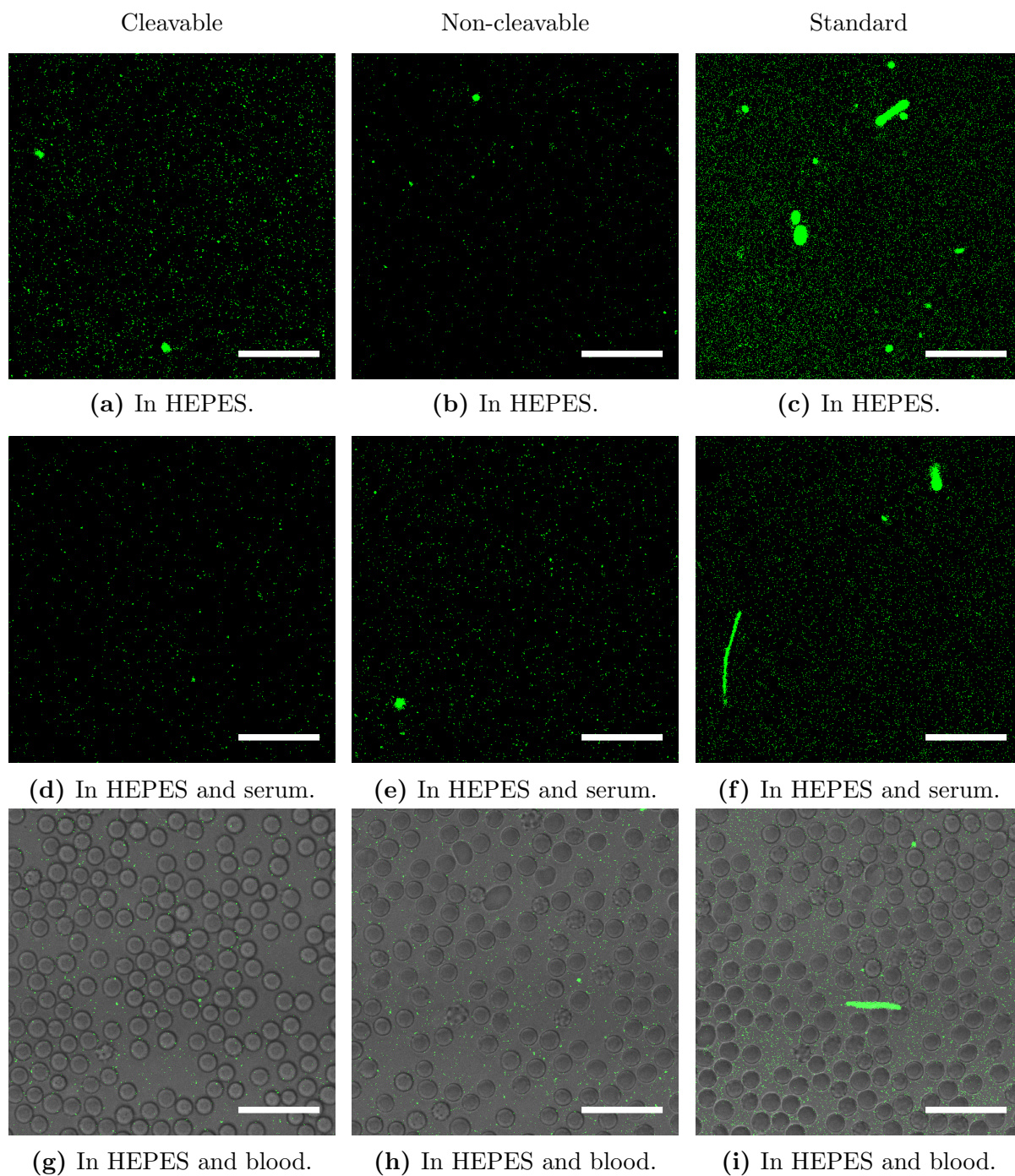


Figure 4.4: Confocal images of NPs in HEPES only (top row), HEPES and serum (middle row), and HEPES and whole blood (bottom row). Representative images were picked from 30 s videos. Particle channel is thresholded using "RenyiEntropy" automatic thresholding in Fiji. All scalebars are 25 μm .

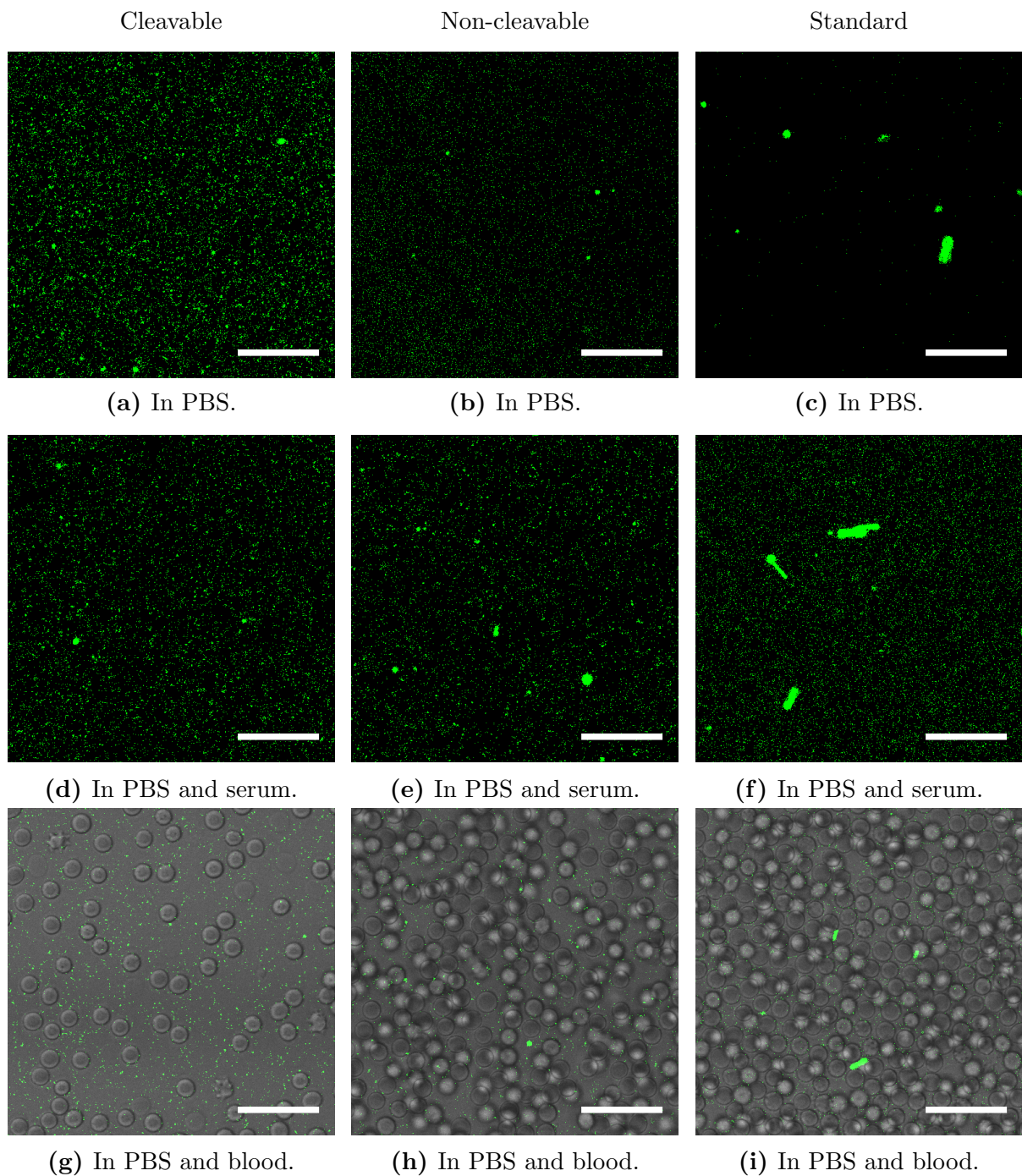


Figure 4.5: Confocal images of NPs in PBS only (top row), PBS and serum (middle row), and PBS and whole blood (bottom row). Representative images were picked from 30 s videos. Particle channel is thresholded using "RenyiEntropy" automatic thresholding in Fiji. All scalebars are 25 μm .

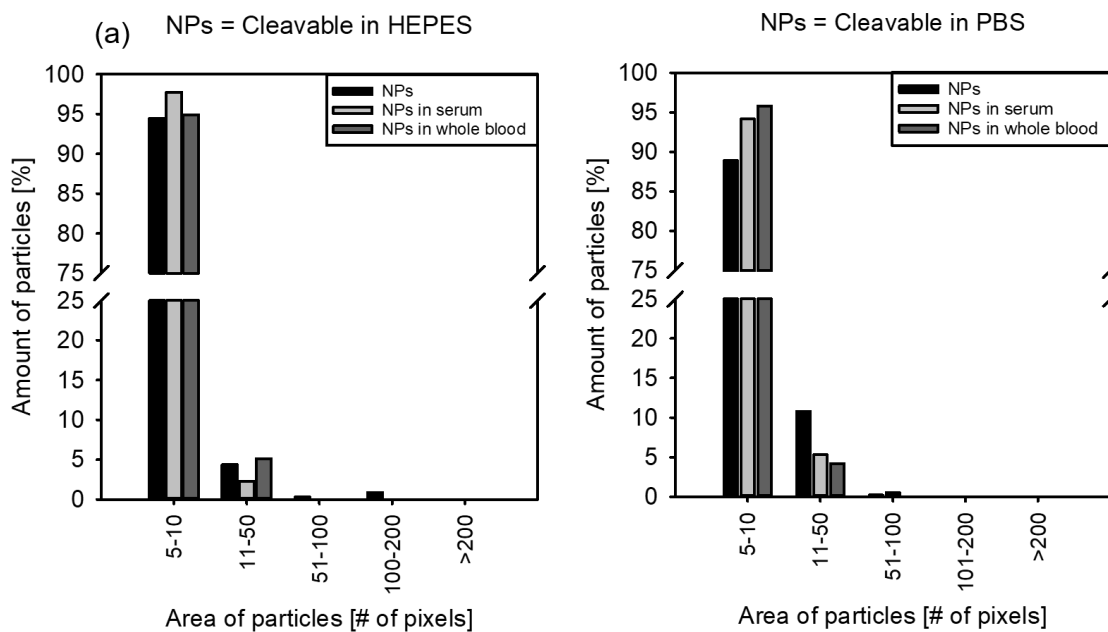


Figure 4.6: Histograms showing percentage of cleavable NPs in HEPES (left) and PBS (right). Note difference in bin range. Y-axis break from 25 to 70 % for all graphs. Calculated from three representative images from each video.

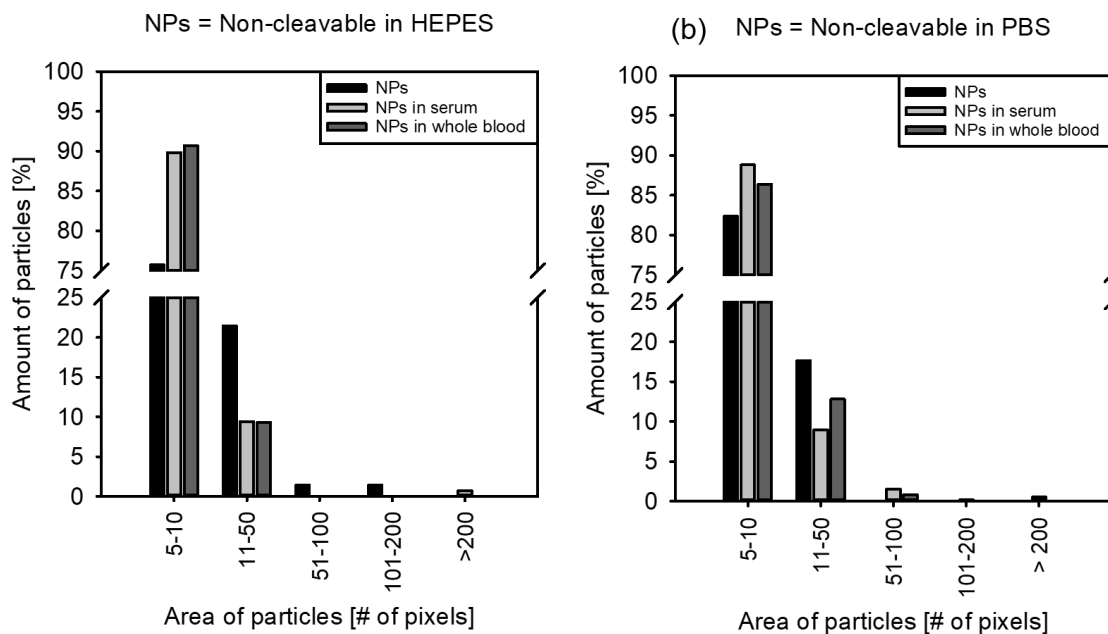


Figure 4.7: Histograms showing percentage of non-cleavable NPs in HEPES (left) and PBS (right). Note difference in bin range. Y-axis break from 25 to 70 % for all graphs. Calculated from three representative images from each video.

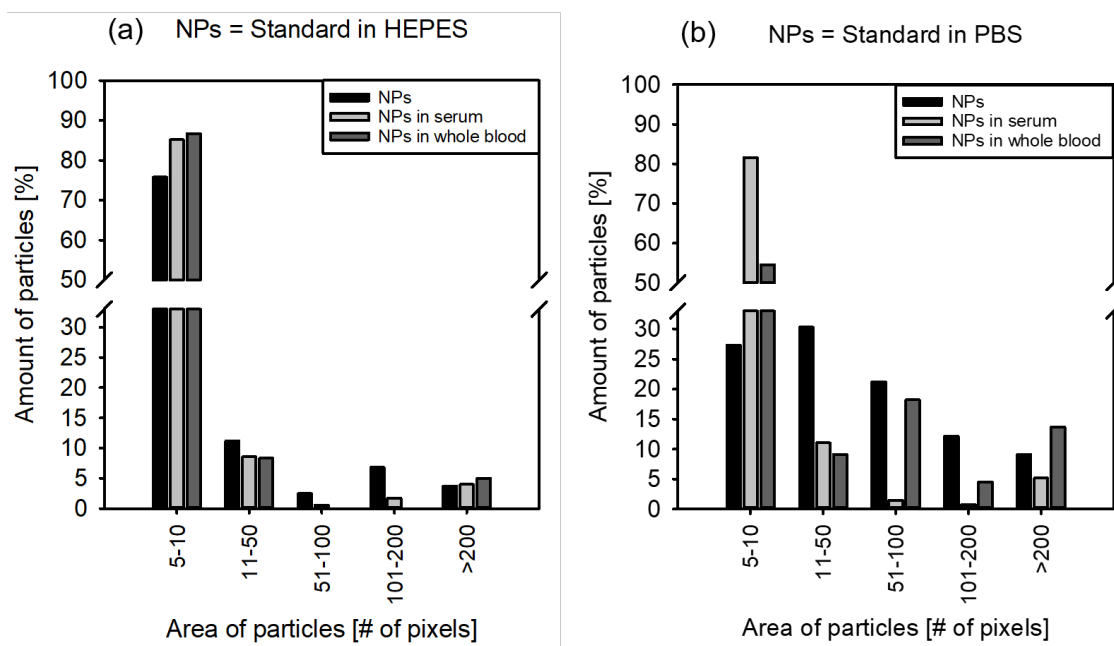


Figure 4.8: Histograms showing percentage of standard NPs in HEPES (left) and PBS (right). Y-axis break from 33-50. Note difference in bin range. Calculated from three representative images from each video.

4.2 Extravasation and distribution of nanoparticles

4.2.1 Extravasation of NPs from blood vessels

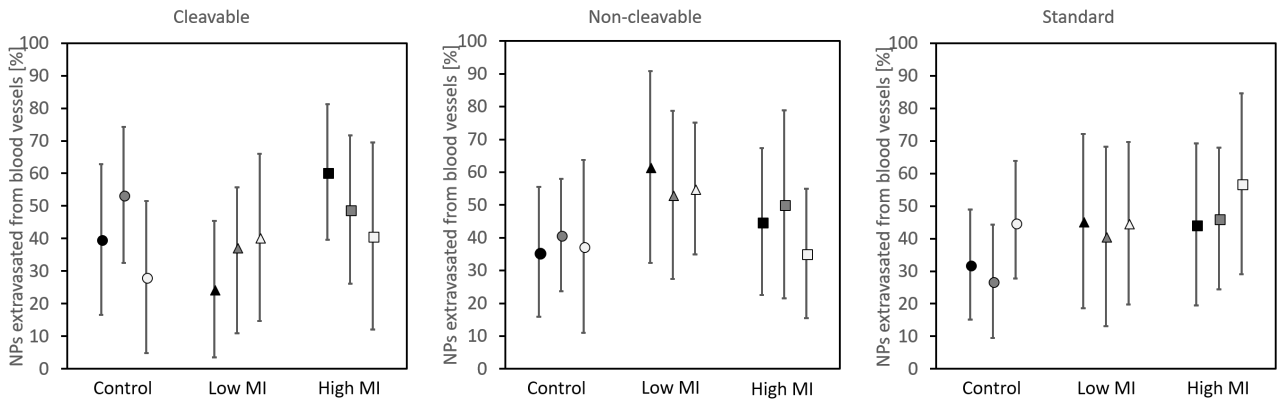
To be able to reach any cancer cells, the nanoparticles had to overcome the second barrier: extravasation, i.e. move out of the blood vessel and into tumor ECM. To increase extravasation, two animal groups were exposed to ultrasound (low and high MI), while the control group did not receive ultrasound. The ultrasound was expected to cause stress on the blood vessel wall indirectly, by making injected microbubbles (Sonovue™) oscillate. In Figure 4.9, the percent extravasation seen in individual images are plotted, grouped according to ultrasound exposure (or lack thereof). The extravasation of the cleavable NPs are replotted from unpublished project work done last semester, to be able to easily compare the three NPs. Then, only two mice were part of the control group, and here a third control mouse has been added to the calculations. When calculating extravasation (Figure 4.9b), intensity was not included, only pixels above threshold.

As can be seen in Figure 4.9, the mean extravasation varies for all NPs. For the cleavable NPs the high MI group showed higher uptake compared to the low MI group, while the control group (no US) were between the US groups. It is the "middle" control animal (animal 19) that has been added this semester.

For the non-cleavable NPs, the low MI group had a higher mean intensity than the high MI group. In animal optical images of the tumor, the same trend was seen, but it was found to be insignificant after correcting for fluorescent intensity differences (personal communications). It should be noted that no image in the low MI non-cleavable NP group had less than 10 % extravasation (Figure 4.9b).

Mean extravasation for animals receiving the standard NPs showed less difference compared to the other NPs (Figure 4.9c). Two of the control animals show a lower mean extravasation compared to the groups exposed to ultrasound, while one animal in the high MI group had a higher mean uptake than all the other animals.

A box plot where images from all 3 animals in each group are plotted together, and a scatter plot of the extravasation in each image of each animal are shown in Appendix B. These plots shows the median extravasation of each group, as well as some differences within animals.



(a) Mean extravasation \pm SD of cleavable NPs (data from fall project).

(b) Mean extravasation \pm SD of non-cleavable NPs.

(c) Mean extravasation \pm SD of extravasation of standard NPs.

Figure 4.9: Extravasation of NPs in individual images calculated as % NPs outside a blood vessel divided by the total amount of pixels representing NPs in that image. Each dot represents one animal. Mean \pm SD extravasation for each animal is shown. 3 Animals per group (control=no US). Approximately 30 images per animal, collected from 3 tumor sections per animal. Left to right markers correspond with increasing numbering of animals in subsequent plots through the thesis.

4.3 Penetration into tumor tissue

The third barrier the NPs must overcome is travelling through the tumor ECM to be able to reach all cancer cells. The distance from the blood vessels of the NPs who had extravasated was measured and plotted for each of the cleavable, non-cleavable and standard to see if any of them travelled further from the blood vessels. To assess whether US affected penetration depth, the results were grouped according to US exposure (Figure 4.10).

It would appear from Figure 4.10, that it is the particles who were exposed to US who dominates after 10 μm . In the case of the cleavable NPs (Figure 4.10c), it is of the particles exposed to high MI US who dominate the distances above 5 μm , while low MI is slightly lower than the cleavable NPs who didn't experience US. The high MI group of the standard NPs also travels further than the low MI and control groups, but here the standard NPs exposed to low MI US travels further from blood vessels than the control particles (Figure 4.10a). However, for the non-cleavable NPs, it is the NPs exposed to low MI US who travel the furthest, followed by the high MI group (Figure 4.10b).

As the groups where the particles travelled furthest seems to be the same groups with the highest extravasation in Figure 4.9, a scatter plot was made of the distance travelled versus the % extravasated for the particles in each image.

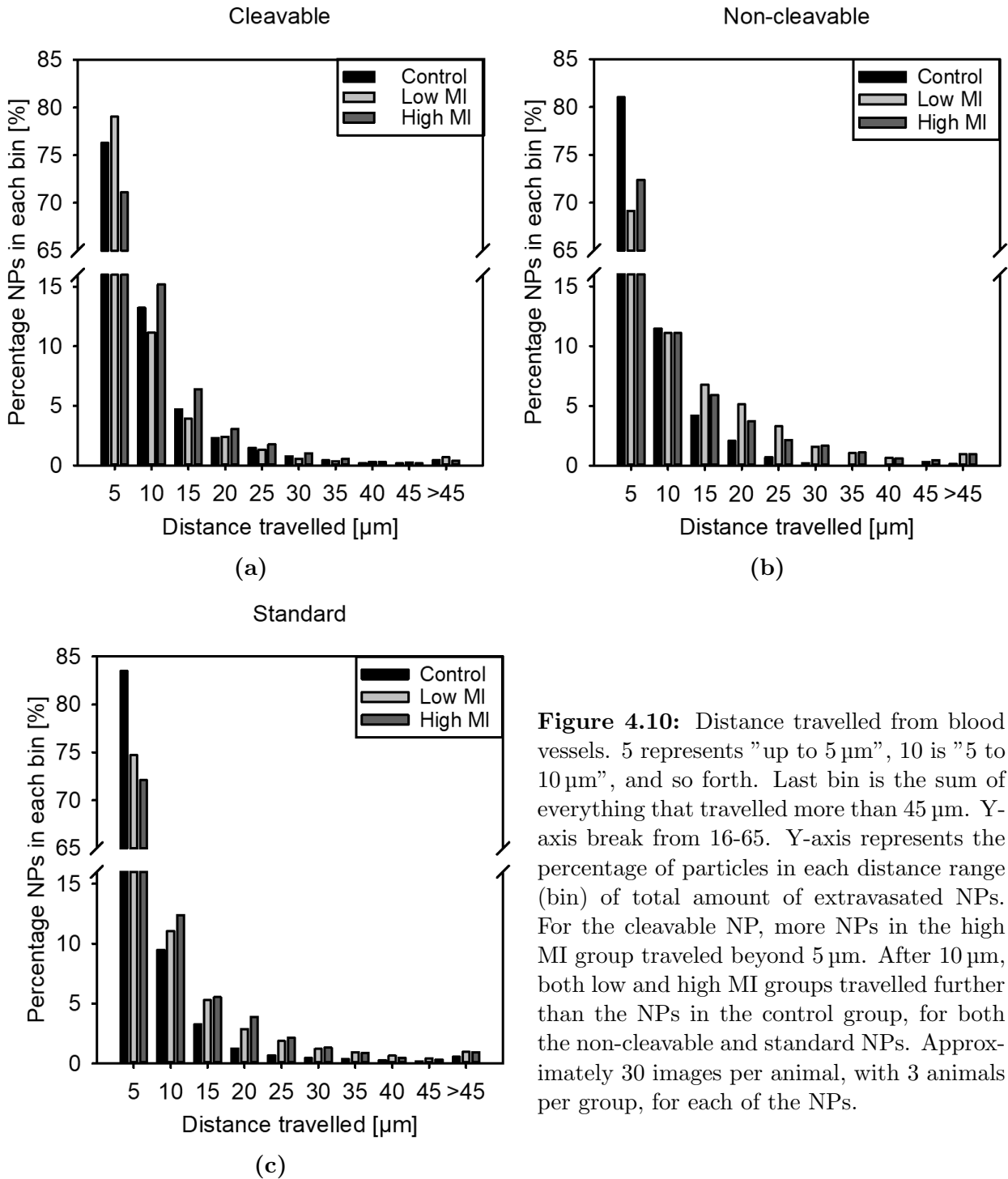


Figure 4.10: Distance travelled from blood vessels. 5 represents "up to 5 μm ", 10 is "5 to 10 μm ", and so forth. Last bin is the sum of everything that travelled more than 45 μm . Y-axis break from 16-65. Y-axis represents the percentage of particles in each distance range (bin) of total amount of extravasated NPs. For the cleavable NP, more NPs in the high MI group traveled beyond 5 μm . After 10 μm , both low and high MI groups travelled further than the NPs in the control group, for both the non-cleavable and standard NPs. Approximately 30 images per animal, with 3 animals per group, for each of the NPs.

4.3.1 Distance travelled vs percent extravasated

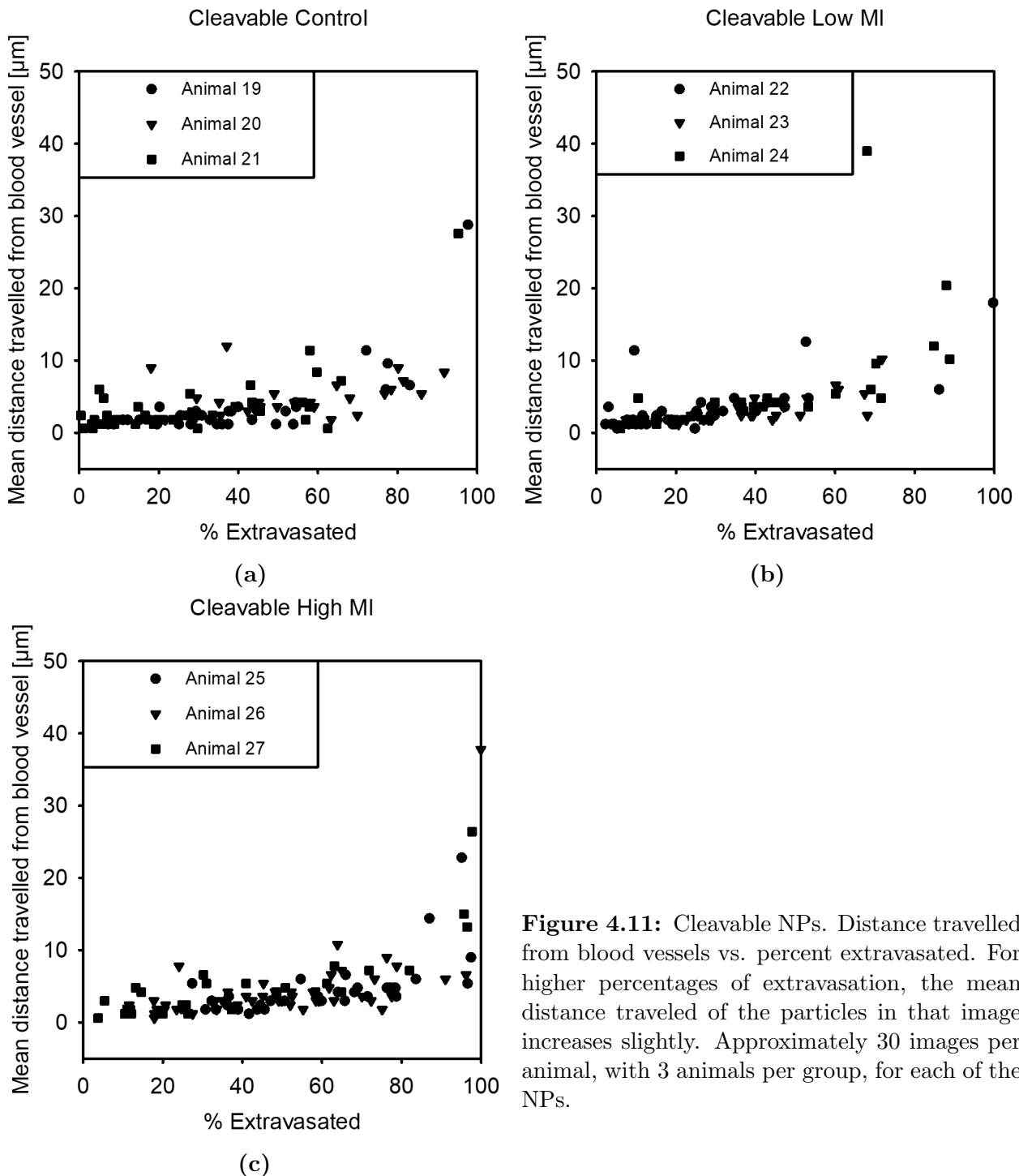


Figure 4.11: Cleavable NPs. Distance travelled from blood vessels vs. percent extravasated. For higher percentages of extravasation, the mean distance traveled of the particles in that image increases slightly. Approximately 30 images per animal, with 3 animals per group, for each of the NPs.

In Figure 4.11, the relationship between mean distance travelled and percent extravasation is presented for the cleavable NPs. This was done to evaluate the degree of dependence on mean distance travelled of the particles in an image on how many particles extravasated. As can be seen, there seem to be a weak increase in mean distance travelled with a higher percent extravasation. The same is true for non-cleavable and standard NPs (Figures 4.12 and 4.13).

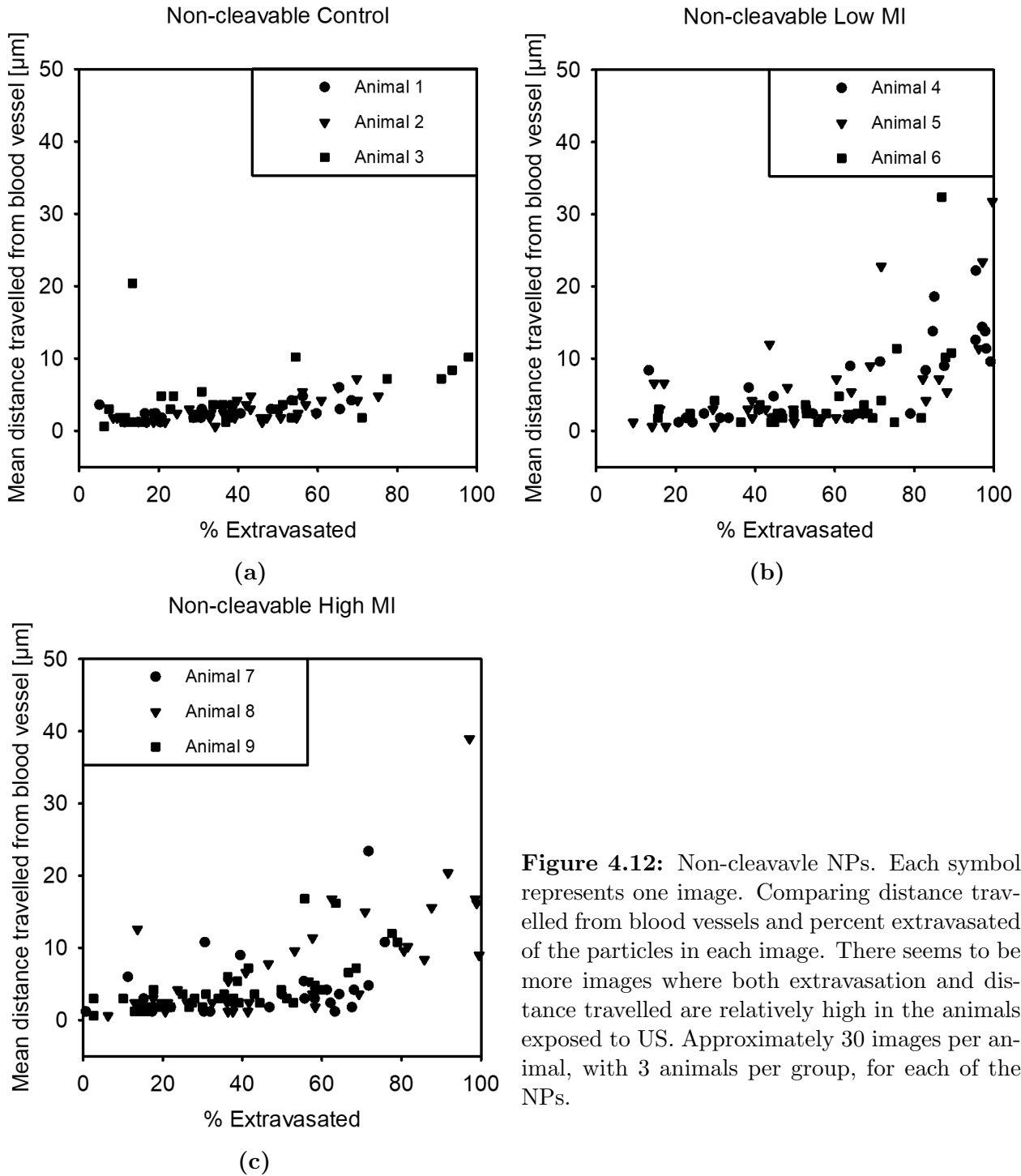


Figure 4.12: Non-cleavable NPs. Each symbol represents one image. Comparing distance travelled from blood vessels and percent extravasated of the particles in each image. There seems to be more images where both extravasation and distance travelled are relatively high in the animals exposed to US. Approximately 30 images per animal, with 3 animals per group, for each of the NPs.

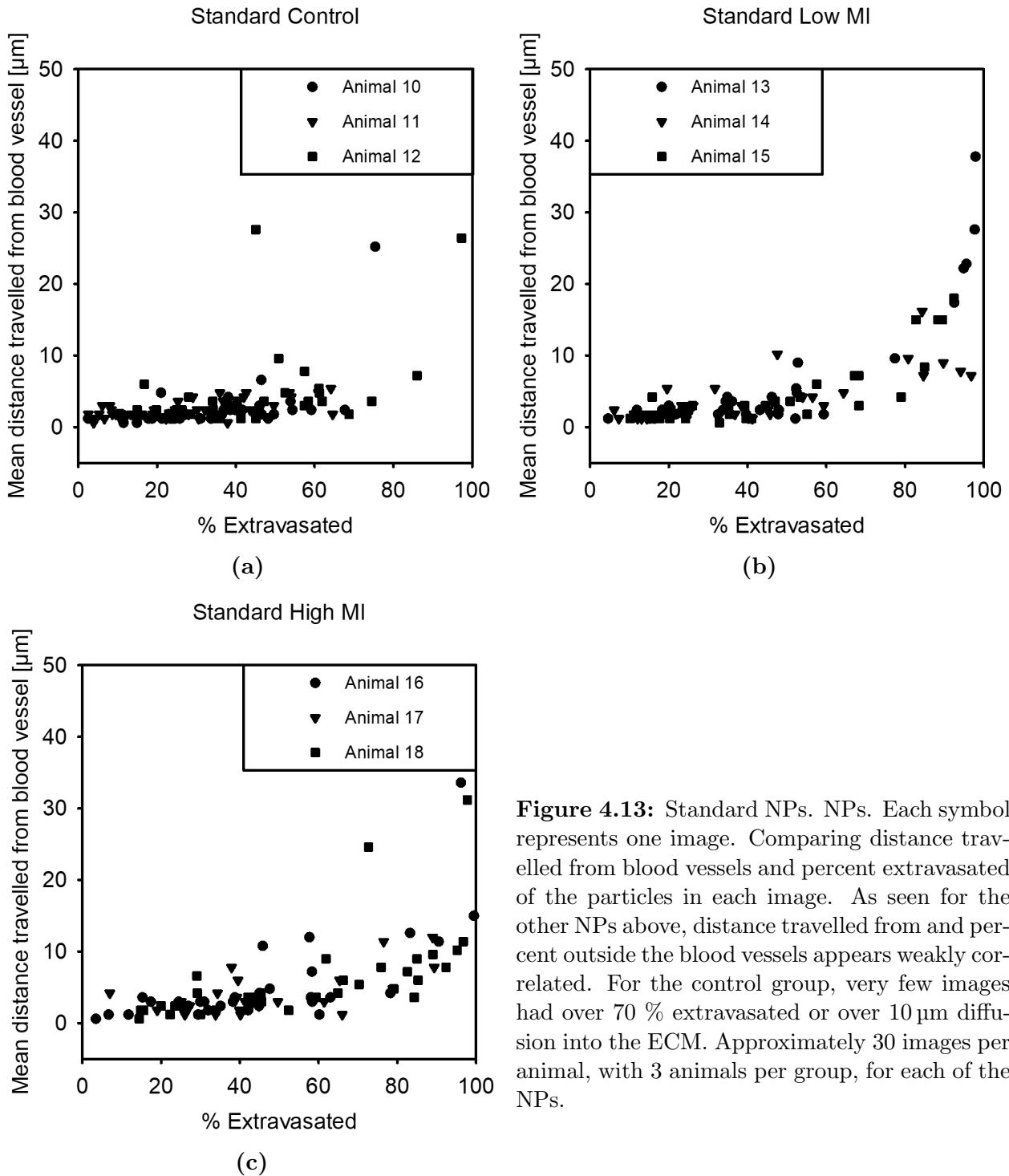


Figure 4.13: Standard NPs. NPs. Each symbol represents one image. Comparing distance travelled from blood vessels and percent extravasated of the particles in each image. As seen for the other NPs above, distance travelled from and percent outside the blood vessels appears weakly correlated. For the control group, very few images had over 70 % extravasated or over 10 μm diffusion into the ECM. Approximately 30 images per animal, with 3 animals per group, for each of the NPs.

4.3.2 Effect of blood vessel content on penetration

According to literature, larger blood vessels in tumors tend to be less structurally organized and therefore more leaky compared to smaller vessels. Therefore, the amount of the vessel (calculated here as the total area of blood vessels in an image) was compared to % extravasation and mean distance travelled for the NPs in that image.

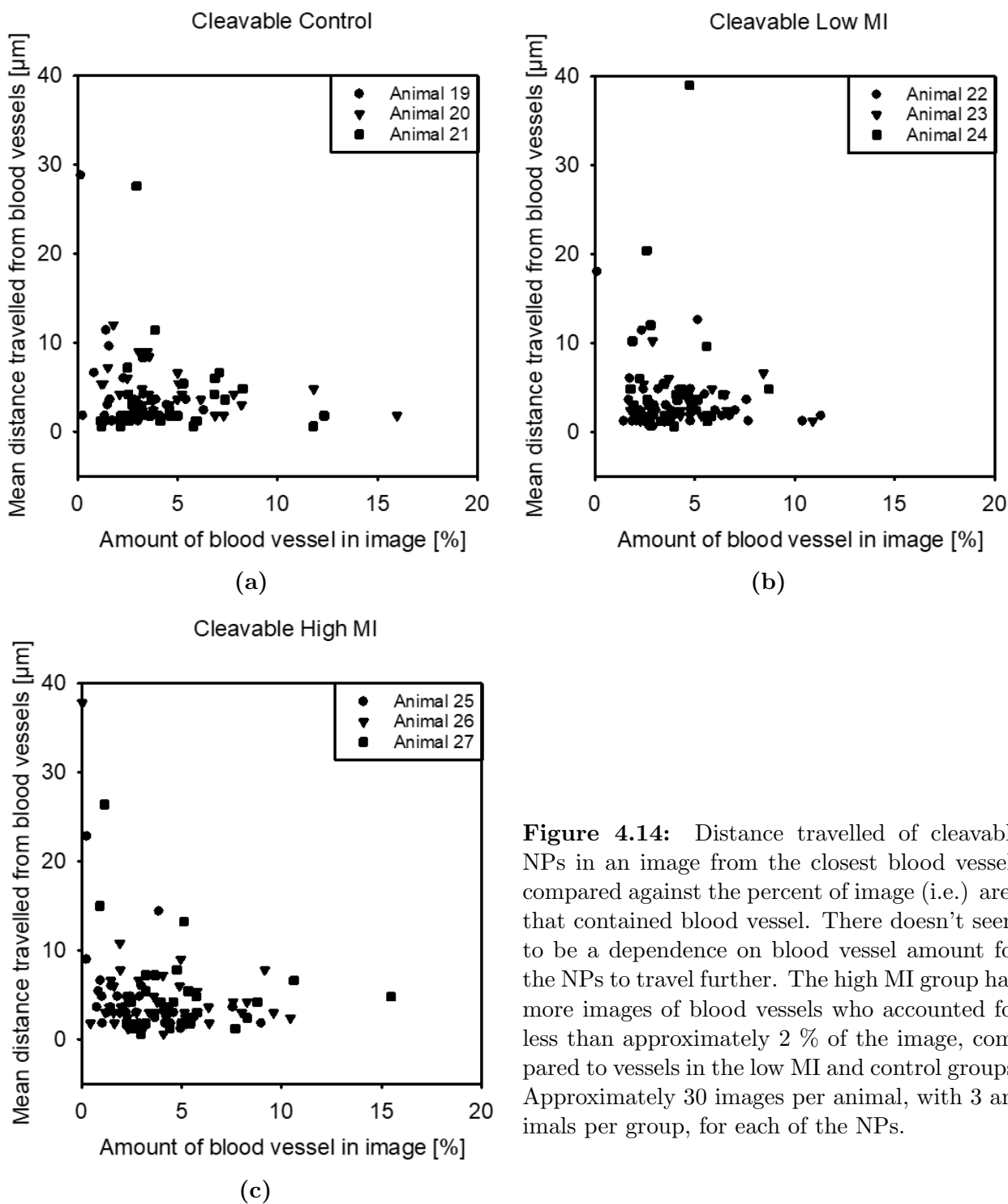


Figure 4.14: Distance travelled of cleavable NPs in an image from the closest blood vessels compared against the percent of image (i.e.) area that contained blood vessel. There doesn't seem to be a dependence on blood vessel amount for the NPs to travel further. The high MI group had more images of blood vessels who accounted for less than approximately 2 % of the image, compared to vessels in the low MI and control groups. Approximately 30 images per animal, with 3 animals per group, for each of the NPs.

It should be noted that these calculations are independent of number of blood vessels,

and therefore many small vessels might have the same area as one large. However, images with multiple small vessels were not imaged nearly as frequent as longer, larger single vessels. Further, if a (larger) blood vessel which had some extravasated NPs associated with it, was poorly stained, it's image is likely to be represented by a low blood vessel area and a high extravasation/mean distance travelled.

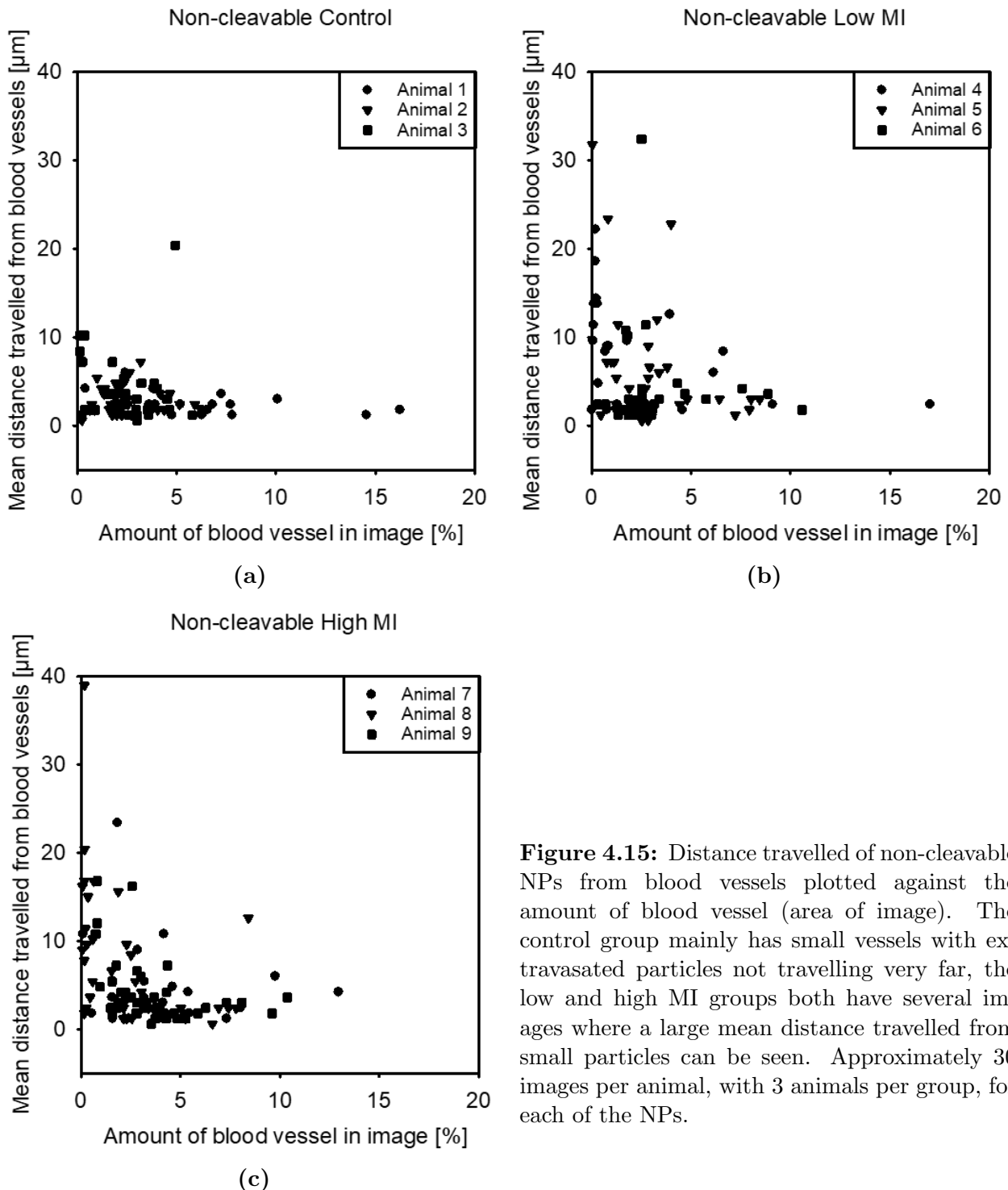


Figure 4.15: Distance travelled of non-cleavable NPs from blood vessels plotted against the amount of blood vessel (area of image). The control group mainly has small vessels with extravasated particles not travelling very far, the low and high MI groups both have several images where a large mean distance travelled from small particles can be seen. Approximately 30 images per animal, with 3 animals per group, for each of the NPs.

No dependence was found between the area blood vessel and fraction of extravasated NPs in an image (data not shown). For the mean distance travelled of NPs in an image versus the

amount of blood vessel (area fraction of image) is shown in Figures 4.11, 4.12, and 4.13. One thing that could not be controlled for when acquiring 2D images of heterogeneous 3D tumors was how the blood vessel was cut with respect to its cross-section and long axis. The only way to see the diameter of a vessel is to cut either perpendicular to its long axis, or perpendicular to the cross-section where the vessel is widest.

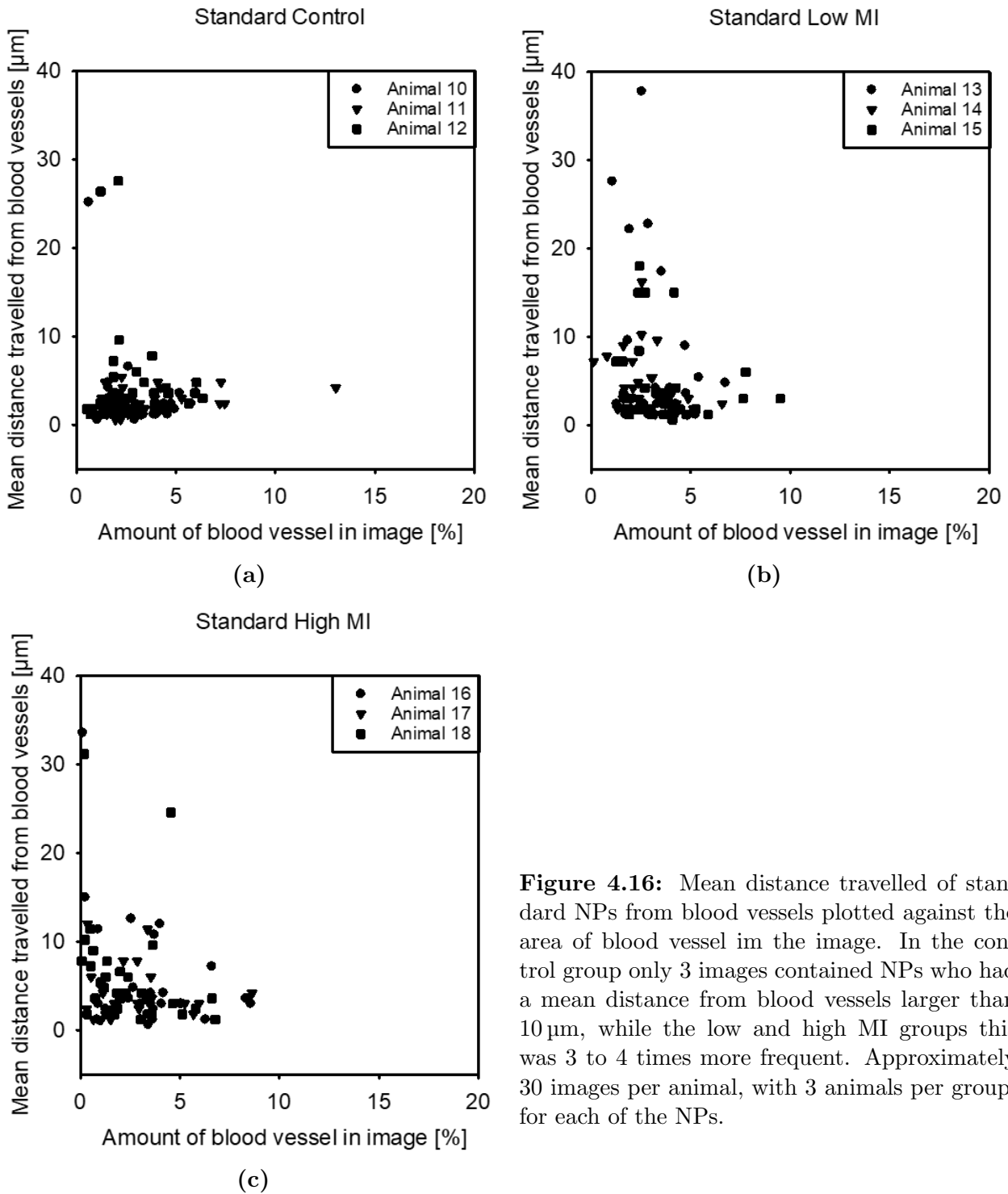


Figure 4.16: Mean distance travelled of standard NPs from blood vessels plotted against the area of blood vessel in the image. In the control group only 3 images contained NPs who had a mean distance from blood vessels larger than 10 μm , while the low and high MI groups this was 3 to 4 times more frequent. Approximately 30 images per animal, with 3 animals per group, for each of the NPs.

It can be seen in Figures 4.14, 4.15, and 4.16, that most images contain blood vessels where NPs didn't penetrate too far into the tumor tissue (less than 5 μm). There is no trend

where the images containing the largest total blood vessel area also contain NPs that travelled very far into the ECM. Rather, the largest mean distance travelled tend to have extravasated from smaller (or poorly stained) blood vessels. The latter also seems to be more frequent in ultrasound groups than in the control groups, at least for the non-cleavable and standard NPs.

4.3.3 Effect of collagen content on penetration

To travel far into the ECM, the NPs must travel through the ECM "scaffold", made up of proteins and proteoglycans in a mesh-like structure. To be able to do this, particles must not be larger than the "mesh holes" e.g. the NPs must fit between the many structural components. Further, the particles must not stick to the components, e.g. due to surface interactions. Since collagen is the most abundant protein in the body, and makes up a large fraction of ECM, collagen content was used as a measurement of protein density in the ECM. Amount of collagen was then compared to % extravasation of NPs and their mean distance travelled from blood vessels. No clear trend was seen between collagen content and extravasation (data not shown). The amount of collagen and the mean distance travelled by NPs in an image is plotted in Figures 4.17, 4.18 and 4.19, for cleavable, non-cleavable, and standard NPs respectively.

It should be noted that for the cleavable NPs, imaged last semester, only the reflected SHG signal was collected, while for non-cleavable and standard NPs both transmitted and reflected SHG signal was collected and analyzed. This is most likely the reason that Figure 4.17 seems to have less collagen overall compared to Figures 4.18 and 4.19.

No clear relationship between the amount of collagen and the distance travelled was seen. In the cleavable and non-cleavable control group, the NPs who travelled furthest seemed to have less collagen in their vicinity, while for the standard control group the NPs travelling furthest did so independently of collagen content.

For low and high MI groups there was a higher distance travelled in the images with higher collagen content compared to the control groups, especially for the non-cleavable and standard NPs. For the cleavable NPs this is not as clear.

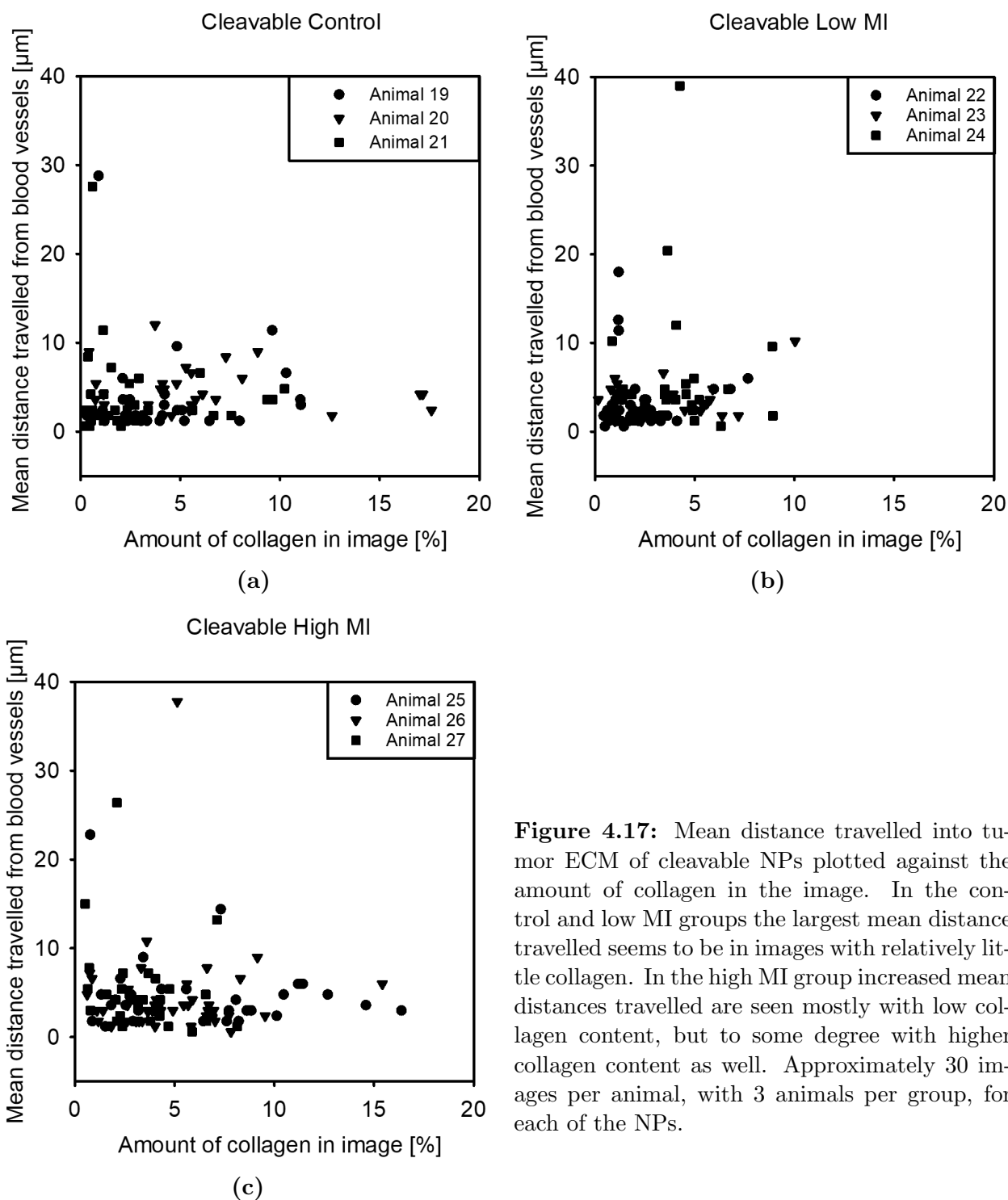


Figure 4.17: Mean distance travelled into tumor ECM of cleavable NPs plotted against the amount of collagen in the image. In the control and low MI groups the largest mean distance travelled seems to be in images with relatively little collagen. In the high MI group increased mean distances travelled are seen mostly with low collagen content, but to some degree with higher collagen content as well. Approximately 30 images per animal, with 3 animals per group, for each of the NPs.

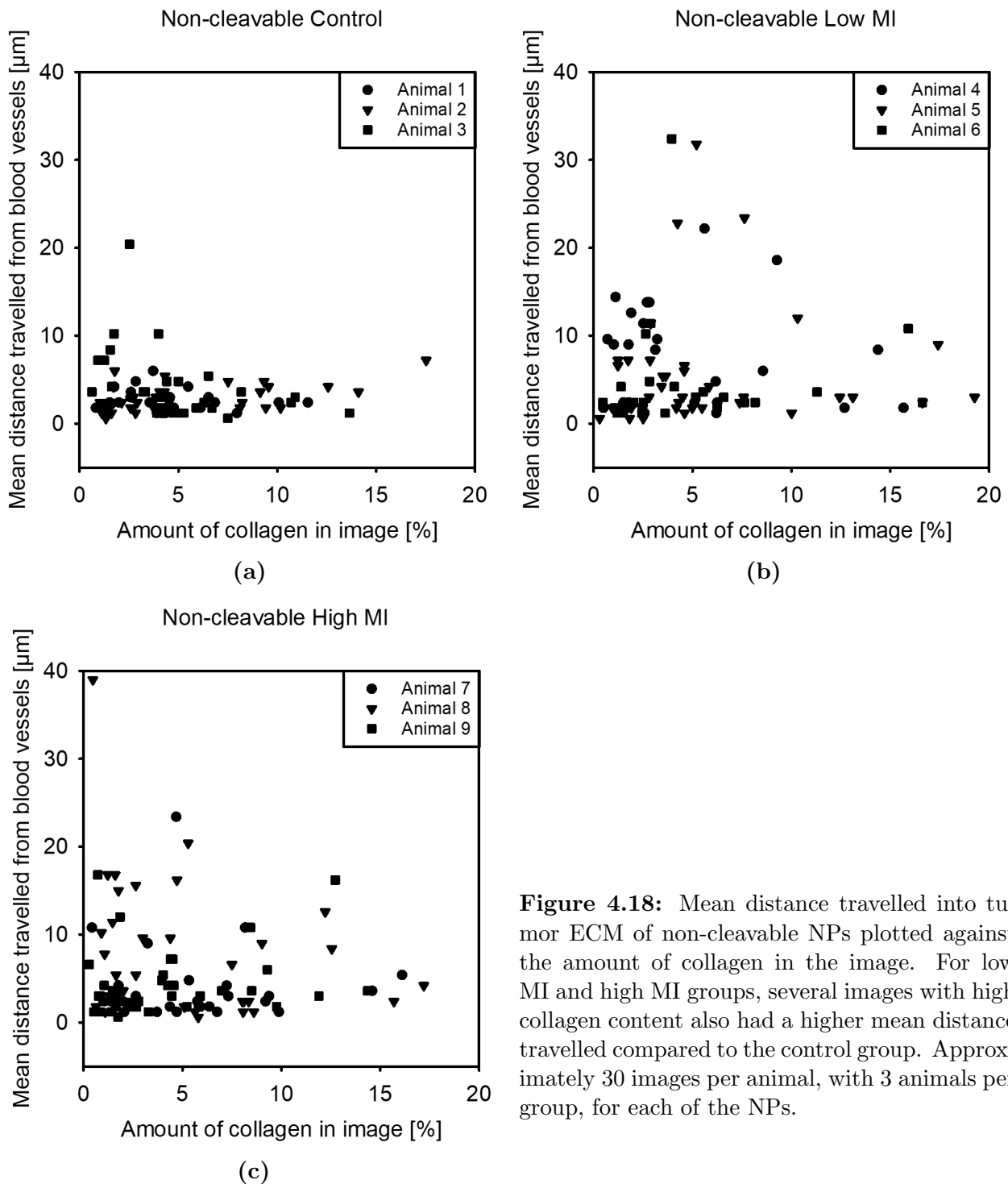
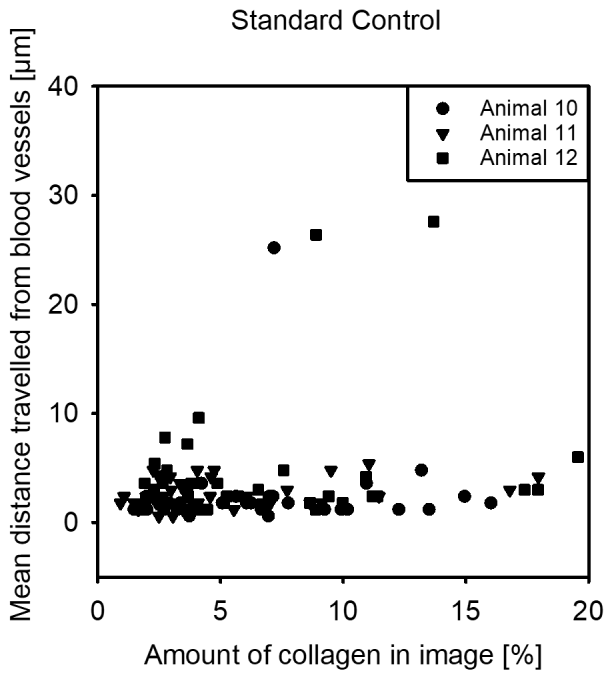
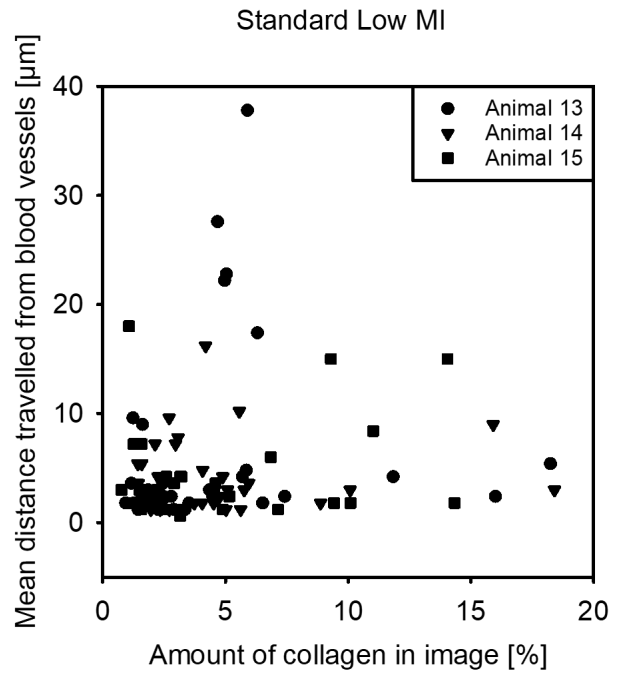


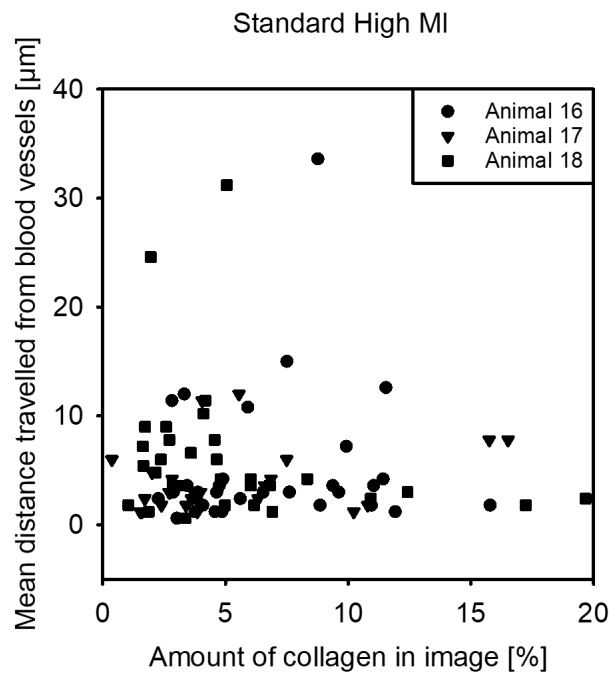
Figure 4.18: Mean distance travelled into tumor ECM of non-cleavable NPs plotted against the amount of collagen in the image. For low MI and high MI groups, several images with high collagen content also had a higher mean distance travelled compared to the control group. Approximately 30 images per animal, with 3 animals per group, for each of the NPs.



(a)



(b)

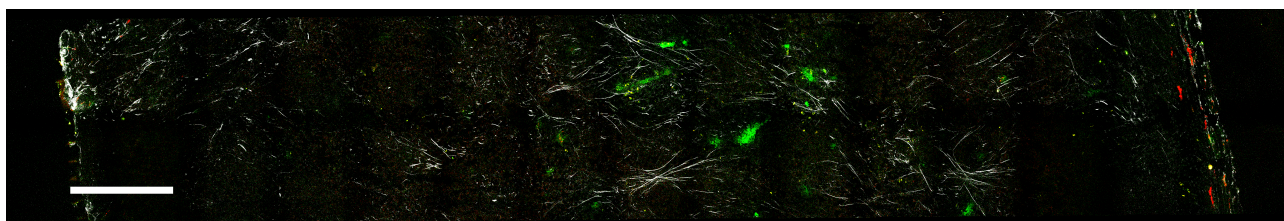


(c)

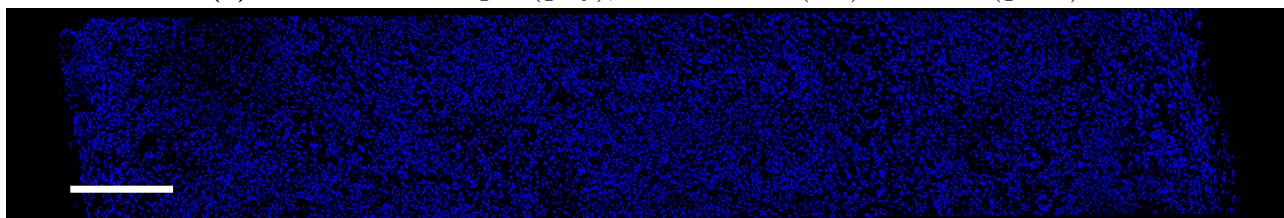
Figure 4.19: Mean distance travelled into tumor ECM of standard NPs plotted against the amount of collagen in the image. Some increase in higher mean distance travelled, independent of collagen content in the low and high MI groups. Approximately 30 images per animal, with 3 animals per group, for each of the NPs.

4.4 Histology of tumors: distribution of collagen and blood vessels

Tile scans were made of one section from two animals. The tumor sections were imaged from one edge, through the center and to the opposite edge, to evaluate whether blood vessels and collagen were located mainly in the periphery or throughout the tumor (Figures 4.20 and 4.21). Interestingly, collagen was seen throughout the section in both animals. Larger blood vessels were seen primarily in the peripheral areas, yet nanoparticle signal in the center indicates that the blood vessels were present throughout as well. This is consistent with what was observed during microscopy of tumor sections searching for blood vessels and NPs. The image channel capturing the nuclei (Figures 4.20b and 4.21b respectively) are presented below the collagen, blood vessel and nuclei. A high cell density common to tumors is observed. Nuclei density was calculated for images of the animals receiving non-cleavable and standard NPs, and very little variation was observed (Appendix D). In Figure 4.21, a structure assumed to be skin is seen on the right hand side. Although measures are made to remove skin, this was sometimes difficult (personal communications). In two of the animals, the outermost sections consisted of lymph node tissue (Appendix F).

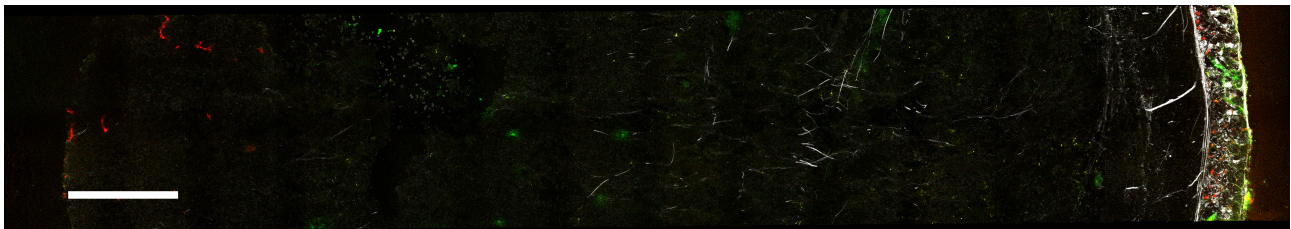


(a) Tile scan of collagen (grey), blood vessels (red) and NPs (green).

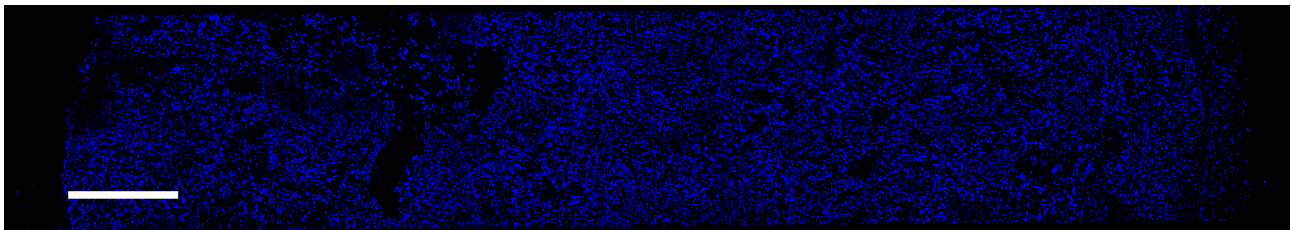


(b) Tile scan showing nuclei (blue).

Figure 4.20: Tile scan of animal A, short direction (as described in Section 3.6.1). Collagen and NPs can both be seen throughout the section. Blood vessels mostly in the periphery, but must be in the center as well due to the presence of nanoparticles. A 20X objective was used. The images are 1.0 mm x 5.8 mm. Scale bars are 500 μm .



(a) Tile scan of collagen (grey), blood vessels (red) and NPs (green).



(b) Tile scan showing nuclei (blue).

Figure 4.21: Tile scan of animal B, short direction. Some collagen and NPs are seen in the central area of the section, some large blood vessels in the periphery (left side). Skin is highly visible on the right hand side. A 20X objective was used. The images represent 1.0 mm x 6.2 mm. Scale bars are 500 μm .

4.5 In vitro nanoparticle uptake in cells

4.5.1 Flow cytometry to evaluate uptake in cells

The fourth barrier that the NPs have to overcome is the cells plasma membrane. To investigate whether any of the NPs were more likely than the others to be taken up, PC3 cells were incubated with NPs, and the amount of cells who took up NPs were counted using flow cytometry. The NPs were excited using a 488 nm laser. At least 10k cells were counted for each experiment. The NPs and cells were incubated for 3 and 6 hours, where 3 hours is the same time NPs were allowed to circulate in blood before the mice were euthanized in in vivo experiments. In addition, the cleavable NPs were cleaved by incubating them with an enzyme, thermolysin, which cleaves at the same amino acid sequence as MMP2 and MMP9. Removing PEG will increase interaction possibilities between the NPs and the cells, because of reduced sterical hindrance. In addition, after the enzyme cleaves off some of the PEG-layer, the cleaved cleavable NPs are expected to have a slightly less negative surface charge, which might increase uptake. To ensure that the thermolysin worked as expected, a cleavable NP which acquires a positive surface charge after cleaving off the PEG-layer was also incubated with thermolysin and subsequently by cells. Since cell membranes carry a negative charge, a positively charged NP is mainly expected to stick to the surface of the cell. To assess that uptake happened by endocytosis and not diffusion of fluorescent molecules to the cell membrane, control incubations at 4 °C were done for both 3 and 6 hours, a temperature known to be too low for endocytosis to happen. In addition, to test that neither thermolysin nor the HEPES buffer thermolysin works in affects the cells or the other nanoparticles, one experiment was performed where cells and NPs were incubated with HEPES buffer alone, and with HEPES buffer and enzyme.

As can be seen in Figure 4.22, after 3 hours of incubation at 37 °C, approximately 40 % of the counted cells shows uptake of the standard NP, while non-cleavable and cleavable NPs hardly were taken up (approximately 5 and 2 % respectively). Incubating for 6 hours at 37 °C increased uptake to approximately 82 % for the standard, 29 % for the non-cleavable, and 20 % for the cleavable NPs.

Uptake of the cleaved version of the cleavable NP was the same as the uncleaved version (32 and 29 % respectively) when incubated for 24 h at 37 °C. To test that the enzyme used for cleavage, it was applied to a second cleavable NP (not previously described) which becomes positively charged after cleavage. Due to opposite charges, these positively charged particles are expected to stick to the negatively charged cell membrane. The uptake for positively charged particles are expected to be large, as the flow cytometer does not separate between fluorescence inside and outside of the cell. As can be seen in Figure 4.23b, uptake of the positively charged version was higher than of the negatively charged version (approximately 78 % and 1 % respectively).

Table 4.3: Cellular uptake of the NPs without cleaving. Average of 3 experiments \pm standard deviation. Corresponds to Figure 4.23a

	Cleavable	Non-cleavable	Standard
Cellular uptake after 3 h incubation [%]	4.0 \pm 1.8	7.1 \pm 2.0	45.1 \pm 15.1
Cellular uptake after 6 h incubation [%]	21.6 \pm 7.2	32.3 \pm 2.7	84.4 \pm 1.4

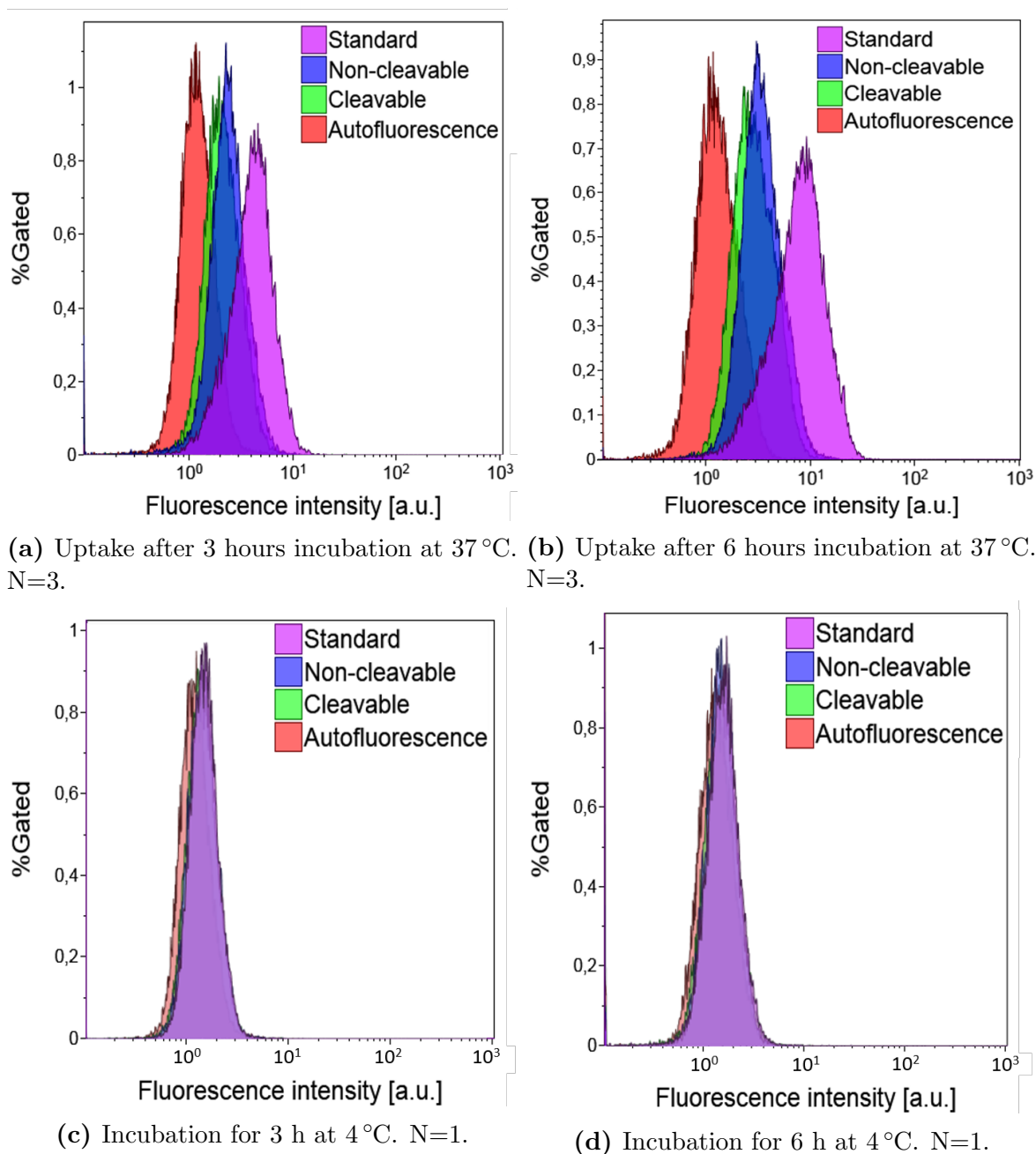
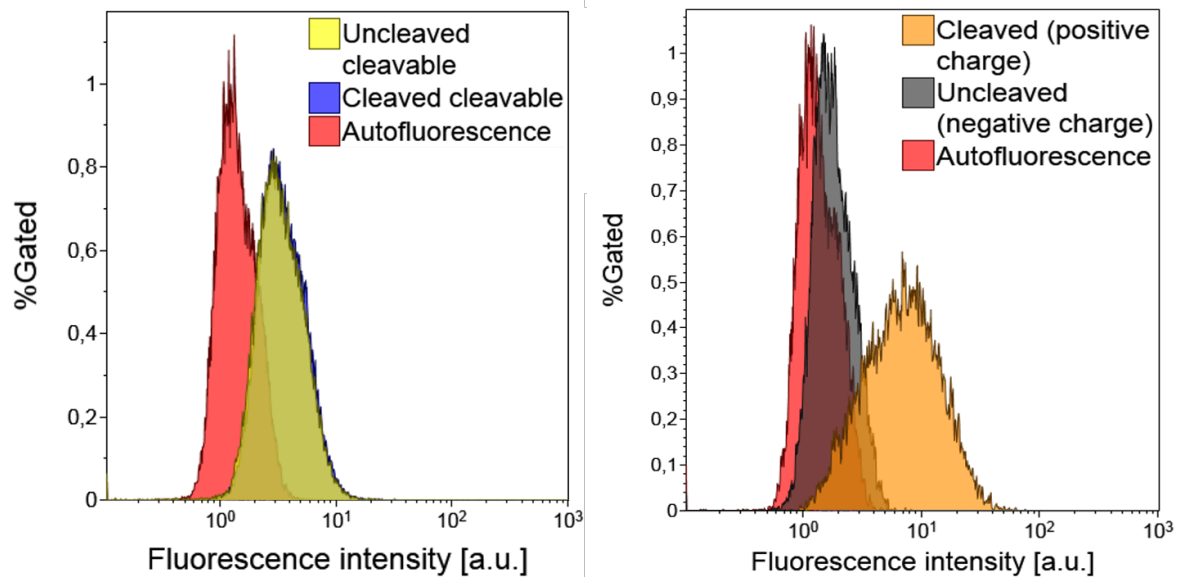


Figure 4.22: Histogram of uptake (3 NPs) measured by flow cytometry. X-axis is fluorescence intensity. a-b are NPs incubated with cells at 37 °C, c-d are NPs incubated with cells at 4 °C.

Table 4.4: Cellular uptake of the cleaved and uncleaved version of the cleavable NPs. Incubated with cells for 24 h. Average of 3 experiments \pm standard deviation.

	Uncleaved	Cleaved
Cellular uptake [%]	28.8 ± 3.9	31.6 ± 2.3



(a) Uptake of cleaved and uncleaved version of the cleavable NP after 24 h incubation at 37 °C. N=3. (b) Uptake of a NP which is positive after cleavage, to show effect of thermolysin. Incubated for 3 h at 37 °C. N=1.

Figure 4.23: (a) is incubation of uncleaved and cleaved cleavable NPs with cells for 24 h at 37 °C. (b) is the same experiment only using a cleavable NP which becomes positively charged after cleavage. The yellow-green color seen in (a) indicates the overlap between the uncleaved and cleaved cleavable NPs.

4.5.2 Microscopy of live cells

To evaluate whether the uptake of NPs (all uncleaved) seen by flow cytometry (Figure 4.22), live cells grown in microscope slide wells were incubated with NPs with incubation condition matching those seen in Figure 4.22b. An overview and a 2X zoomed in image was taken for each cell (Figure 4.24). These images confirm that the NPs (green) are indeed inside cells, and not attached to the outside of the cell membrane (red). Further, just like in the flow cytometer figure, it can be noted that the standard has a higher uptake than the non-cleavable, while the cleavable has very little uptake here. However, the difference in uptake between cleavable and non-cleavable was not significant in the flow cytometry spectra, while they seemed to be quite a difference in the microscopy images. It can be seen that the cleavable NP signal is overlapping with CellMask staining, creating yellow spots.

It should be noted that wells in which cells had been incubated with NPs contained fewer cells than wells where cells did not receive NPs (not shown), despite there being approximately the same number of cells in each well to begin with. The cells seemed to be nicely attached to the microscope well, with several filopodia seen.

Some autofluorescence was seen in cells which were not incubated with NPs (images not shown).

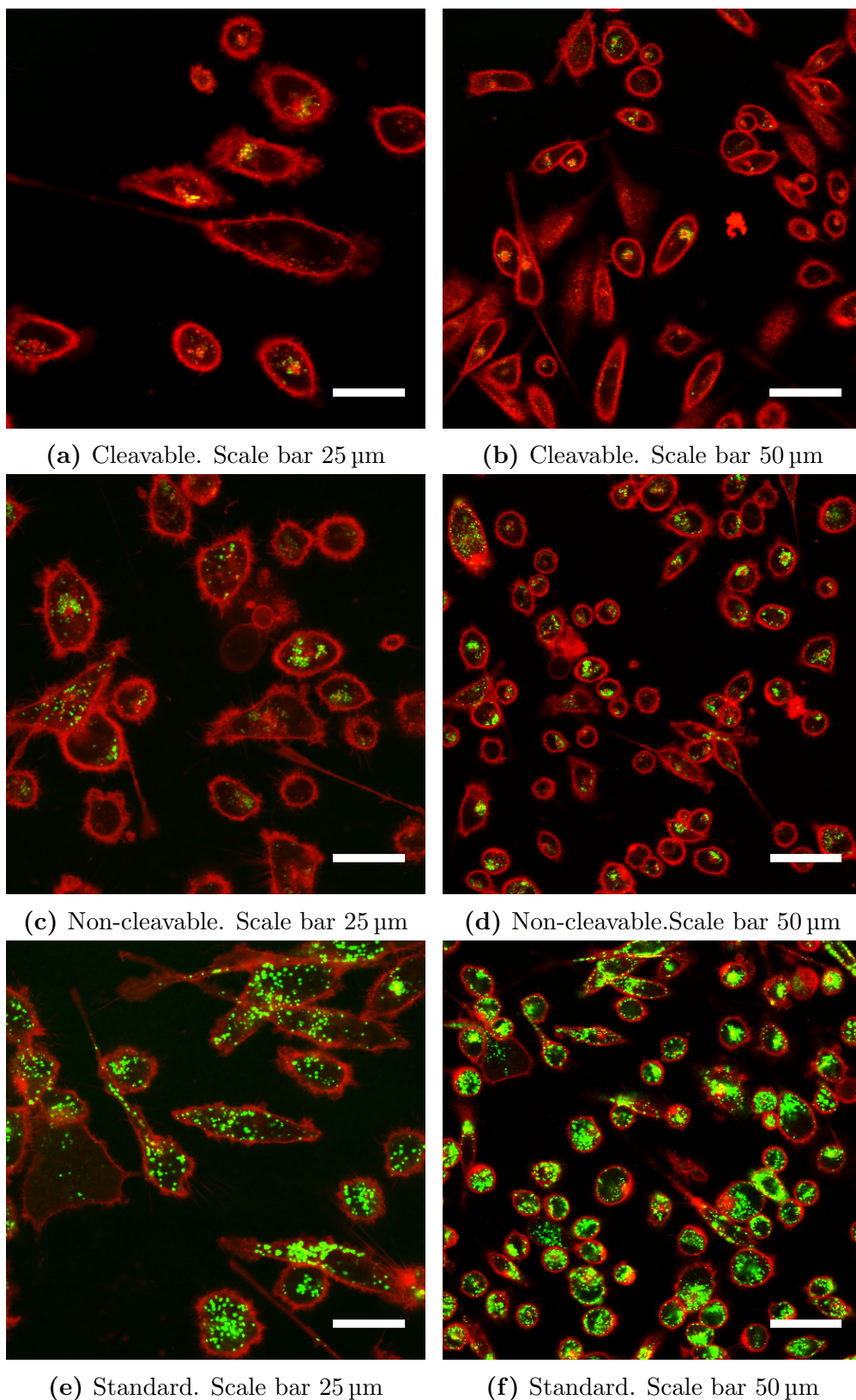


Figure 4.24: Microscopy images of live cells incubated with cleavable (top row), non-cleavable (middle row), and standard (bottom row). Left column contains zoomed in images (145x145 μm), and the right column contains overview images (290x290 μm).

Chapter 5

Discussion

Throughout experiments, we have followed the NPs across 4 barriers that must be overcome for successful cellular uptake after I.V. injection. If we do not address all the barriers, our work might be futile. For example, it is important to develop a drug delivery carrier which is easily taken up by cancer cells, but that carrier will not be beneficial to patients if it cannot reach the cancer cells. Many factors come into play when we enter biological systems, known for their high complexity and interconnectedness. Following is a discussion of the experiments conducted, the likely causes of the results, and how to interpret them. Extravasation and distribution of NPs in tumor ECM without US will be discussed separately from the cases where US is applied.

5.1 Stability and batch to batch variability

5.1.1 Temporal stability

Over time (4 months, NPs stored at 4°C) the peak fluorescence intensity dropped for both fluorophores in all three NP systems. The intensity of the Atto 700 dropped more than the intensity of Atto 488.

The reduction in fluorescence intensity could be due to photobleaching when the NPs are exposed to light. Atto fluorophores are, however, known to have a high photostability [58]. Further, NPs were kept protected from light between experiments, and effort was made to minimize light exposure during experiments. Therefore, photobleaching is not likely the main reason for loss of fluorescence signal.

It should be noted that the small increase (2-3 %) in fluorescence intensity of Atto 488 seen in the standard liposome over the 4 month time span is considered to be a small enough increase that it might be due to a pipetting inaccuracy. Alternatively, the possibility exists that the lipid-linked fluorophores were packed too tightly on the standard liposome surface, which could have caused them to be quenched. It follows that if some of the lipid components leaked from the double lipid membranes over time, this would free more surface space and reduce quenching, yielding a higher signal.

As a commercial drug delivery liposome is unlikely to contain fluorophores, intensity stability might not be of outmost importance, especially if it is caused by fading of the fluorophores over time. However, if the loss of signal over time is due to lipids being released from the liposome this would indicate an unstable structure, which could be a problem for drug delivery, unless the drug delivery liposome was designed to degrade.

It is reasonable to expect that loading the NPs with drugs are likely to affect the properties of the NPs. A hydrophilic drug would be carried within the aqueous core of the NPs, perhaps affecting size, and possibly altering the fraction of lipids with surface conjugates in the two water-lipid interfaces of the two membranes. Currently, fluorophores can be attached to the liposomes facing either into the core or out towards the surrounding medium. Loading the core with a drug might force the fluorophores or other conjugates to occupy the outer membrane due to lack of space. A hydrophobic drug would be loaded within the lipid double membrane, and unless it was very small would be likely to affect the size, fluidity and stability of the double membrane. It has been shown that loading liposomes with structurally similar drugs does not result in similar retention of the different drugs [59]. Drugs with a long shelf life can be produced in larger batches, which will reduce cost compared to unstable carriers which might have to be produced shortly before use. Therefore, stability is an important factor to be considered when developing drug delivery carriers, and the temporal stability should be assessed for the final version of the carrier.

5.1.2 Batch variability

From batch to batch, the non-cleavable had a 25 % drop in size (from 155 to 116 nm). As the ζ -potential didn't change much for the non-cleavable NPs, it can be argued that the amount of PEG is likely to be the same. The size difference of the cleavable and standard NPs between batches was not as prominent (mean size was 8 and 14 % reduction, respectively). For these two NPs the ζ -potential did change, with the cleavable becoming more anionic and the standard NPs becoming more neutral. It was also observed that, despite following the same production protocol, all the second batches came at a much lower concentration. Put together, all this information suggests that the preparation protocol does not have a satisfactory batch to batch reproducibility.

5.2 Aggregation in blood and serum components

The standard NPs formed larger structures than the cleavable and non-cleavable NPs. There were more aggregates of the standard NPs in PBS than in HEPES. For the cleavable and non-cleavable NPs, no prominent difference between solvents was observed. Particles did not stick to the red blood cells (video, not shown).

Qualitatively, the aggregates composed of more than 50 adjacent pixels are easily visualized and likely to be true clusters. However, since an aggregate was defined as two or more pixels above threshold adjacent on one of four sides (the sides of a square pixel), it must be noted that NPs could be interpreted as being aggregated while in reality only being within one pixel length (approximately 200 nm) from each other. This is part of the reason that "aggregates" of less than 5 connected pixels were excluded from the quantitative histograms.

It is believed that the salts in the PBS could have been the reason for the more and larger aggregations of the standard NPs observed when in PBS compared to HEPES. The ions would be able to stabilize local areas of surface dipoles, which could lead to coalescence if the PEG grouped in local areas of the surface and other surface areas were exposed and left with less steric hindrance. An illustration of how this possibly could happen is shown in Figure 5.1. It is unclear why the standard NPs aggregated (or coalesced) more than the cleavable and non-cleavable NPs. One likely reason is the difference in composition. Perhaps HSPC is more

likely to stick or merge compared to POPC, or perhaps the production method did not yield the expected PEG coverage, and that the sterical hindrance was different between the standard and the cleavable and non-cleavable NPs. It should be noted that the quantitative histograms were computed from 3 frames of the same sample, and that the difference might not have been as large if more repeats had been done.

Surprisingly, the addition of blood or serum to the NPs in buffer did not seem to affect the sizes or amounts of aggregates. Instead large aggregates were already observed in the buffer solution. It was believed that the serum proteins could bind to the lipids and change their surface properties, and thereby cause aggregation. Un-PEGylated liposomes has been found to aggregate and release content when exposed to serum proteins [60]. PEGylating liposomes have been found to reduce interactions with the serum proteins, but it cannot completely prevent the formation of a protein corona [26, 27]. The degree of protein corona formed depends on the amount of shielding, which often corresponds to the amount of PEGylation, as PEG has become the golden standard for inducing stealth [61]. Milosvits et al. found that a small fraction of Caelyx (liposome with doxorubicin) and the corresponding liposome without drug (Doxebo) forms large aggregates (>500 nm). It would appear that only an estimated billionth of the solution formed these large aggregates, and that more formed after storage, indicating an insufficient storage stability [62]. The standard liposome here should have the same lipid composition as the Doxebo, except for the addition of fluorophores. Although not quantified, the concentration of larger aggregates seen in this thesis was likely higher than what Milosvits et al. found, given their ease of detection by fluorescence microscopy. Of course, as the standard NPs have lipid anchored fluorophores, that might be enough to cause increased aggregation compared to the Doxebo which should have the same composition except for fluorophores. However, as aggregation was been found in both Doxebo and Doxil/Caelyx, it is reasonable to deduce that the formulation can lead to the formation of large aggregates, albeit a low concentration of such.

It is important to consider the effect of the large aggregates when injected in blood. First, the presence of a few large aggregates might not be a problem for successful extravasation, penetration and cellular uptake, as the majority of the particles were very small. Considering that the particles less than 5 connected pixels were not included in the histograms in Section 4.1.3, it is clear that the majority of NPs remain small enough to extravasate, penetrate ECM, and be taken up by cells. However, the large NPs could harm the patient by blocking capillaries, and cause local cell death. Indeed, when the animals were euthanized, tumors and some organs of interest were dissected out and fluorescence was imaged in the whole animal optical imager (Appendix E). Animals receiving standard or cleavable NPs did show signs of necrotic areas in the lungs in more cases compared to animals receiving the non-cleavable NPs, only 3 hours post injection (personal communications). The lungs contain the first capillaries the NPs arrive to after being injected, and it would appear that more of the cleavable and standard NPs get stuck there (Appendix E). This means that less of the cleavable and standard NPs remain in circulation, available for extravasation into the tumor interstitium (see biodistribution data in Appendix E).

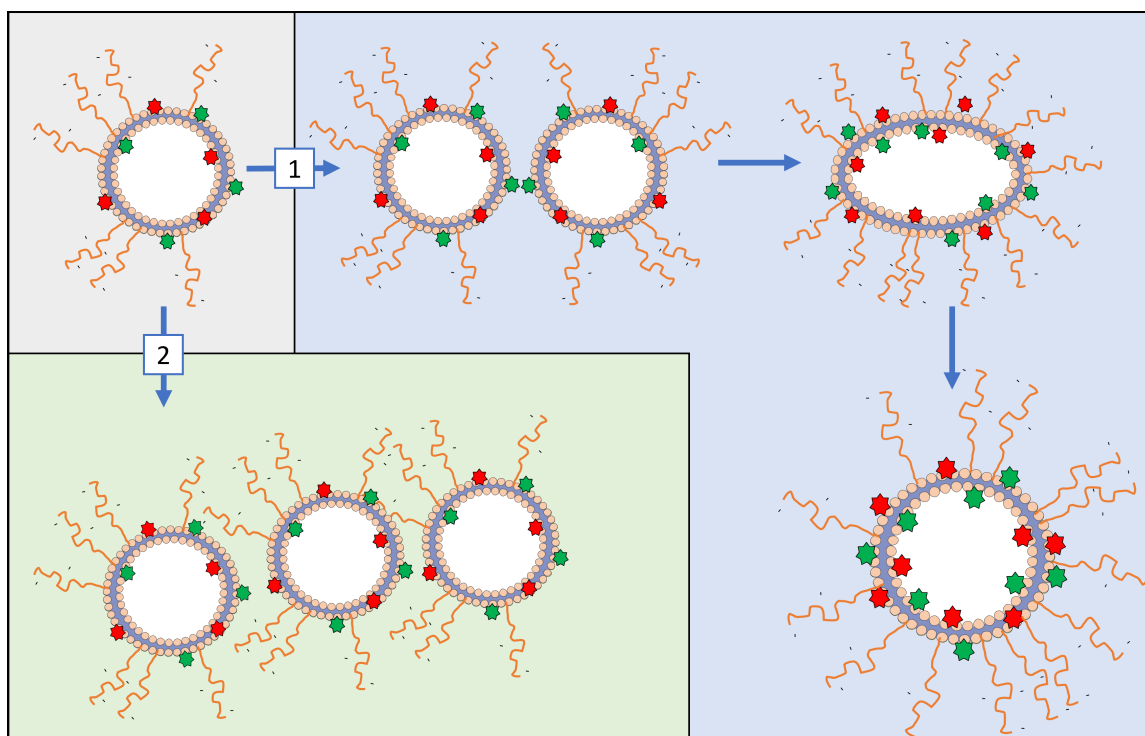


Figure 5.1: Illustration of two ways the large aggregates observed could have formed. Path 1 shows coalescence and path 2 shows particles sticking together, either aggregating or agglomerating. Both paths start with a heterogeneous distribution of PEG on the outer lipid-water interface, leading to areas with reduced steric hindrance. Free ions in solvent are not shown, but expected to contribute in stabilization of the heterogeneous distribution of PEG, aggregation, or enable coalescence. Aggregation is used in the text to describe all cases of particle clusters. Made by the author using Servier Medical Art ©.

5.3 Extravasation of NPs without ultrasound

In all control animals, for all three NPs, both large and small degrees of extravasation was seen. The median % extravasation values for the US groups were higher than for the control groups, with one exception. The Low MI group of the cleavable liposome had the lowest median extravasated value of all the groups. As the control animals were not exposed to US, the extravasation seen in these groups should be due to the EPR effect.

All three control groups had similar degrees of extravasation, with mean values from 35 to 40 %. However, it can be seen both in Section 4.2.1 and Appendix B, that there are large variations from animal to animal, and from image to image within the same animal.

Images where the ratio of NPs outside to inside blood vessels was low, could represent blood vessels with low permeability. Alternatively, these images could represent tissue where a high interstitial pressure prevented extravasation of NPs.

In contrast, the images where a high fraction of NPs appeared to have had extravasated, could be depicting highly leaky vessels, or a local interstitial pressure drop. However, it is also possible that these results were an indication of poorly stained vessels. Blood vessels were stained with lectin 3 hours after the NPs and MBs were injected. If NPs blocked a vessel, or the blood vessel shut down, or if the perfusion of blood vessels diminished between NP injection and lectin injection, the lectin would not be able to properly stain endothelial cells. Any NPs

that were inside an unstained vessel would falsely be interpreted as being extravasated. Images where little blood vessels were stained were still included as it would be impossible to remove them without being unbiased and correctly separate images of a highly permeable vessel from an unstained one.

Unezaki et al. showed extravasation of 133 nm and 198 nm PEGylated liposomes into a solid tumor known for highly permeable vessels [63]. Hashizume et al. report vessel pore cut-off sizes between 200 nm and 2 μm for a tumors with variable leakiness [25]. These results indicate that there is at least a possibility that pore sizes in PC3 tumors could be large enough to allow for extravasation of the NPs used here, all less than 175 nm unless aggregated, and the microscopy images would agree that extravasation did happen to some degree in several vessels. Sulheim et al. investigated five tumor models, including PC3, and found that PC3 had a medium-low degree of vascularization and overall low nanoparticle uptake compared to the other models [64].

Krasnici et al. investigated the effect of surface charge on targeting the angiogenic endothelium in tumors [65]. They found that positively charged liposomes significantly accumulated in solid tumor microvessels, while neutral and anionic liposomes only had a weak correlation with tumor vasculature compared to surrounding, healthy tissue. The cationic liposomes were found to stay in the blood vessels, likely attached to negatively charged angiogenic cells, while neutral and anionic liposomes showed some extravasation into the tumor ECM. As they did not apply any external or internal means to facilitate extravasation, the EPR effect can be assumed to have been the main reason for extravasation. Krasnici et al. did not report a significant difference in extravasation of neutral and anionic liposomes, and therefore it might not be expected that there will be a difference between the NPs used in this thesis, who all have a negative ζ -potential. Further, the NPs used in this thesis are expected not to adsorb to angiogenic blood vessel cells.

Although the EPR effect is acknowledged in animal models, it is highly disputed in humans [30]. Therefore, US and MBs have been exploited to increase extravasation and distribution in tumors, which will be discussed later.

5.4 Distance travelled through ECM without ultrasound

Considering the control animals, more than 75 % of extravasated particles did not diffuse farther than 5 μm from the nearest blood vessel. The cleavable NPs had the lowest fraction of particles at 5 μm and therefore more cleavable NPs in the control animals traveled farther compared to the other NPs in their respective control animals. However, the cleavable had the highest fraction of NPs at 10 μm , and after approximately 25 μm it was difficult to see any difference.

As for the passive extravasation described above, the distance travelled for extravasated particles is governed by diffusion and convection gradients. The diffusion gradient would lead the particles to spread from the vessel, but tumor ECM and cells within would act as a physical barrier. The standard NPs were approximately 25 nm smaller in diameter compared to the cleavable and non-cleavable NPs. The cleavable and non-cleavable were of comparable sizes. The size difference could cause the standard NPs to travel further if only they were small enough to pass through the dense structural network. This cannot be observed from the distribution histogram, as the standard NPs have a higher fraction which did not diffuse more than 5 μm . Likely, the size difference is too small for to affect diffusion.

Another factor that will affect distance travelled is interactions with the local cells and

other constituents of the ECM [66]. The interactions will be affected by surface charge, which is negative for ECM components and cellular membranes. Based on the characterizations of the NPs, the standard NPs are the most negative, followed by the cleavable, and the non-cleavable. Repulsion between two negative objects will stop them from sticking to each other. However, after the NPs have travelled through blood, it is expected that some proteins have adsorbed onto the NPs and form a protein corona, despite the steric hindrance provided by PEG. These proteins could change the surface charge of the NPs. A protein corona would likely make the particles more anionic, as proteins in blood carry an overall negative charge, but depending on the proteins attaching it is probably possible that the corona could make the NPs more neutral. Either way, proteins attaching would have an effect on the distance travelled by changing the interactions of NPs with the ECM.

Cells can hinder diffusion by taking up NPs. If NPs were taken up by cells near a blood vessel, or even by the endothelial cells making up the vessel wall, it would be unlikely that escape on the other side of the cell and travel further.

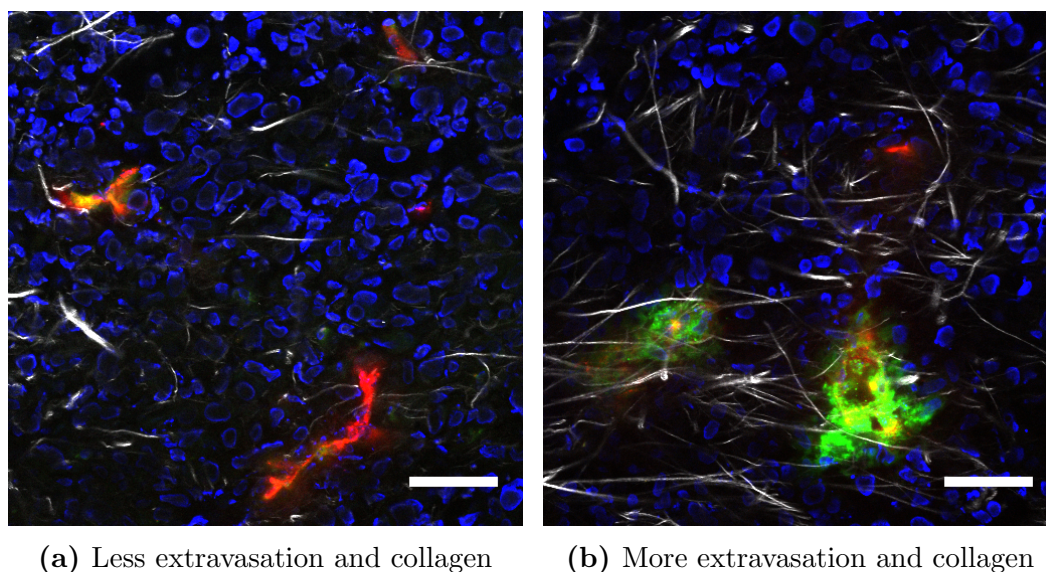
If we compare the cleavable and the non-cleavable NPs, the cleavable NPs seemed to travel further from blood vessels. It is possible that MMP2 and -9 enzymes have cleaved off the PEG and that the cleavable NPs therefore have become smaller and/or attained a new surface composition which increased their diffusion coefficient. However, the activity of MMP2/-9 was not measured in the tumors. 3 hours should be sufficient to cleave all PEG, given that there are enough active enzymes available, but this has not been evaluated. It is therefore difficult to say whether cleaving caused the cleavable NPs to travel minimally farther than the non-cleavable NPs. Further, it should be considered that any PEG molecules cleaved off of the cleavable NPs could provide additional sterical hindrance if not removed.

According to V. Sereti, cleaving the PEG did not change the surface charge of the cleavable NPs. This would imply that the surface of the particles is charged, despite being made up of neutral and zwitterionic lipids. Had the cleavable NPs changed surface charge, it would likely have affected the diffusion coefficient of the NPs. This is because the coefficient is dependent on particle interactions with its surroundings (e.g. probability of sticking to structures, particles or cells), and size in the form of the hydrodynamic radius [32].

5.5 Tumor heterogeneity and variability

Blood vessels and NPs were found in both peripheral and central areas of the tumor sections imaged, the same was true for collagen. Both blood vessels and collagen were expected to be more frequently observed at the periphery of the tumor compared to the center, as PC3 cells are known to be a cell line with a relatively low degree of vascularization [64]. Although the distribution of collagen, blood vessels and NPs throughout the tumor was investigated by tile scans of only two animals, these tile scans were representative of all the tumor sections observed when searching for blood vessels and NPs in the ocular prior to imaging individual vessels (represented in the schematic of sweeping pattern across a tumor section in Section 3.6).

It appears likely that the heterogeneous nature of the tumors, both between animals and within tumors could be the explanation of any apparent effects or differences, or indeed hide any small, local effects. In addition, the heterogeneity could explain the large variations seen within groups, especially for extravasation. In the same tumor section, vessels with both very low and very high % extravasation was seen. A depiction of this is seen in Figure 5.2, which includes two images taken of vessels in the same tumor section.



(a) Less extravasation and collagen (b) More extravasation and collagen

Figure 5.2: Two images from the same tumor section, a control animal who received standard NPs. Blood vessels in red, NPs in green, nuclei in blue and collagen in grey. Yellow represents the overlay of blood vessel and NPs, i.e. NPs within blood vessels. Color brightness have been adjusted for clarity. Separate images of blood vessel and nanoparticles can be seen in Appendix C. Scale bars are 50 μm .

5.6 Effect of US and MBs on extravasation

It was observed that exposure to ultrasound and microbubbles increased extravasation compared to their respective control groups, again, except for the low MI group of the cleavable NPs.

For NPs to extravasate they must be in the tumor tissue vasculature. Extravasation in animals exposed to US will therefore be discussed and compared to biodistribution data of the whole tumor (Appendix E). The biodistribution data shows the total fluorescence measured from the tumor and the vessels within the tumor. Extravasation data shows the ratio of NPs outside vessels in images of individual vessels. The extravasation data is collected from 3 25 μm thick sections, and therefore does not necessarily represent the whole tumor, which were approximately 10 x 10 x 8 mm^3

Cleavable NPs

It was surprising that the median % extravasation was higher in the control group than the low MI group. Especially since the images of the whole tumor showed an increase of fluorescence intensity per gram for both low and high MI groups compared to the control. The low extravasation of particles exposed to low MI US could be due to animal heterogeneity in blood vessel distribution and size, as well as tumor interstitial pressure. It is also possible that the low extravasation seen throughout the low MI group indicates that the treatment somehow affected blood vessel permeability. Previously, during the project which evaluated only the cleavable NPs, it was believed that the large difference between the low and high MI groups showed an increased extravasation of NPs when exposed to high MI, and that the reason the control group had a higher median extravasation and mean distance travelled than the low MI group was due to heterogeneity in the control group. Back then, the control group consisted of only two animals, and one of them had extraordinary leaky vessels. Since then, another control animal has been added to the cleavable group, and the extravasation seen is still higher than

the low MI group, likely because the control animal which most likely had hyperpermeable vessels was not removed from the control group.

Non-cleavable NPs

For the non-cleavable NPs the low MI group had an overall increase in extravasation compared to the non-cleavable high MI and control groups. The low MI group had no images of blood vessel where less than 10 % of NPs had extravasated, and all animals had vessels where more than 90 % of NPs were outside of vessels (Appendix B). Imaging the whole tumor indicated, however, that the high MI group had more NPs per gram of tissue compared to the low MI and control groups. It could be envisioned that the non-cleavable NPs interacted with MBs during the stable cavitation, leading to increased extravasation. If the MBs exposed to low MI is expected to cavitate over the entire US pulse duration. In contrast, it is possible that the high MI caused implosion of MBs early in the US exposure period, and that the gas failed to re-cavitate yielding a strong but short lived force on the endothelial cells. Therefore, the cavitation effect of low MI lasted over the entire US pulse duration, while the high MI effect might have been very short, although strong. To get a deeper understanding of this, the cavitation signal could be detected by US for MBs mixed with the different NPs and exposing them to both low and high MI. These data have recently been collected and are currently being analyzed. Preliminary analysis indicates that the NPs did not interact with the MBs, but this was measured in buffer and interactions could be different in blood after the particles and bubbles were exposed to serum proteins.

Standard NPs

For the standard group, the effect of low MI and high MI seemed not to differ, and both had a slightly higher median % extravasation than the standard control group. This is in coherence with the biodistribution data (Appendix E), which indicated that all the animals receiving standard NPs had approximately the same amount of NPs located in the tumor.

It is difficult to explain why the extravasation yielded different results between the three NPs. It can be argued, that for cleavable and standard NPs, the high MI seemed to be more useful for increasing extravasation, while this was not true for the non-cleavable NPs. This argument does not, however, explain why the cleavable NPs in the low MI group had lower extravasation than the control animals. Of course, this observation could be explained by all the animals in the cleavable low MI group having vessels with a low EPR effect. A low responding group would further help explain why the biodistribution data showed that the total tissue uptake showed more NPs in the low MI cleavable group compared to the control cleavable group. More animals should be added to check if the 3 low MI cleavable animals really all had vessels with low permeability, or if the US and/or MBs somehow caused the NPs present not to extravasate. Finally, it must not be forgotten that there is a possibility that the section imaged might not have been representative for the overall tumor uptake.

The biodistribution data also showed that the tumors in the non-cleavable high MI group contained more NPs than the non-cleavable low MI group. Therefore it seems like the low MI US yielded higher extravasation of non-cleavable NPs compared to high MI US. Again, heterogeneity cannot be ruled out, but the cleavable and non-cleavable should behave very similar based on their compositions, making these results very interesting. Perhaps the difference in low MI extravasation between cleavable and non-cleavable NPs indicates that the production did not yield the expected, similar, NP formulations.

The percentage of particles imaged which were extravasated from their associated blood vessel varied enormously from vessel to vessel, within animals, from almost having no NPs extravasated to almost all NPs having extravasated. The first phenomena can easily be expected

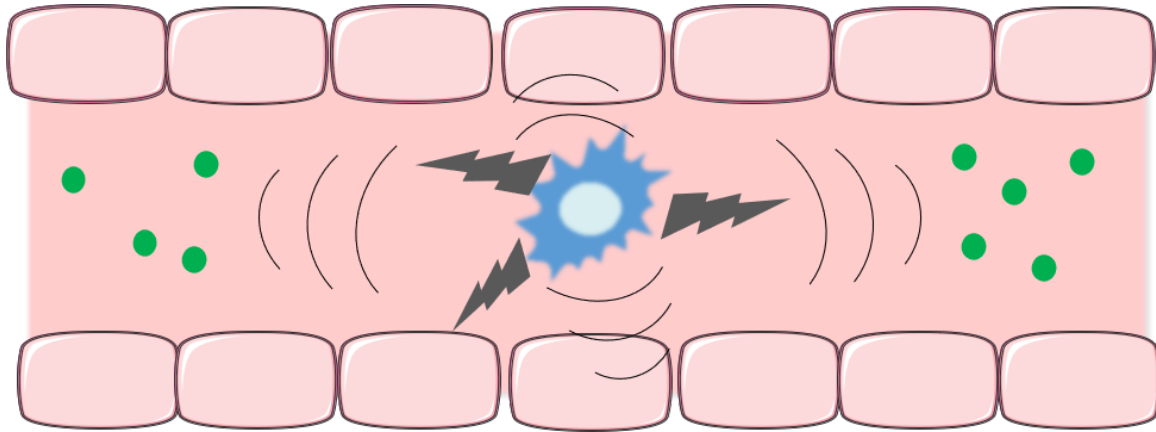


Figure 5.3: Illustration of an imagined MB implosion pushing the NPs (green) along the vessel instead of toward the endothelial cells. Made by the author using Servier Medical Art ©.

to be due to a vessel with low permeability, while the second is most likely to be caused by unstained blood vessels. However, it is difficult to know for sure whether the poorly stained vessels are so due to a chance change in blood perfusion, or if it was a consequence of the ultrasound exposure. For example, all three animals in the non-cleavable, low MI group had several vessels that were possibly poorly perfused, while this was true for only one or two animals in all the other groups. Again, it is evident that including more animals are necessary before reaching definitive conclusions.

Low MI US has been shown to cause stable cavitation [67]. Cavitating MBs have been shown to increase blood vessel wall permeability in the brain, and the mechanism is hypothesized to be a local shear force on the vessel wall by the cavitating MBs [68, 42].

High MI US has shown to cause implosions that releases a shock wave or jet stream towards blood vessel walls [45, 69], but it is difficult to control when this happens and where the implosion happens with respect to NPs. It is easy to imagine that if the implosion is immediate after starting US exposure, the effect might be too short lived to really produce lasting increased permeability. Alternatively it can be envisioned that an implosion could push the NPs away along the vessel luminal space, instead of towards the vessel walls (illustrated in Figure 5.3). However, Brujan et al. showed that microjet formation in vitro after high MI US could produce forces as large as 50 MPa on surroundings, which they believe is a high enough force to damage cell walls [69]. They found that the jet forces acted on a surface for 1 μ s, and that the force quickly diminished with distance from implosion site, underlining the importance of bubble location with respect to the blood vessel wall [69].

5.7 Effect of US and MBs on tumor penetration

NPs penetrate further from the blood vessels in animals exposed to low and high MI ultrasound in the non-cleavable and standard NPs compared to the respective controls. The same increased penetration was seen for the cleavable NPs exposed to high MI US, compared to controls. This is consistent with the amount of extravasated NPs, i.e. the more extravasated particles, the higher the chemical gradient promoting diffusion towards the center. However, it is possible that the US affected local convection by compression and expansion of the tissue as the ultrasound passed through the ECM. A vibrating ECM could have induced streaming of interstitial liquid,

which could have transported NPs. It would be interesting to see if there would be an increase in penetration distance if the US was applied for a longer total time span. However, that would require subsequent refills of MBs, as the circulation half life time is only a few minutes for Sonovue MBs.

Larger distances travelled were observed in images with a low amount of blood vessels when US was applied, indicating that the effect of cavitation is largest on small vessels. This is consistent with the notion that in small vessels, MBs are more likely to be in close proximity to the vessel wall. The increase in distance travelled from small vessels was seen for both low and high MI, for all 3 NPs.

Our results are consistent with the study by Theek et al. investigating the effect of high MI US to improve extravasation and distribution of NPs in two tumor models (A431 cells (human epidermoid) and BxPC-3 cells (human pancreatic adenocarcinoma)), both displaying a relatively low EPR effect. They found a trend towards higher uptake and further penetration when US was applied, but also saw inter- and intratumoral variations [70]. Theek et al. used two types of microbubbles, one soft-shelled similar to the Sonovue used here, and one hard-shelled. The different MBs were expected to have different oscillation potential due to a difference in shell rigidity. The US was applied continuously for 10 minutes, while in this thesis the total US exposure was 2 minutes. Theek et al. monitored uptake by hybrid computed tomography–fluorescence molecular tomography (CT-FMT) for up to 48 hours. Their results showed a significant uptake of NPs in each of the two tumor models, by one of the MBs (soft shelled for BxPC-3, and hard-shelled for A431). The significant uptake by CT-FMT was measured 24 h after US exposure, while no significant differences were seen at 4 or 48 hours. They further confirmed increased penetration of NPs in tumors exposed to US by ex vivo TPLSM. Since the animal experiments analyzed in this thesis were terminated 3 hours after NP injection and US exposure, they can only be compared to CT-FMT results after 4 hours by Theek et al., which did not indicate significant tumor uptake. It is possible that the effect of US would be clearer had the NPs been able to extravasate for a longer time.

Chen et al. used a high speed camera to visualize MB and blood vessel interactions. They observed deflections of the vessel wall, which in turn must have pushed and pulled on the adjacent interstitium [71]. This can potentially explain the increased distance travelled when ultrasound is applied, and MBs undergo stable cavitation.

When comparing mean distance travelled with the amount of collagen present in the image, it would appear that the tumors which received US penetrated farther, mostly in images with little collagen, but also to some extent in images with a relatively high collagen content. This could indicate that US yields an increase in tumor penetration, and that the effect is larger where there is little collagen to begin with.

5.8 Cellular uptake

The highest cellular uptake in vitro was of the standard NPs (45 ± 15 % and 84 ± 1 % after 3 and 6 hours respectively). There was no difference in uptake of cleavable and non-cleavable NPs, and neither were taken up to a significant degree after 3 h incubation at 37 °C (4 and 7 %, respectively). After 6 hours the cellular uptake of cleavable and non-cleavable was increased to 22 and 32 %, respectively. Cleaving PEG off of the cleavable NPs did not increase cellular uptake. Uptake was established to be due to endocytosis, as no signal was seen when incubating the cells and NPs at 4 °C for 3 and 6 h. At 4 °C, cellular functions are low, and any signal

seen at this temperature would be expected to be due to exchange of lipid-anchored dyes from the particles and into the cell membrane. Cellular uptake was measured by flow cytometry. Since flow cytometry does not separate between cells that have taken up NPs internally and cells with NPs attached to the surface, cells incubated with NPs were also imaged by confocal microscopy (Leica TCS SP8). The increased cellular uptake of standard NPs compared to the other two was also seen qualitatively in live cell microscopy. Here a clear difference was seen in uptake of the three different NPs. The difference was in agreement with the flow cytometry data, except that the flow cytometry did not show an as clear difference between cleavable and non-cleavable as was seen by microscopy. All three NPs were observed internalized in cells.

By microscopy, the cleavable NPs were observed co-located with CellMask, which stains lipid structures such as the cell membrane. According to the distributor the CellMask is slow to leak into the cells, and since cells were imaged directly after applying the CellMask, internal organelles and vesicles with lipid membranes (e.g. the nucleus) should not have been stained. This could indicate that the cleavable NPs imaged were located within endosomes, or the nucleus. The non-cleavable and standard did not show overlap with CellMask to the same degree, and this could indicate that the routes of uptake varies between cleavable NPs and the other two, or that standard and non-cleavable manages to escape the endosomes and end up in the cytoplasm. As flow cytometry did not show a difference in uptake of the cleaved and uncleaved version of the cleavable NPs, the cleaved version was not imaged by microscopy.

The main lipids in the NPs, POPC for cleavable and non-cleavable and HSPC for standard NPs are phosphatidylcholines, and therefore should behave similarly. Likewise, all three NPs should have the same fraction of PEG coating, but it is already pointed out that the production is not necessarily reproducible. Perhaps the expected molar ratios in each type of NP was not achieved, and that e.g. the molar fraction of PEG differed enough to somehow reduce the uptake of cleavable and non-cleavable NPs. Otherwise, the PEG is attached to cholesterol for the cleavable and non-cleavable, and for a phospholipid for the standard NPs. Perhaps this could affect interactions with the cells, and thereby uptake. When Doxil/Caelyx was clinically approved for encapsulating doxorubicin, it was approved based on the improved toxicological profile, and not for any increased uptake in the tumor [72]. Therefore, it does not explain why the standard NPs, which supposedly have the same lipid composition is favored for cellular uptake compared to the cleavable and non-cleavable NPs.

Despite differences in uptake in vitro it should always be remembered that the same uptake will not necessarily be seen in vivo, and that NPs taken up might not be able to deliver their loads to the desired compartment due to different mechanisms of drug resistance [73]. Escaping the endosomal pathway is necessary for a successful delivery, as the pathway usually either end in lysosomal degradation of the content or exocytosis for foreign material. It has been thoroughly reviewed in literature [74, 75, 76], but clinical trials focusing on endosomal escape is not extensively described yet. As the NPs used here are drug free, the endosomal pathway has not been addressed, but should be in future applications.

Further, it was observed by light microscopy that after washing and staining of cells, the total amount of cells were reduced compared to a well which had not received NPs or CellMask. This could indicate that the washing is too aggressive, or that some cells were poorly attached or dead after being incubated with NPs.

5.9 Clinical relevance, suggestions for improvement and future outlook

A small clinical trial with ultrasound, microbubbles and a free drug has shown that the ultrasound and microbubbles does not have detrimental toxicity effects, and several patients had a positive outcome [10]. It follows that clinical trials with ultrasound, microbubbles and nanoparticles would be a natural step forward. There is ongoing research trying to establish ways to evaluate tumors for e.g. leakiness of vasculature, degree of vasculature, and interstitial pressure, thereby identifying cancer patients that can benefit from treatment with drug loaded NPs [77, 78, 79].

To get more conclusive results regarding uptake and distribution, more animals should be imaged and added to each group. It should be noted that although control animals which show a response such as high degree of extravasation or particles diffusing far into the tumor due to structural features and high permeability, is not an unfortunate event. Even though highly responsive control animals will make the animals responding to treatment stand out less, it will always be tumors with different levels of response, and it's the low responding tumors that has the highest need for treatment to get them up to the level of high responding tumors.

Evaluation of blood vessel leakiness in an animal prior to treatment would strengthen the argumentation for increased extravasation by ultrasound and microbubbles. This could e.g. be done by analysis of the interstitial pressure, or perhaps live imaging of blood flow in tumors by Doppler mode ultrasound or using window chambers to evaluate vessel permeability using a fluorescent molecule. Of course, extravasation of small molecules might not correlate with extravasation of larger NPs, but it could give an indication of the overall leakiness. To better assess the extravasation properties of NPs, a test NP could be used, e.g. one with a magnetic core which could be imaged by MRI.

Likewise, monitoring tumors post treatment for known effects such as change in oxygenation or temperature, could help post-treatment outlook by identifying respondents and non-respondents early in the treatment scheme [80].

Chapter 6

Conclusion

Throughout this semester, three nanoparticle formulations loaded with two fluorophores have been characterized for fluorescent properties by fluorescent spectra, their extravasation and distribution in tumor tissue has been evaluated by confocal microscopy, and cellular uptake in vitro has been examined by flow cytometry and complemented by confocal microscopy. The major trends and observations were:

There was no clear aggregation behaviour of the nanoparticles observed when added to blood and serum, but more aggregates were observed in general for the standard nanoparticles, compared to the other two nanoparticles. This was supported by biodistribution data which showed a high distribution of standard, but also cleavable nanoparticles in the lungs. which showed a high distribution of standard, but also cleavable nanoparticles in the lungs.

A minimal increase of extravasation was observed in tumors exposed to ultrasound, with the exception of the tumors in the low mechanical index cleavable group. Total extravasation was not measured as the imaged sections only represented a fraction of the tumor volume. The highest extravasation was observed for the non-cleavable nanoparticles, when exposed to ultrasound with a low mechanical index. However, more animals need to be imaged to ensure that the effect of ultrasound was not due to heterogeneity.

Ultrasound also resulted in a minimal increase in penetration distance by nanoparticles in tumor tissue. The increase seemed larger in images with a low blood vessel area. Mean penetration distance increased independently of collagen present in the image.

The standard nanoparticles were taken up in cells much more frequently than the cleavable and non-cleavable nanoparticles. Cleaving of poly(ethylene glycol) did not affect cellular uptake in vitro.

Going forward, more animal experiments should be conducted and evaluated to clearly distinguish effects of ultrasound from intrinsic animal-to-animal variations. It would also be useful to develop a baseline for individual tumor permeability to successfully evaluate true effects of microbubbles and ultrasound.

Bibliography

- [1] J. Hardin and G. Bertoni. *Becker's World of the Cell*. 9th ed. Pearson Education, 2018. Chap. 26, pp. 802–834.
- [2] R. K. Jain. “Understanding Barriers to Drug Delivery: High Resolution in Vivo Imaging Is Key”. In: *Clinical Cancer Research* 5 (1999), pp. 1605–1606.
- [3] K. A. Kurdziel, J. D. Kalen, J. I. Hirsch, J. D. Wilson, H. D. Bear, J. Logan, J. McCumisky, K. Moorman-Sykes, S. Adler, and P. L. Choyke. “Human dosimetry and preliminary tumor distribution of 18F-fluoropaclitaxel in healthy volunteers and newly diagnosed breast cancer patients using PET/CT”. In: *Journal of nuclear medicine: official publication, Society of Nuclear Medicine* 52 (2011), p. 1339.
- [4] D. Peer, J. M Karp, S. Hong, O. C Farokhzad, R. Margalit, and R. Langer. “Nanocarriers as an emerging platform for cancer therapy”. In: *Nature nanotechnology* 2 (2007), p. 751.
- [5] J. V. Jokerst, T. Lobovkina, R. N. Zare, and S. S. Gambhir. “Nanoparticle PEGylation for imaging and therapy”. In: *Nanomedicine* 6 (2011), pp. 715–728.
- [6] N. Kamaly, Z. Xiao, P. M. Valencia, A. F. Radovic-Moreno, and O. C. Farokhzad. “Targeted polymeric therapeutic nanoparticles: design, development and clinical translation”. In: *Chemical Society reviews* 41 (2012), pp. 2971–3010.
- [7] V. Sanna, N. Pala, and M. Sechi. “Targeted therapy using nanotechnology: focus on cancer”. In: *International journal of nanomedicine* 9 (2014), p. 467.
- [8] O. M Koo, I. Rubinstein, and H. Onyuksel. “Role of nanotechnology in targeted drug delivery and imaging: a concise review”. In: *Nanomedicine: Nanotechnology, Biology and Medicine* 1 (2005), pp. 193–212.
- [9] H. Maeda, J. Wu, T. Sawa, Y. Matsumura, and K. Hori. “Tumor vascular permeability and the EPR effect in macromolecular therapeutics: a review”. In: *Journal of Controlled Release* 65 (2000), pp. 271–284.
- [10] G. Dimcevski, S. Kotopoulis, T. Bjånes, D. Hoem, J. Schjøtt, B. T. Gjertsen, M. Biermann, A. Molven, H. Sorbye, E. McCormack, M. Postema, and O. H. Gilja. “A human clinical trial using ultrasound and microbubbles to enhance gemcitabine treatment of inoperable pancreatic cancer”. In: *Journal of Controlled Release* 243 (2016), pp. 172–181.
- [11] D. Hanahan and R. A. Weinberg. “Review Hallmarks of Cancer: The Next Generation”. In: *Cell* 144 (2011), pp. 646–674.
- [12] P. S. Ward and C. B. Thompson. “Metabolic Reprogramming: A Cancer Hallmark Even Warburg Did Not Anticipate”. In: *Cancer Cell* 21 (2012), pp. 297–308.
- [13] L. Floor, J. E. Dumont, C. Maenhaut, and E. Raspe. “Hallmarks of cancer: of all cancer cells , all the time?” In: 18 (2012), pp. 509–515.
- [14] J. A. Nagy, S.-H. Chang, A. M. Dvorak, and H. F. Dvorak. “Why are tumour blood vessels abnormal and why is it important to know?” In: *British Journal of Cancer* 100 (2009), pp. 865–869.
- [15] A. M. Jhaveri and V. P. Torchilin. “Multifunctional polymeric micelles for delivery of drugs and siRNA”. In: *Frontiers in Pharmacology* 5 (2014), p. 77.
- [16] P. Lu, V. M. Weaver, and Z. Werb. “The extracellular matrix: A dynamic niche in cancer progression”. In: *The Journal of Cell Biology* 196 (2012), pp. 395–406.
- [17] M. W. Pickup, J. K. Mouw, and V. M. Weaver. “The extracellular matrix modulates the hallmarks of cancer”. In: *EMBO reports* 15 (2014), pp. 1243–1253.

- [18] M. Wagner and H. Wiig. “Tumor Interstitial Fluid Formation, Characterization, and Clinical Implications”. In: *Frontiers in Oncology* 5 (2015).
- [19] H. Wiig, D. Keskin, and R. Kalluri. “Interaction between the extracellular matrix and lymphatics: Consequences for lymphangiogenesis and lymphatic function”. In: *Matrix Biology* 29 (2010), pp. 645–656.
- [20] M. Egeblad and Z. Werb. “New functions for the matrix metalloproteinases in cancer progression”. In: *Nature Reviews Cancer* 2 (2002), pp. 161–174.
- [21] T. Itoh, M. Tanioka, H. Yoshida, T. Yoshioka, H. Nishimoto, and S. Itohara. “Reduced angiogenesis and tumor progression in gelatinase A-deficient mice”. In: *Cancer research* 58 (1998), pp. 1048–1051.
- [22] J. Xu, D. Rodriguez, E. Petitclerc, J. J. Kim, M. Hangai, S. M. Yuen, G. E. Davis, and P. C. Brooks. “Proteolytic exposure of a cryptic site within collagen type IV is required for angiogenesis and tumor growth in vivo”. In: *The Journal of Cell Biology* 154 (2001), pp. 1069–1080.
- [23] T. Itoh, M. Tanioka, H. Matsuda, H. Nishimoto, T. Yoshioka, R. Suzuki, and M. Uehira. “Experimental metastasis is suppressed in MMP-9-deficient mice”. In: *Clinical & experimental metastasis* 17 (1999), pp. 177–181.
- [24] M. D. Sternlicht and Z. Werb. “How Matrix Metalloproteinases Regulate Cell Behavior”. In: *Annual Review of Cell and Developmental Biology* 17 (2001), pp. 463–516.
- [25] H. Hashizume, P. Baluk, S. Morikawa, J. W. McLean, G. Thurston, S. Roberge, R. K. Jain, and D. M. McDonald. “Openings between Defective Endothelial Cells Explain Tumor Vessel Leakiness”. In: *The American Journal of Pathology* 156 (2000), pp. 1363–1380.
- [26] H. Yoshioka. “Surface modification of haemoglobin-containing liposomes with polyethylene glycol prevents liposome aggregation in blood plasma”. In: *Biomaterials* 12 (1991), pp. 861–864.
- [27] S. Palchetti, V. Colapicchioni, L. Digiaco, G. Caracciolo, D. Pozzi, A. L. Capriotti, G. La Barbera, and A. Laganà. “The protein corona of circulating PEGylated liposomes”. In: *Biochimica et Biophysica Acta (BBA)-Biomembranes* 1858 (2016), pp. 189–196.
- [28] R. P. Bagwe, L. R. Hilliard, and W. Tan. “Surface modification of silica nanoparticles to reduce aggregation and nonspecific binding”. In: *Langmuir* 22 (2006), pp. 4357–4362.
- [29] R. K. Jain and L. T. Baxter. “Mechanisms of heterogeneous distribution of monoclonal antibodies and other macromolecules in tumors: significance of elevated interstitial pressure”. In: *Cancer research* 48 (1988), pp. 7022–7032.
- [30] F. Danhier. “To exploit the tumor microenvironment: since the EPR effect fails in the clinic, what is the future of nanomedicine?” In: *Journal of Controlled Release* 244 (2016), pp. 108–121.
- [31] R. K. Jain and L. T. Baxter. “Mechanisms of Heterogeneous Distribution of Monoclonal Antibodies and Other Macromolecules in Tumors: Significance of Elevated Interstitial Pressure”. In: *Cancer Research* 48 (1988), pp. 7022–7032.
- [32] R. K. Jain. “Vascular and interstitial barriers to delivery of therapeutic agents in tumors”. In: *Cancer and Metastasis Reviews* 9 (1990), pp. 253–266.
- [33] S. D. Conner and S. L. Schmid. “Regulated portals of entry into the cell”. In: *Nature* 422.6927 (2003), pp. 37–44.
- [34] V. C. F. Mosqueira, P. Legrand, A. e Gulik, O. Bourdon, R. Gref, D. Labarre, and G. Barratt. “Relationship between complement activation, cellular uptake and surface physicochemical aspects of novel PEG-modified nanocapsules”. In: *Biomaterials* 22 (2001), pp. 2967–2979.
- [35] R. K. Jain and T. Stylianopoulos. “Delivering nanomedicine to solid tumors”. In: *Nature reviews Clinical oncology* 7 (2010), p. 653.
- [36] Y. Fan and Q. Zhang. “Development of liposomal formulations: From concept to clinical investigations”. In: *Asian Journal of Pharmaceutical Sciences* 8 (2013), pp. 81–87.
- [37] Avi Schroeder, Joseph Kost, and Yechezkel Barenholz. “Ultrasound, liposomes, and drug delivery: principles for using ultrasound to control the release of drugs from liposomes”. In: *Chemistry and Physics of Lipids* 162 (2009), pp. 1–16.

- [38] W. D. O'Brien. "Ultrasound–biophysics mechanisms". In: *Progress in Biophysics and Molecular Biology* 93 (2007), pp. 212–255.
- [39] C. Poon, D. McMahon, and K. Hynynen. "Noninvasive and targeted delivery of therapeutics to the brain using focused ultrasound". In: *Neuropharmacology* 120 (2017), pp. 20–37.
- [40] K. L. "Ultrasound. Its Chemical, Physical, and Biological Effects. Kenneth S. Suslick, Ed. VCH, New York, 1988 xiv, 336 pp., illus." In: *Science* 243 (1989), pp. 1499–1499.
- [41] G. A. Hussein, W. G. Pitt, and A. M. Martins. "Ultrasonically triggered drug delivery: Breaking the barrier". In: *Colloids and Surfaces B: Biointerfaces* 123 (2014), pp. 364–386.
- [42] V. Frenkel. "Ultrasound mediated delivery of drugs and genes to solid tumors". In: *Advanced drug delivery reviews* 60 (2008), pp. 1193–1208.
- [43] M. C. Ziskin. "Fundamental physics of ultrasound and its propagation in tissue." In: *RadioGraphics* 13 (1993), pp. 705–709.
- [44] T. Şen, O. Tüfekçioğlu, and Y. Koza. "Mechanical index". In: *Anatolian Journal of Cardiology* 15 (2015), pp. 334–336.
- [45] P. Prentice, A. Cuschieri, K. Dholakia, M. Prausnitz, and P. Campbell. "Membrane disruption by optically controlled microbubble cavitation". In: *Nature physics* 1 (2005), p. 107.
- [46] I. Lentacker, I. De Cock, R. Deckers, S. C. De Smedt, and C. T. W. Moonen. "Understanding ultrasound induced sonoporation: definitions and underlying mechanisms". In: *Advanced drug delivery reviews* 72 (2014), pp. 49–64.
- [47] B. H. A. Lammertink, C. Bos, R. Deckers, G. Storm, C. T. W. Moonen, and J.-M. Escoffre. "Sonochemotherapy: from bench to bedside". In: *Frontiers in pharmacology* 6 (2015), p. 138.
- [48] W. L. Nyborg. "Mechanisms for bioeffects of ultrasound relevant to therapeutic applications". In: *Emerging Therapeutic Ultrasound*. World Scientific, 2006, pp. 5–66.
- [49] P. N. Prasad. "Fundamentals of Light–Matter Interactions". In: *Introduction to Biophotonics*. John Wiley & Sons, Inc., 2004, pp. 92–128.
- [50] P. N. Prasad. "Principles of Lasers, Current Laser Technology, and Nonlinear Optics". In: *Introduction to Biophotonics*. John Wiley & Sons, Inc., 2004, pp. 129–158.
- [51] P. N. Prasad. "Bioimaging: Principles and Techniques". In: *Introduction to Biophotonics*. John Wiley & Sons, Inc., 2004, pp. 203–254.
- [52] S. W. Paddock. "Principles and practices of laser scanning confocal microscopy". In: *Molecular biotechnology* 16 (2000), pp. 127–149.
- [53] Wanda M. Haschek, Colin G. Rousseaux, Matthew A. Wallig, Brad Bolon, and Ricardo Ochoa. *Haschek and Rousseaux's Handbook of Toxicologic Pathology*. 2013, pp. 202–203.
- [54] H. M. Shapiro. *Practical flow cytometry*. John Wiley & Sons, 2005.
- [55] Sofie Snipstad, Sigrid Berg, Ýrr Mørch, Astrid Bjørkøy, Einar Sulheim, Rune Hansen, Ingeborg Grimstad, Annemieke van Wamel, Astri F Maaland, Sverre H Torp, and Catharina de Lange Davies. "Ultrasound Improves the Delivery and Therapeutic Effect of Nanoparticle-Stabilized Microbubbles in Breast Cancer Xenografts". In: *Ultrasound in Medicine and Biology* 43 (2017), pp. 2651–2669.
- [56] J. Schindelin, I. Arganda-Carreras, E. Frise, V. Kaynig, M. Longair, T. Pietzsch, S. Preibisch, C. Rueden, S. Saalfeld, B. Schmid, J.-Y. Tinevez, D. J. White, V. Hartenstein, K. Eliceiri, P. Tomancak, and A. Cardona. "Fiji: an open-source platform for biological-image analysis". In: *Nature Methods* 9 (2012).
- [57] J. Schindelin, C. T. Rueden, M. C. Hiner, and K. W. Eliceiri. "The ImageJ ecosystem: An open platform for biomedical image analysis". In: *Molecular Reproduction and Development* 82 (2015), pp. 518–529.
- [58] Germany Merck KGaA Darmstadt. *Atto Dyes for Superior Fluorescent Imaging*. June 2018. URL: https://www.sigmaaldrich.com/life-science/cell-biology/detection/learning-center/atto.html?utm_source=redirect&utm_medium=promotional&utm_campaign=insite_atto.
- [59] I. V. Zhigaltsev, N. Maurer, Q.-F. Akhong, R. Leone, E. Leng, J. Wang, S. C. Semple, and P. R. Cullis. "Liposome-encapsulated vincristine, vinblastine and vinorelbine: a comparative study of drug loading and retention". In: *Journal of controlled release* 104 (2005), pp. 103–111.

- [60] M. N. Jones and A. R. Nicholas. “The effect of blood serum on the size and stability of phospholipid liposomes”. In: *Biochimica et Biophysica Acta (BBA)-Biomembranes* 1065 (1991), pp. 145–152.
- [61] D. Pozzi, V. Colapicchioni, G. Caracciolo, S. Piovesana, A. L. Capriotti, S. Palchetti, S. De Grossi, A. Riccioli, H. Amenitsch, and A. Laganà. “Effect of polyethyleneglycol (PEG) chain length on the bio-nano-interactions between PEGylated lipid nanoparticles and biological fluids: from nanostructure to uptake in cancer cells”. In: *Nanoscale* 6 (2014), p. 2782.
- [62] C. M. Dawidczyk, L. M. Russell, and P. C. Searson. “Nanomedicines for cancer therapy: state-of-the-art and limitations to pre-clinical studies that hinder future developments”. In: *Frontiers in Chemistry* 2 (2014), p. 69.
- [63] S. Unezaki, K. Maruyama, J.-I. Hosoda, I. Nagae, Y. Koyanagi, M. Nakata, O. Ishida, M. Iwatsuru, and S. Tsuchiya. “Direct measurement of the extravasation of polyethyleneglycol-coated liposomes into solid tumor tissue by in vivo fluorescence microscopy”. In: *International Journal of Pharmaceutics* 144 (1996), pp. 11–17.
- [64] E. Sulheim, J. Kim, A. van Wamel, E. Kim, S. Snipstad, I. Vidic, I. H. Grimstad, M. Widerøe, S. H. Torp, S. Lundgren, D. J. Waxman, and C. de L. Davies. “Multi-modal characterization of vasculature and nanoparticle accumulation in five tumor xenograft models”. In: *Journal of Controlled Release* 279 (2018), pp. 292–305.
- [65] S. Krasnici, A. Werner, M. E. Eichhorn, M. Schmitt-Sody, S. A. Pahernik, B. Sauer, B. Schulze, M. Teifel, U. Michaelis, K. Naujoks, and M. Dellian. “Effect of the surface charge of liposomes on their uptake by angiogenic tumor vessels”. In: *International journal of cancer* 105 (2003), pp. 561–567.
- [66] A. I. Minchinton and I. F. Tannock. “Drug penetration in solid tumours”. In: *Nature Reviews Cancer* 6 (2006), p. 583.
- [67] K. B. Bader and C. K. Holland. “Gauging the likelihood of stable cavitation from ultrasound contrast agents”. In: *Physics in Medicine & Biology* 58 (2012), p. 127.
- [68] K. Hynynen. “Focused ultrasound for blood–brain disruption and delivery of therapeutic molecules into the brain”. In: *Expert opinion on drug delivery* 4 (2007), pp. 27–35.
- [69] E.A. Brujan, T. Ikeda, and Y. Matsumoto. “Jet formation and shock wave emission during collapse of ultrasound-induced cavitation bubbles and their role in the therapeutic applications of high-intensity focused ultrasound”. In: *Physics in Medicine & Biology* 50 (2005), p. 4797.
- [70] B. Theek, M. Baues, T. Ojha, D. Möckel, S. K. Veettil, J. Steitz, L. van Bloois, G. Storm, F. Kiessling, and T. Lammers. “Sonoporation enhances liposome accumulation and penetration in tumors with low EPR”. In: *Journal of Controlled Release* 231 (2016), pp. 77–85.
- [71] H. Chen, W. Kreider, A. A. Brayman, M. R. Bailey, and T. J. Matula. “Blood vessel deformations on microsecond time scales by ultrasonic cavitation”. In: *Physical review letters* 106 (2011), p. 034301.
- [72] S. Wilhelm, A. J. Tavares, Q. Dai, S. Ohta, J. Audet, H. F. Dvorak, and W. C. W. Chan. “Analysis of nanoparticle delivery to tumours”. In: *Nature Reviews Materials* 1 (2016), p. 16014.
- [73] A. L. B. Seynhaeve, B. M. Dicheva, S. Hoving, G. A. Koning, and T. L. M. ten Hagen. “Intact Doxil is taken up intracellularly and released doxorubicin sequesters in the lysosome: evaluated by in vitro/in vivo live cell imaging”. In: *Journal of controlled release* 172.1 (2013), pp. 330–340.
- [74] A. K. Varkouhi, M. Scholte, G. Storm, and H. J. Haisma. “Endosomal escape pathways for delivery of biologicals”. In: *Journal of Controlled Release* 151 (2011), pp. 220–228.
- [75] C. Zylberberg, K. Gaskill, S. Pasley, and S. Matosevic. “Engineering liposomal nanoparticles for targeted gene therapy”. In: *Gene therapy* 24 (2017), p. 441.
- [76] R. H. Shete H. K .and Prabhu and V. B. Patravale. “Endosomal escape: a bottleneck in intracellular delivery”. In: *Journal of nanoscience and nanotechnology* 14 (2014), pp. 460–474.
- [77] Y. Feng, E.-K. Jeong, A. M. Mohs, L. Emerson, and Z.-R. Lu. “Characterization of tumor angiogenesis with dynamic contrast-enhanced MRI and biodegradable macromolecular contrast agents in mice”. In: *Magnetic resonance in medicine* 60 (2008), pp. 1347–1352.

- [78] B. F. Jordan, M. Runquist, N. Raghunand, R. J. Gillies, W. R. Tate, G.h Powis, and A. F. Baker. “The thioredoxin-1 inhibitor 1-methylpropyl 2-imidazolyl disulfide (PX-12) decreases vascular permeability in tumor xenografts monitored by dynamic contrast enhanced magnetic resonance imaging”. In: *Clinical Cancer Research* 11 (2005), pp. 529–536.
- [79] R. Venkatasubramanian, R. B. Arenas, M. A. Henson, and N. S. Forbes. “Mechanistic modelling of dynamic MRI data predicts that tumour heterogeneity decreases therapeutic response”. In: *British journal of cancer* 103.4 (2010), p. 486.
- [80] E. Hysi, L. A. Wirtzfeld, J. P. May, E. Undzys, S.-D. Li, and M. C. Kolios. “Photoacoustic signal characterization of cancer treatment response: Correlation with changes in tumor oxygenation”. In: *Photoacoustics* 5 (2017), pp. 25–35.

Appendix A

Fluorescence emission overview

APPENDIX A. FLUORESCENCE EMISSION OVERVIEW

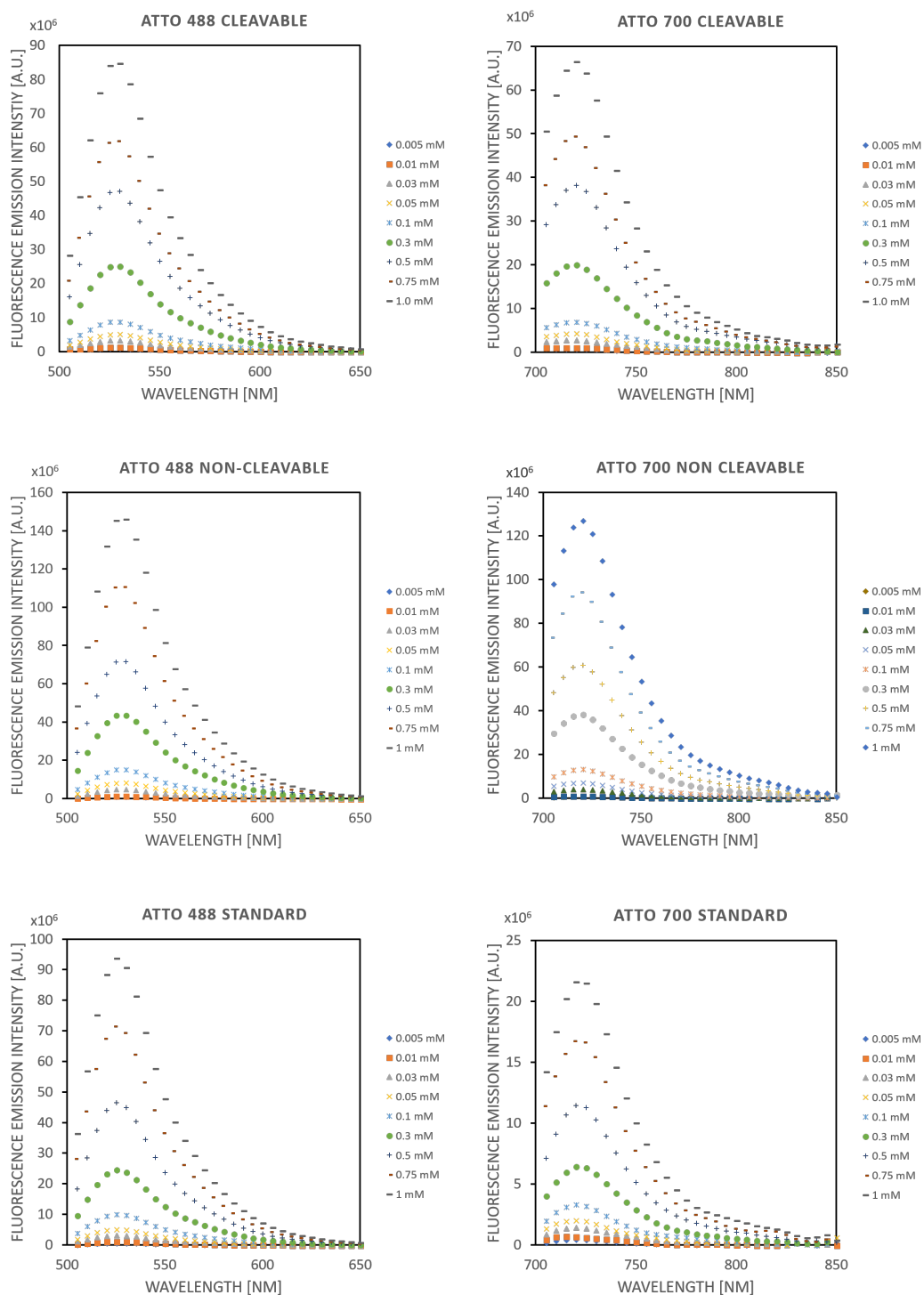
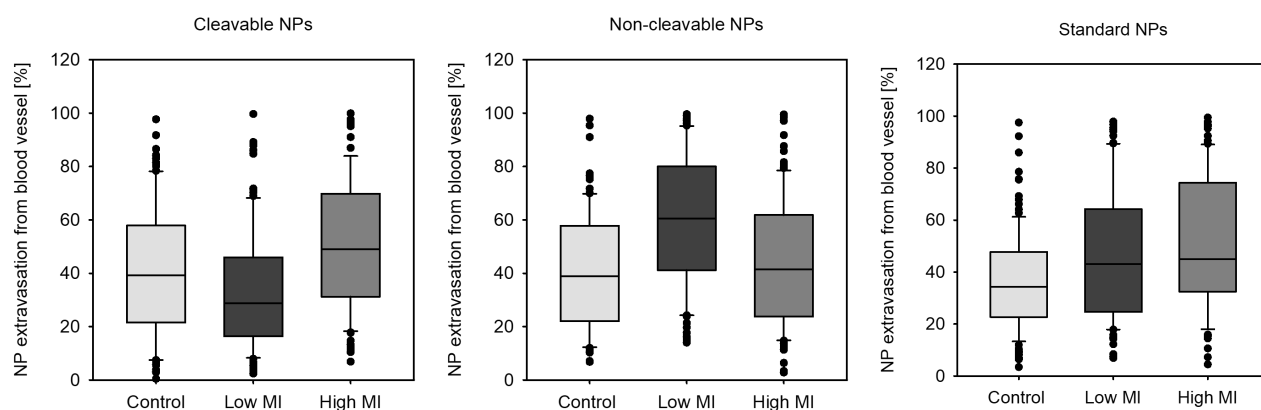


Figure A.1: Fluorescence emission intensity plots of all concentrations for both Atto 488 (left column) and Atto 700 (right column) fluorophores, for all three NPs. Cleavable (top row), Non-cleavable (middle row) and Standard (bottom row). Note difference in y-axis range.

Appendix B

Extravasation

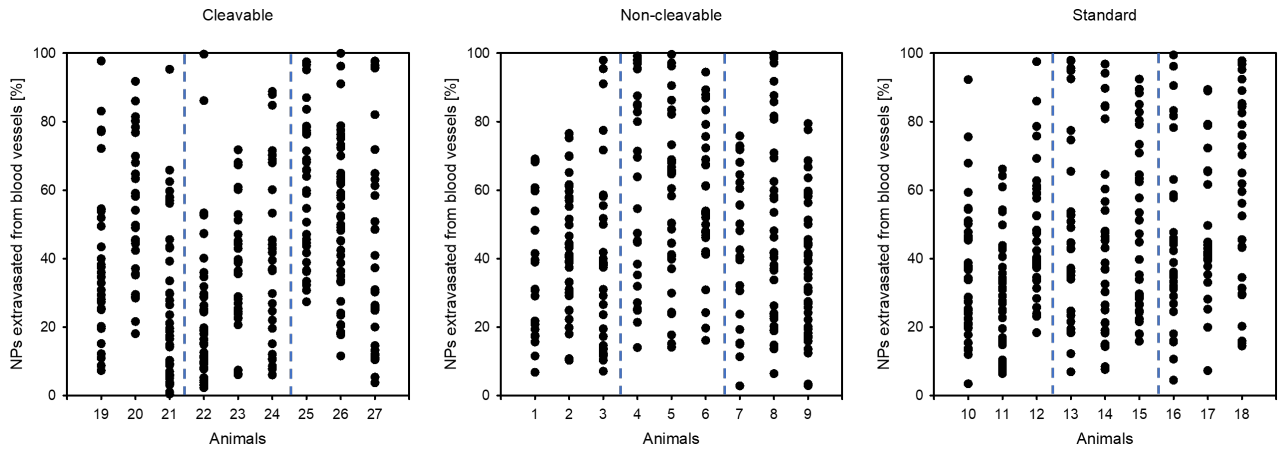


(a) Extravasation of cleavable NPs (data from fall project).

(b) Extravasation of non-cleavable NPs.

(c) Extravasation of standard NPs.

Figure B.1: Extravasation of NPs in individual images calculated as % NPs outside a blood vessel divided by the total amount of NPs in that image. Each box represents all the images in the respective ultrasound groups (control = no US, low MI = 0.4, high MI = 0.8). Boxes show 25/75 percentiles, horizontal lines are median values. Median values are calculated from all the images in a group (approximately 30 images per group).

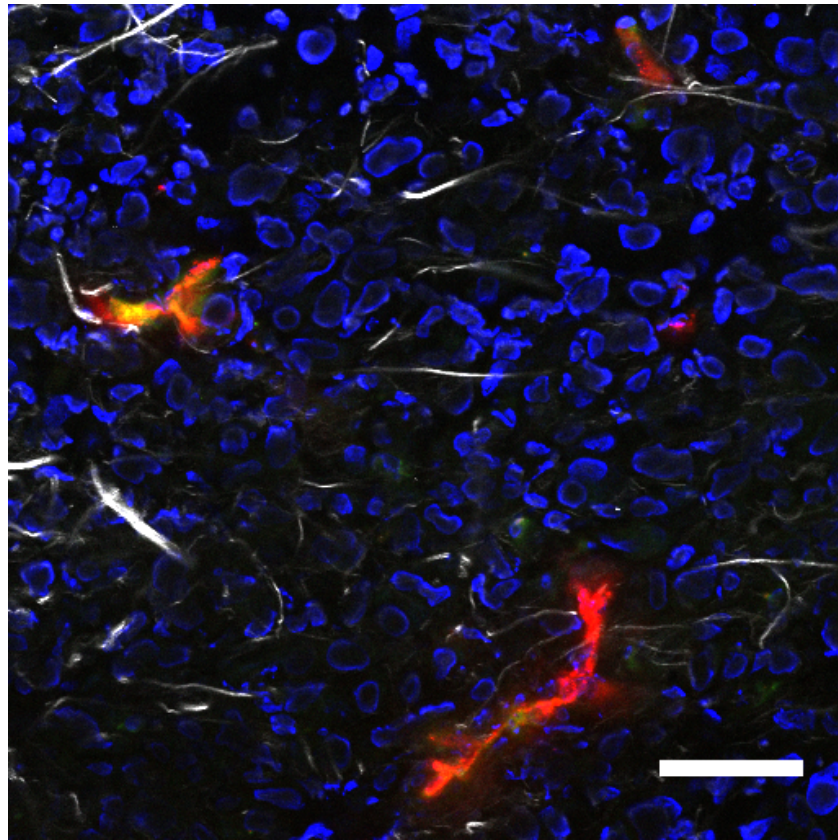


(a) Extravasation of cleavable NPs (data from fall project). (b) Extravasation of non-cleavable NPs. (c) Extravasation of standard NPs.

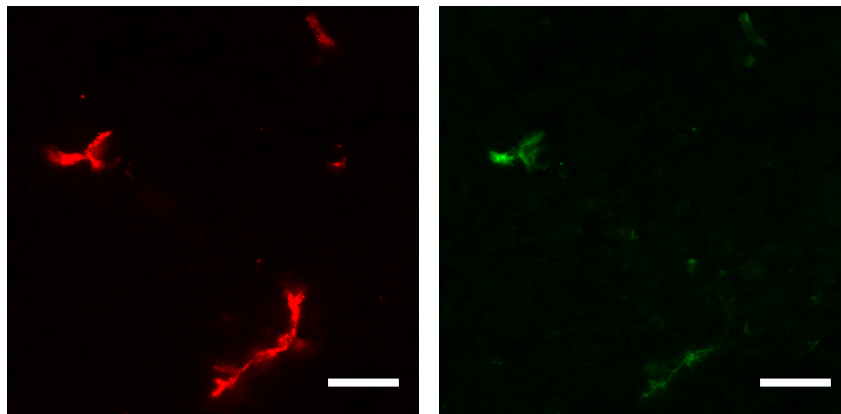
Figure B.2: Extravasation of NPs in individual images calculated as % NPs outside a blood vessel divided by the total amount of NPs in that image. All dots represent one image of one of the three sections imaged per animal.

Appendix C

Microscopy images of tumor tissue



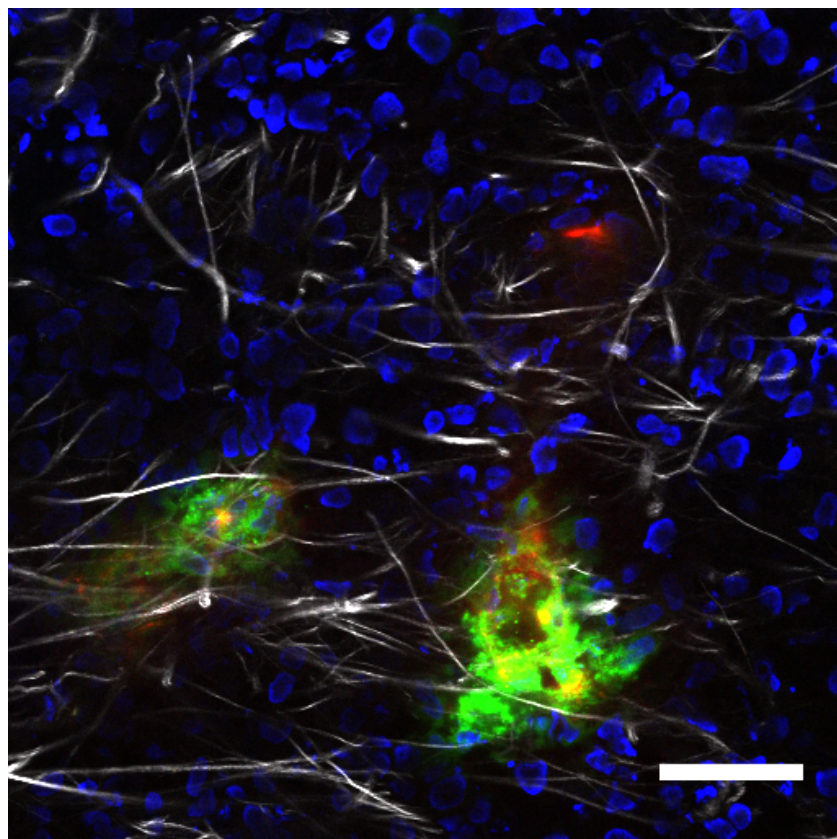
(a) Composite image.



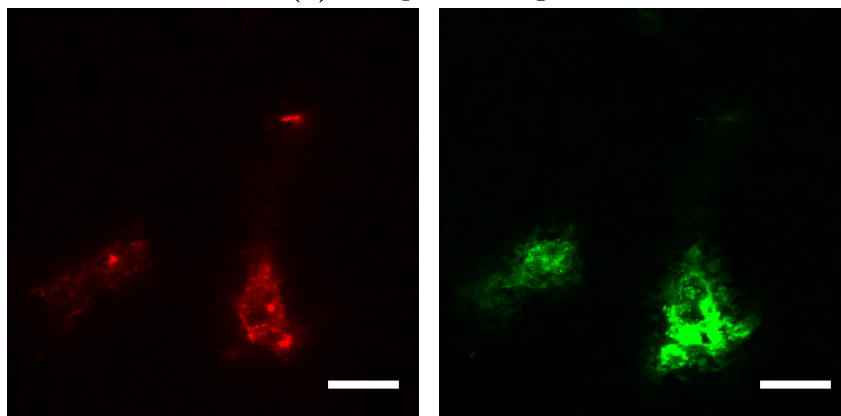
(b) Blood vessel channel

(c) Nanoparticle channel

Figure C.1: Figure from discussion on difference in extravasation. Composite image in (a) with low extravasation. Blood vessel channel and nanoparticle channel is shown in (b) and (c). Scale bars are 50 μm .



(a) Composite image.



(b) Blood vessel channel

(c) Nanoparticle channel

Figure C.2: Figure from discussion on difference in extravasation. Composite image in (a) with low extravasation. Blood vessel channel and nanoparticle channel is shown in (b) and (c). Scale bars are 50 μm .

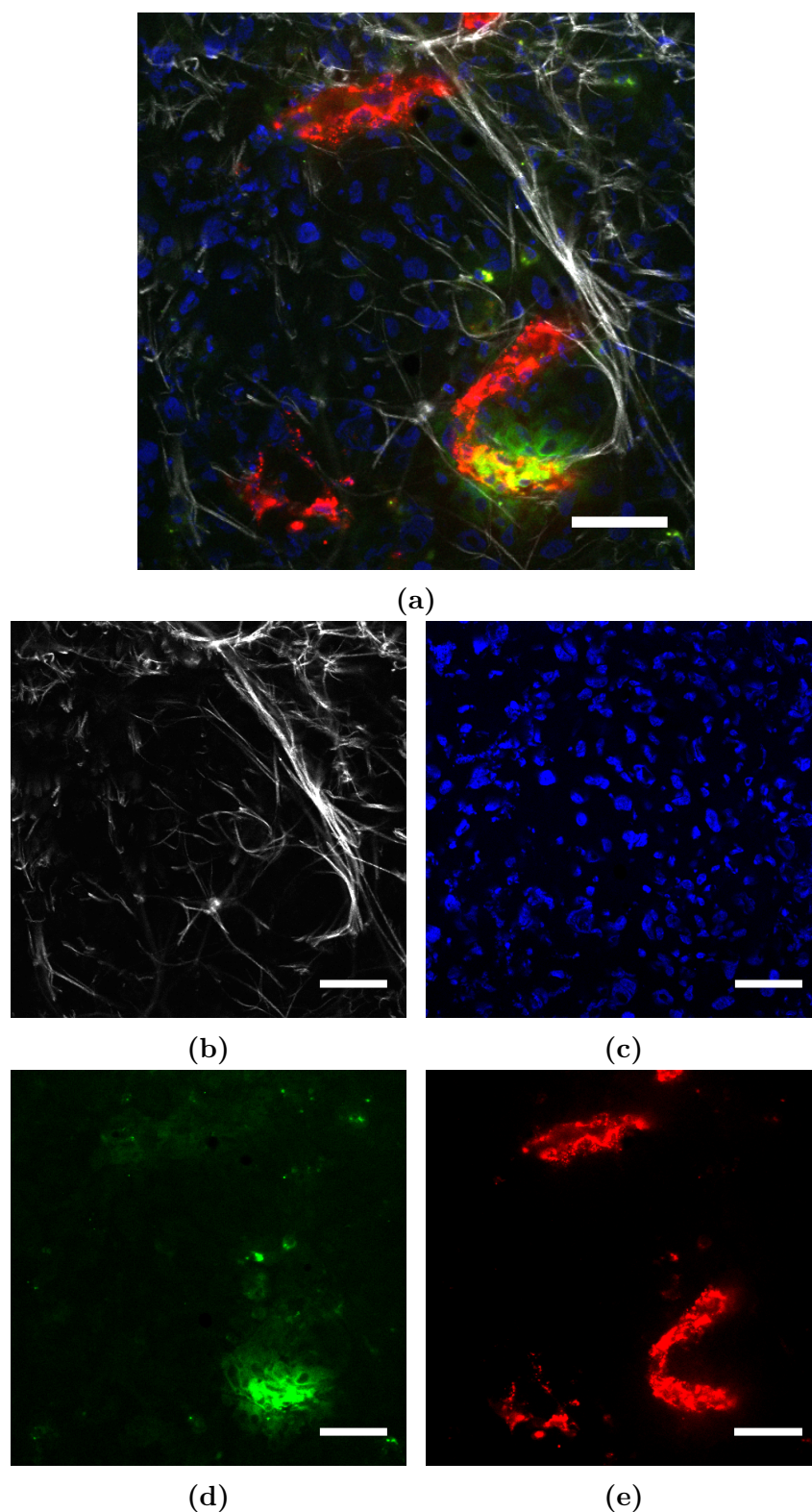


Figure C.3: Example composite image and the four channels it was merged from. Brightness is adjusted in the channels. Collagen channel is the addition of transmitted and reflected SHG signal. Scale bars are 50 μm .

Appendix D

Nuclei density

Calculations and plots of nucleic density was made for the non-cleavable and standard NPs. No significant difference was seen in tumor density, and consequently, the % extravasated NPs did not depend on nuclei concentration. Considering this, and due to a lack of time, the same calculations and plots were not made for the cleavable NPs.

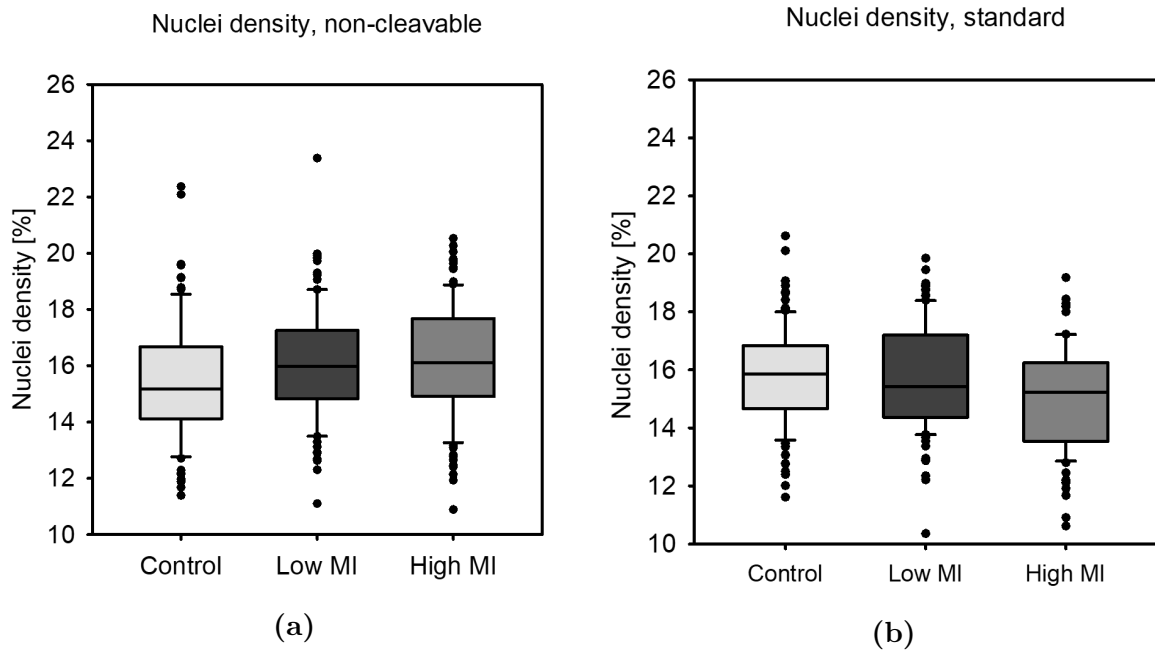


Figure D.1: Nuclei density as calculated by the percentage of pixel values above threshold in the nuclei channel (Equation 3.3). Implies low variation in cell density.

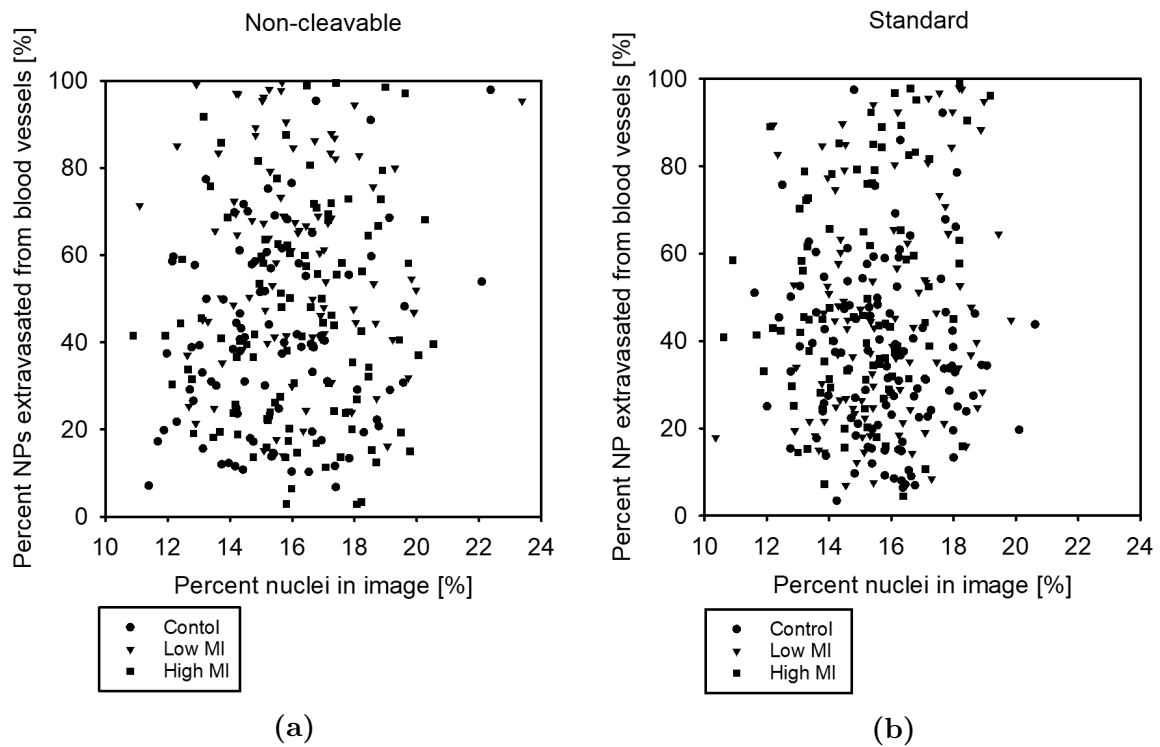


Figure D.2: Scatter plot of the nuclei density in an image against the % extravasated NPs in the same image. Each dot represents one image. Different groups are represented by different shapes.

Appendix E

Biodistribution in animals

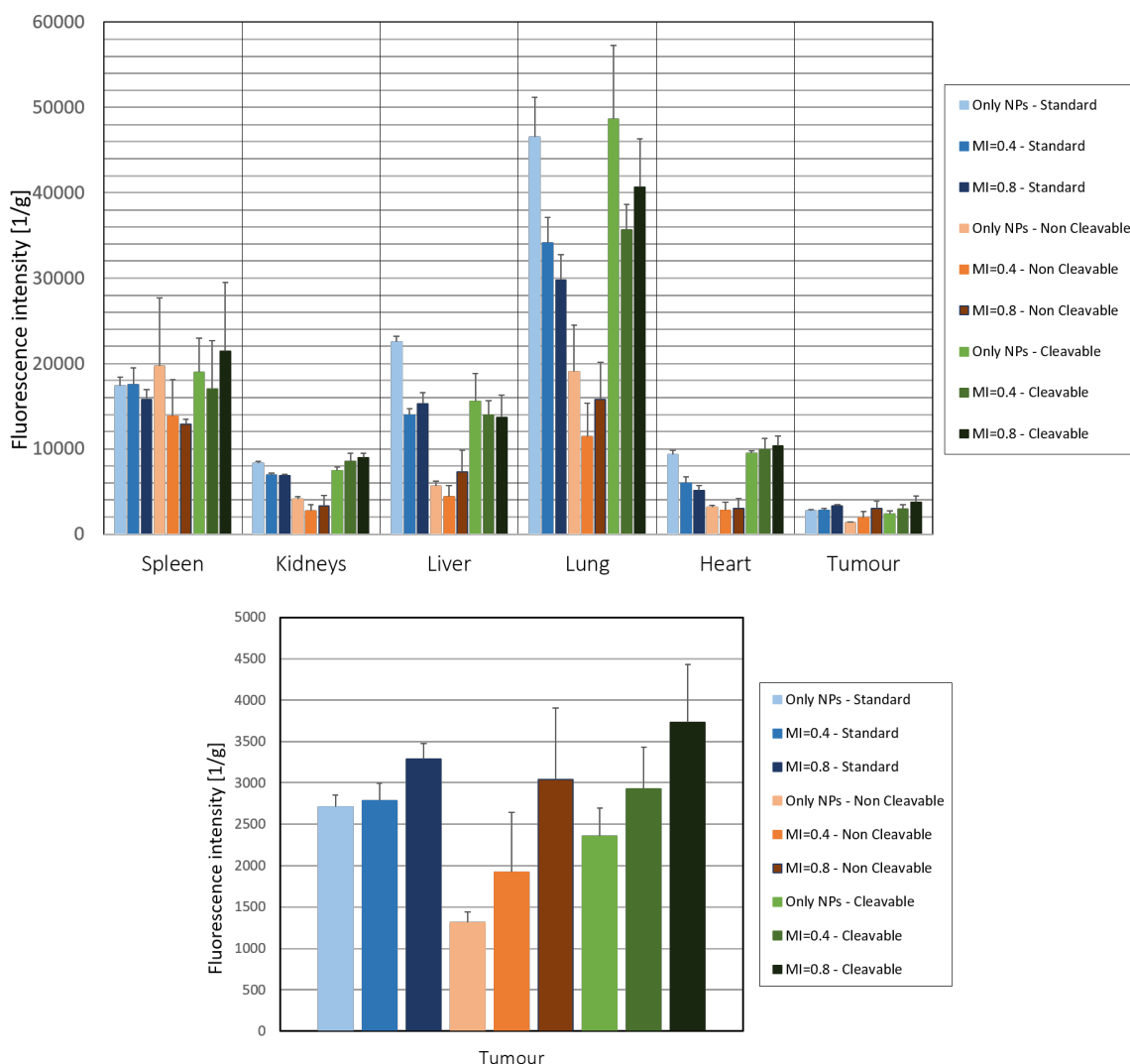


Figure E.1: Biodistribution of Atto 700 measured in whole animal optical imager. Corrected for intensity differences of the Atto 700 in the three NPs. Data provided by M. Olsman.

Appendix F

Microscopy images of lymph nodes

Nanoparticles were observed in lymph nodes, but it is unknown whether they came from the nearby tumor or from their own vasculature (Figure F.1).

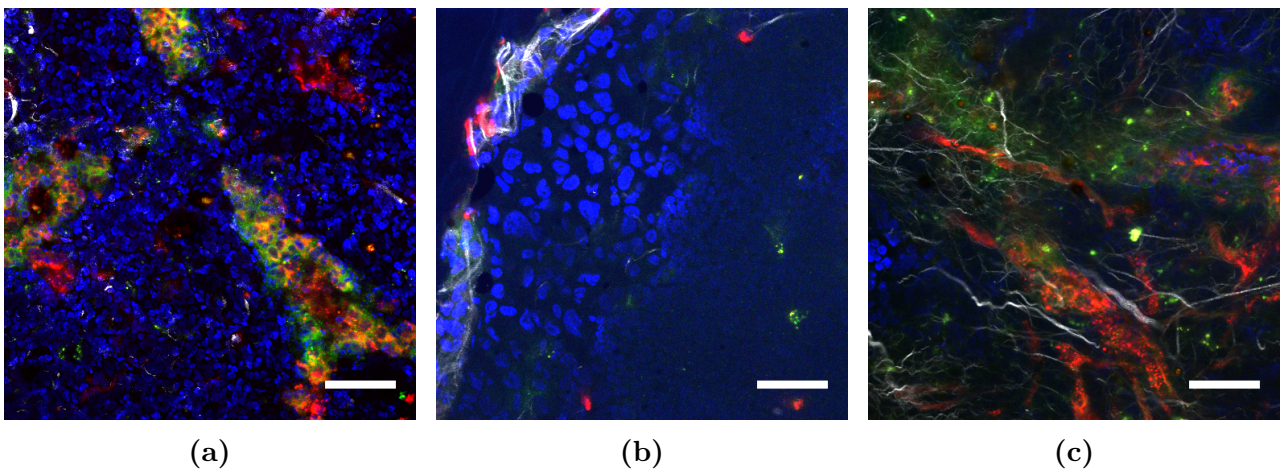


Figure F.1: Images from sections containing lymph node tissue (a-c). In (b) the interface between lymph (small nuclei) and cancer (large nuclei) can be seen. Scale bars are 50 μm .